Synthesis and characterisation of semiconductor nanoparticle thin films

A thesis submitted to the University of Manchester
for the degree of Doctor of Philosophy in the
Faculty of Engineering and Physical Sciences

2013

DAVID JOHN HENRY CANT

SCHOOL OF PHYSICS AND ASTRONOMY

Contents

Final Word Count = 34387

List of tables

List of figures

The University of Manchester

Abstract of thesis submitted by David John Henry Cant for the degree of Doctor of Philosophy and entitled '**Synthesis and characterisation of semiconductor nanoparticle thin films**'

Month and year of submission: September 2013

Due to their unique properties, nanoparticles have been a focus of significant research interest for use in various opto-electronic applications, particularly in the field of solar energy generation. In order to realize a nanoparticle based solar cell, it is important to be able to create thin films of organised nanoparticles and to be able to control their surface properties.

In this work the use of a novel synthesis technique involving reaction at the interface between two immiscible liquids to synthesise thin films of lead sulfide nanoparticles on the order of ~10 nm in diameter is reported. The use of the liquid-liquid interface allows the synthesis of particles without the use of stabilising ligands, with sizes and morphologies determined by the conditions present at the interface.

Variations in the precursor used, solvent height, and precursor concentration were explored. Films synthesised at various solvent heights displayed a decrease in particle size with increasing solvent height. This trend was seen to vary depending on the lead-containing precursor used.

Changes in the precursor concentration resulted in changes in the morphology of the resulting particles as observed with transmission electron microscopy (TEM). Preferential growth along certain planes was observed for particles synthesised with the highest lead precursor concentration.

Experiments with precursors with differing organic chain length displayed an increase in particle size with increasing chain length, as well as an increase in preferential growth observed by X-ray diffraction (XRD).

Surface ageing was investigated using X-ray photoelectron spectroscopy (XPS) techniques, which showed that all samples followed a similar oxidation mechanism. Oxidised lead species, attributed to hydrated lead oxide, were determined to be the initial oxidation product, formed within a week of exposure to air. Sulfoxy species were observed to form over a greater length of time, with sulfate being determined to be the final oxidation product. An oxidation mechanism is proposed based on XPS analysis of films exposed to air for up to nine months.

Declaration

No portion of the work referred to in the thesis has been submitted in support of an application for another degree or qualification of this or any other university or other institute of learning.

Copyright Statement

This thesis is dedicated to Dr. Samantha Hardman,
without whose tolerance and support this work
may never have been completed

Acknowledgements

Special thanks to my supervisors, Prof. Wendy Flavell, Dr. John Thomas, and Prof Paul O'Brien, for their wisdom and ideas throughout this project.

Thanks to the research group of Prof. Wendy Flavell, whose camaraderie and willingness to lend aid helped resolve many issues throughout this work.
Thanks to the research groups of Dr. John Thomas and Prof. Paul O'Brien, whose assistance with all things related to the chemistry and synthesis undertaken was invaluable.
Thanks to Dr. Christopher Muryn, whose expertise with much of the equipment used during this project was a valuable asset.
Special thanks to my fellow NOWNano DTC students, who provided a network of knowledge and alternative perspectives that most PhD students are not lucky enough to have. Thanks especially for the many relaxing evenings spent together taking each others minds off our work.
Many thanks to the DTC staff and academics, who helped start the DTC and were always willing to listen and respond to feedback about the course. Thanks also to the EPSRC for funding this work.

Very special thanks to my parents, who completely failed to dissuade me from following in their footsteps to do a PhD in Physics at Manchester.
Many thanks to the friends too numerous to mention, who have made my time in Manchester as enjoyable as it has been.

Exceptional thanks to $C_8H_{10}N_4O_2$, without whose continued existence none of this would have been possible.

The Author

The author graduated from the University of Manchester in 2009 with a Master's degree in Physics. Immediately following this he was accepted onto the NOWNano DTC postgraduate research course, for which this thesis is the final product.

Chapter 1: Introduction

It is well known that the world's energy requirements have been steadily increasing for the last several decades[1] with increasing levels of development and increasing population across much of the globe demanding greater and greater supply. Much of this energy requirement is currently sourced from fossil fuels[1] which are fundamentally limited in nature – there are no new reserves of oil or coal being created. The knowledge of this limited supply, and the increasing demand for energy has resulted in a steady driving up of the cost of fossil fuels in recent years. In addition to these factors, there are concerns that continued use of fossil fuels may contribute to global warming, and the severe environmental issues this may cause.

Due to these concerns, interest in other energy sources, especially those considered 'renewable' has vastly increased in recent years. Of these alternative energy sources, one that holds particular interest is solar power. As, ultimately, almost all energy sources we currently use originate in some way from the Sun, then the direct conversion of sunlight into power holds appeal as the most direct and potentially environmentally safe method of energy generation. There are several ways of generating electricity *via* sunlight, ranging from using solar energy in the production of hydrogen as a fuel, through to the thermal methods that have been until recently the most common, and also directly, through the photovoltaic effect[2]. Production of electricity *via* the photovoltaic effect simply requires a device capable of exhibiting the effect (typically some form of photodiode) and electromagnetic radiation of the correct wavelength to cause the effect (for effective use as an energy source, this will of course be sunlight). As such, efficient exploitation of the photovoltaic effect is an important goal in the future of energy generation.

1.1 - Photovoltaic Devices (PVD)

The photovoltaic effect is the process whereby illumination of a device by radiation results in a potential difference (a voltage) across the device. This is a similar process to the photoelectric effect, where electrons are ejected from a material by incident photons. However, the photovoltaic effect typically takes place in a semiconductor, where, rather than being ejected from the material, the electrons are excited into the conduction band of

the semiconductor[3]. This leaves behind an atom in the valence band with an empty energy state, or a 'hole'. Normally, these two opposing charges will, after a time, recombine; in a photovoltaic device, however, recombination is prevented, and the charges are separated to electrodes at either side of the device, resulting in a flow of current. It is clear that for photovoltaic devices to be used in energy production, their band gap energies must be located at the point within the solar spectrum at which they can convert the largest amount of energy possible into usable power.

1.1.1 - Semiconductor pn Junctions

Semiconductor pn junctions are one of the most fundamental forms of photovoltaic device. Consisting of two adjacent sections of semiconductor material, one doped with donor atoms and one with acceptors,electrons and holes flow from one side to the other until the concentrations reach an equilibrium and the Fermi energies of the two halves become equal. This forms what is known as the depletion layer in between the two halves, whose band structure takes the form shown in figure 1.

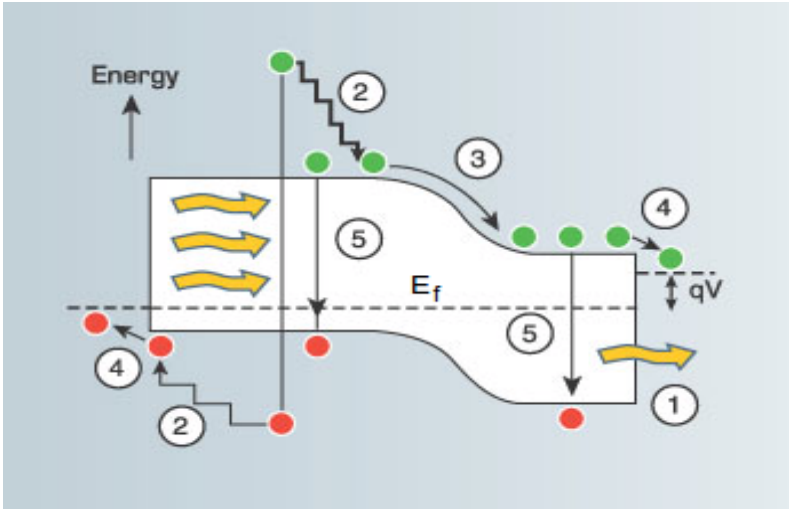

Figure 1.1: Diagram showing the various processes that result in a loss of energy (and thus efficiency) in a pn junction based photovoltaic device: incident photons may excite an electron (shown in green) from the valence band into the conduction band, leaving behind a positive 'hole' (shown in red). Photons without the required energy to excite an electron will pass through without being absorbed (1). If excitation occurs, the electron-hole pair will typically undergo thermal relaxation (2) followed by either recombination (5) or charge separation to produce a current. Voltage losses will also occur due to the junction (3) and at the contacts (4)[42].

This results in a potential difference between the two, which acts to separate any electron-hole pairs produced. There are many ways in which a single pn junction can suffer losses in the amount of energy it can harvest from an individual photon, as depicted in figure 1.1, and these loss processes limit its efficiency to around 31% (under non-concentrated sunlight), known as the 'Shockley-Queisser Limit'[4]. A breakdown of the proportion of energy that can be converted to usable electric power is shown in figure 1.2. Commercially available solar cells do not currently reach the Shockley-Queisser limit, and therefore there is still potential in maximising efficiency without necessarily overcoming the limit[5].

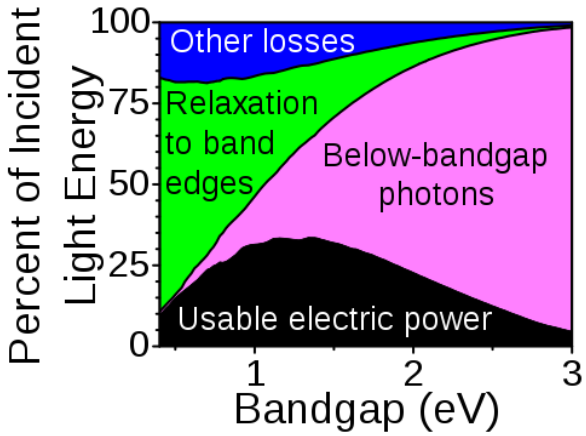

Figure 1.2: Diagram of the proportion of incident light energy lost to each of the major loss processes as a function of the band gap[43].

So-called 'first generation' solar cells are those made using bulk single crystals, typically of doped silicon. These may have a high efficiency, but their manufacture is costly due to the requirement for extremely high-purity silicon. Solar cells made using thin film technology are around 3 times cheaper than bulk single crystal wafers, and thus much larger areas can be produced; cells of this type are often known as second generation solar cells. Third generation cells are typically technologies that maintain the relatively low production costs, similar to second generation cells, while enhancing the efficiency of the cell, often aiming to surpass the Shockley-Queisser limit (figure 1.3).

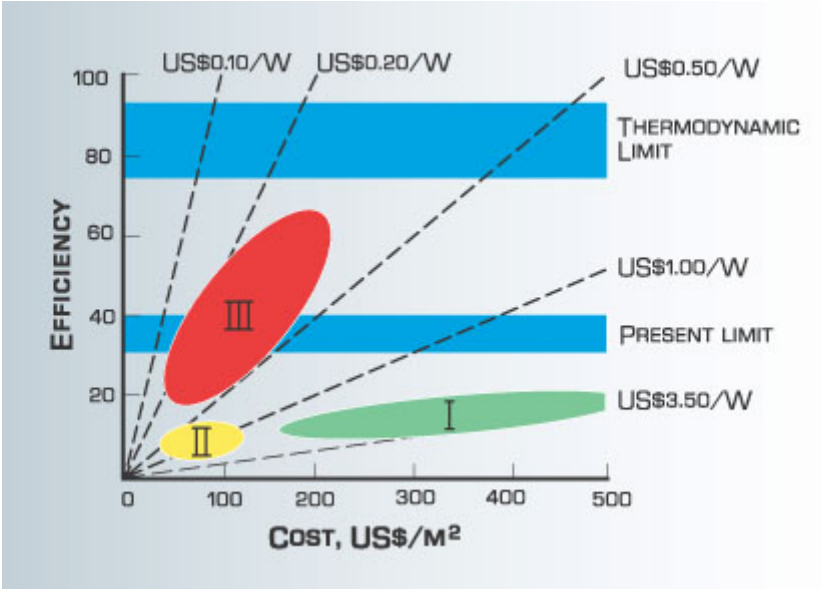

Figure 1.3: Graph of the cost per m^2 in USD against the efficiency of the three different generations of solar cells. The lower blue band represents the range of the Shockley-Queisser limit for a single band gap solar cell and the higher blue band represents the limit for multiple band gap cells.

In order to surpass this limit, there are multiple routes. Most of the losses are due either to the difference between the energy of the photon and the band gap of the device, or due to the bandgap being too high to absorb much of the incident light. Energy in excess of the bandgap will typically be lost as thermal excitation of the lattice, however there are many methods of avoiding this. They usually involve the conversion of the photon into more than one excited electron-hole pair. One such method is the process of down-conversion [6] whereby an incident photon interacts with a 'luminescence converter', or phosphor, coated ontop of the PVD, resulting in two or more lower energy photons. This process is often highly inefficient however, but can be used to produce small improvements in the overall efficiency of the cell. A similar process, known as upconversion can also serve to counteract the issue of low-energy photons not being absorbed – two or more photons which pass through the device may be absorbed by an upconverter beneath it to produce a single, higher energy photon[7]. One method commonly used to combat both issues, even in current first generation cells, is to layer multiple different bandgap materials, starting with those that absorb the highest energies. In this manner, one can absorb much more of the incident radiation efficiently, however there are obviously proportional increases in cost.

1.2 – Alternative Light Harvesting Elements

The 'light-harvesting element' of a solar cell refers to the portion of the cell which interacts directly with the incident photons, for example in a first generation cell this is the silicon pn junction itself. In recent years, many different possible light harvesting elements have been considered for use in solar cells, each with their own advantages and disadvantages. An ideal light harvesting element would be capable of absorbing photons at a high efficiency over the entire solar spectrum (figure 4), while converting as much of the energy of each photon into electrical current. Many light harvesting elements are typically a form of pn junction, or operate in a way analogous to one.

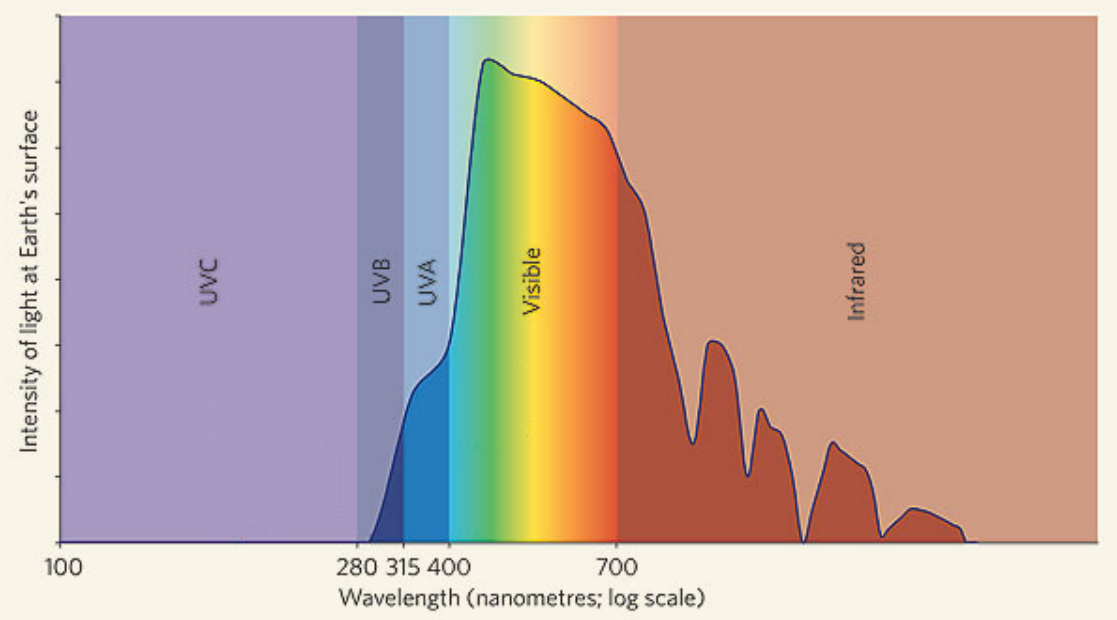

Figure 1.4: Graph of the solar spectrum incident at the surface of earth[38].

Much work has gone into optimising first generation cells, often *via* the creation of extremely tailored cell structures such as multi-junction diodes[8]. These are constructed of several diodes with varying band gaps layered on top of one another in order to be able to absorb efficiently over a large portion of the solar spectrum. Such devices have a substantially higher efficiency limit than single-junction devices – losses due to unabsorbed low energy photons and thermal relaxation of the electron-hole pair can be reduced. Also available is the use of up- and down-converters previously mentioned, which can be a relatively low-cost way to provide an improvement of efficiency to a cell[6,7]. Indeed, as of 2005, monolithic three-junction cells were by far the most efficient solar cell technology demonstrated, as seen in figure 1.5. Multi-junction cells are

however impractical for use in terrestrial applications due to their prohibitive cost, typically only being used for applications where space or mass are at a premium, such as in space exploration. As such there is a substantial amount of research being conducted into other, more cost-effective methods of solar power generation.

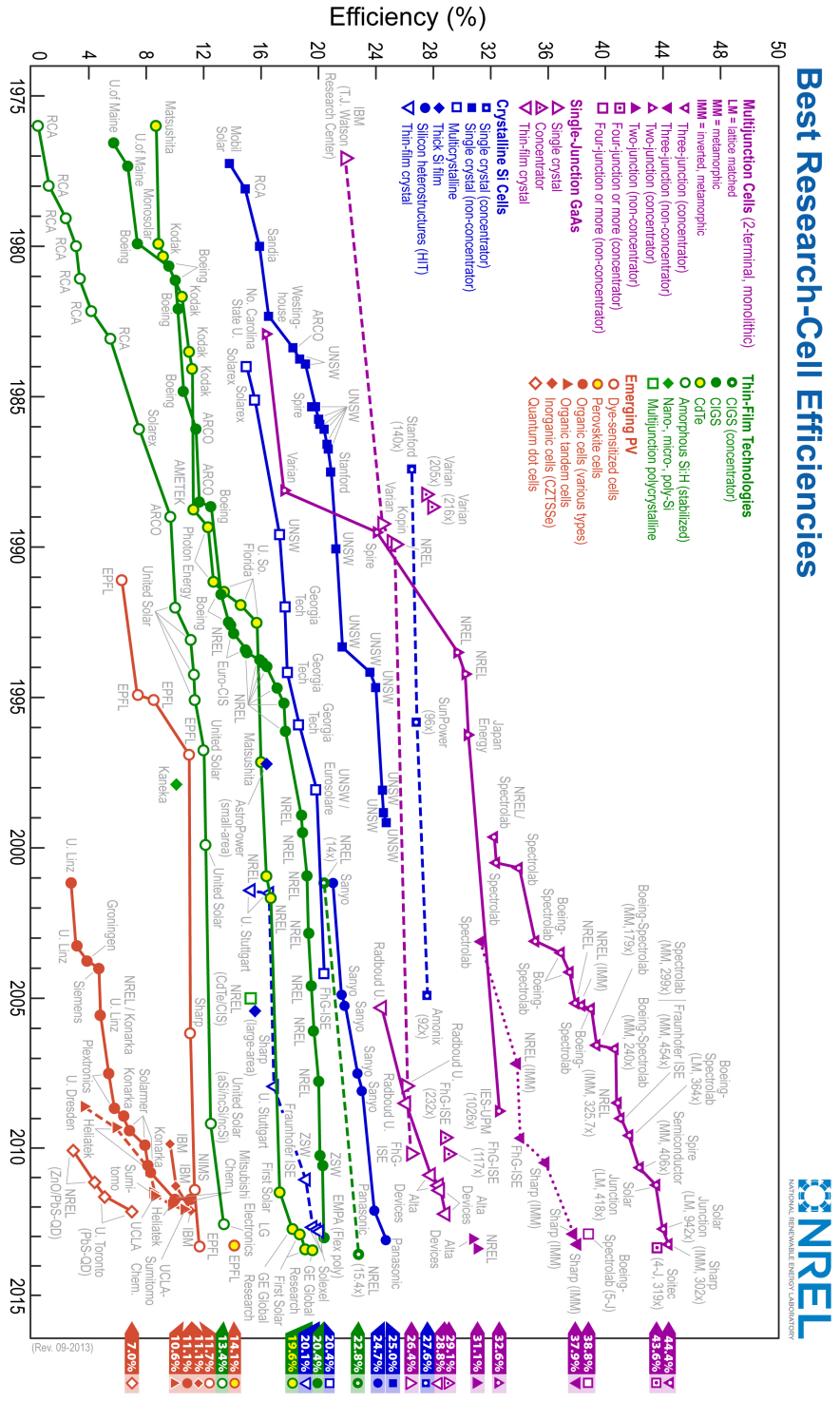

Figure 1.5: Graph of the highest achieved solar cell efficiencies measured at an accepted centre for standard solar cell measurements[41].

1.2.1 Organic Semiconductors

Certain types of organic compound, from molecules to polymers, are semiconducting; such compounds have states analogous to the valence and conduction bands in inorganic semiconductors. The concept of so-called 'plastic' solar cells [9] is appealing, for a variety of reasons – production of solar cells *via* chemical processes has the potential to greatly reduce the cost and complexity of manufacture[10] while also allowing a high degree of customisability[9]. The simplest of such cells consists of a single layer of an organic semiconductor placed between contacts of differing work functions, in order to provide a potential difference across the cell and separate the produced charge. More advanced cells usually involve either multiple organic semiconducting compounds with differing electrical properties – analogous to the donors and acceptors of inorganic semiconductor technology – or include some other material to act as part of the produced 'junction'. C_{60} is an often-used material for this, as it can be used as a strong electron-acceptor in such cells[11]. While potentially very convenient in terms of manufacture, the main disadvantage of organic photovoltaics is that their efficiencies, and indeed their limits, are much lower than most other technologies [5,12,13] .

1.2.2 Dye-Sensitized solar cells

Dye-sensitized solar cells are a thin-film-based technology that, while not necessarily achieving efficiencies competitive with the highest efficiencies observed in other thin film cells, have several advantages in terms of simplicity of manufacture and low cost. Despite achieving photo-conversion efficiencies that reach, at a maximum, ~12%[14], the low cost to construct a dye-sensitized solar cell allows them to reach extremely low costs-per-watt, and potentially achieve grid parity[15]. The construction of a dye solar cell is simple; a transparent anode is coated onto the back of a transparent plate (typically glass, although alternatives are a subject of interest[15] for reducing cost), and an oxide electrode, typically titanium dioxide which forms a porous, high-surface-area structure, is coated onto the back of this anode. This construction is then soaked in a mixture of a photosensitive dye in a solvent, resulting in covalent bonding of the dye to the surface of the TiO_2. This is then attached to a second plate, consisting of an electrode (typically platinum) coated in iodide electrolyte. To prevent the escape of the electrolyte, this structure must then be sealed.

Incident light upon the dye-sensitized solar cell is absorbed by the dye, which, once excited, injects electrons into the TiO_2 where they are removed at the anode in order to perform work. Electrons are then returned at the platinum electrode where they are transferred back to the dye *via* the electrolyte. The process of photocurrent production *via* dye-sensitization of semiconductors was discovered in the late 1960's[16] and the production of a dye-sensitized solar cell was published by Grätzel and O'Regan in 1991[17](leading to such cells being alternatively called "Grätzel" cells). The main issue facing development of dye-sensitized solar cells are their lack of durability to weather conditions due to the liquid electrolyte required, which can freeze or expand based on temperature, effecting power conversion and potentially damaging the device. Replacement of certain components of the design, such as the expensive platinum electrode, the liquid electrolyte, or the glass substrate, in efforts to reduce cost or solve issues with durability, has proven difficult without causing corresponding reductions in efficiency[15].

1.2.3 Solar Fuel Cells

Although not always an application of the photovoltaic effect, and not necessarily an alternative light-harvesting element, the various types of fuel cell are worth mentioning as a competing cell architecture within the field. Solar fuel generation, often referred to as a type of 'artificial photosynthesis', is the process of utilising sunlight to directly or indirectly produce some form of storable fuel (often hydrogen and oxygen from water). In a chemical context, burnable fuels are those which can be oxidised to produce energy. Thus, the process of solar fuel generation typically requires some material which can be reduced to form such a fuel, and a source of electrons with which it can be reduced[18]. The redox reaction of water to produce hydrogen is thus an excellent candidate, and the cleanliness of hydrogen gas as a fuel provides another advantage. TiO_2, ZnO, and WO_3 have been reported as potential candidates for anodes in the photovoltaic electrolysis of water, due to their stability on exposure to typical electrolyte solutions and appropriate band-gap energies. However their relatively low absorption requires treatment in order to produce a viable cell. Hensel *et al.*[19] recently reported the generation of hydrogen from a photochemical cell based upon N-doped TiO_2 sensitized using CdSe quantum dots as the photoanode, immersed in an aqueous solution of Na_2S and Na_2SO_3 electrolytes. Solar fuel production has one clear advantage over other methods of extracting solar energy in

that the produced fuel can be stored and used when needed, and as such does not rely on the immediate presence of sunlight for power. The counter to this is of course the fact that energy stored in fuels cannot be extracted with 100% efficiency, thus decreasing the potential efficiency of this method of obtaining energy from the sun.

1.3 - Quantum Dots as Light-Harvesting Elements

Semiconductor quantum dots present a highly-appealing alternative to traditional semiconductors as the light harvesting element in a photovoltaic device, due to several advantageous properties for the conversion of solar light into usable energy. The defining characteristic of a quantum dot is its ability to demonstrate quantum confinement; quantum confinement is an effect that occurs when the size of a nanoparticle is small enough such that it can be considered as a potential well with dimensions on the order of the Bohr radius of an exciton – the name given to the electron-hole pair generated upon excitement of an electron into the conduction band of a semiconductor. An exciton can be considered as analogous to a hydrogen atom, as it consists of a single positive and negative charge bound together. This bound state forms the lowest energy state that the excited electron can occupy. In keeping with the analogy to a hydrogen atom, excitons within a material may have a Bohr radius – a characteristic distance describing the separation of the electron-hole pair, differing dependent on the material it exists within due to the permittivity and effective mass of charge carriers within that particular medium. As the size of a nanoparticle approaches the scale of the exciton Bohr radius, the boundaries of the particle begin to confine the position of the charge carriers, acting as a three-dimensional potential well. In this situation the particle becomes more like an atom, its energy levels becoming discrete rather than forming continuous bands. This can be described by the confinement of the electron's wavefunction in one or more dimensions – the boundary conditions of the resulting potential well limit the available energy states which the electron may occupy. Quantum confinement in one dimension is shown in figure 1.6. As the dimensions of this potential well decrease the wavelength of bound states of the particle must decrease, and therefore the allowed states increase in energy. This same effect effectively applies to the hole in the valence band,

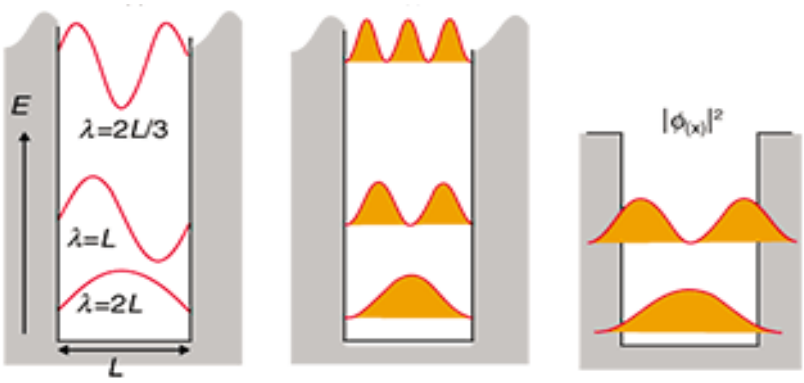

Figure 1.6: Diagram showing how confinement of a particle's wavefunction in one dimension limits the available energy states, where L is the diameter of the well, E is the energy, and λ is the particle wavelength. From left to right; the wavefunction of a particle in an infinite potential well; the probability density of the same particle; and the probability density of a particle in a finite well, where there begins to be a finite probability of the particle penetrating the walls of the well.[38,39]

figure 1.7 shows the difference in energy level diagrams for semiconductor quantum dots as opposed to the bulk semiconductor.

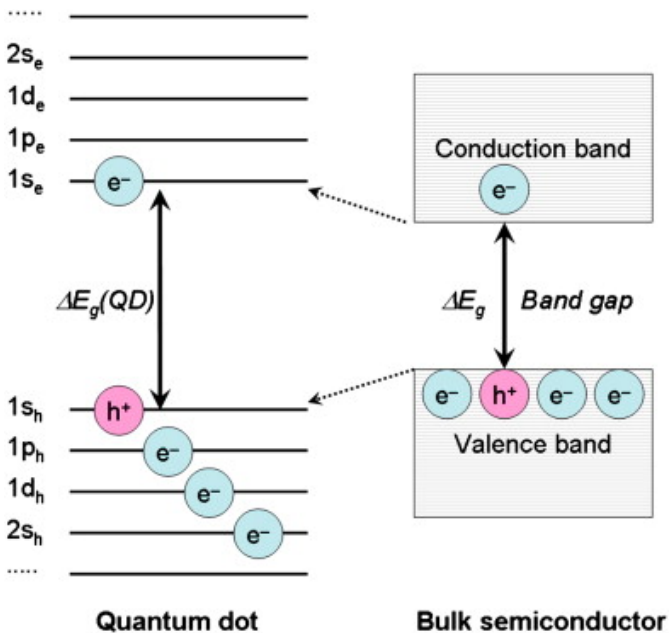

Figure 1.7: Diagram depicting how the allowed energy levels for a quantum dot are altered in comparison to a bulk semiconductor.

This confinement of the exciton within a nanoparticle has the effect of altering its band gap, the size of which is inversely proportional to the square of the particle's diameter [20]. Equation 1 shows the relationship of the band gap of a nanoparticle (E_{GNP}) with the band

gap of the bulk material (E_{GBulk}) and the particle's diameter (L). K is a constant dependant on the material.

$$E_{GNP} = E_{GBulk} + \frac{K}{L^2} \quad (1)$$

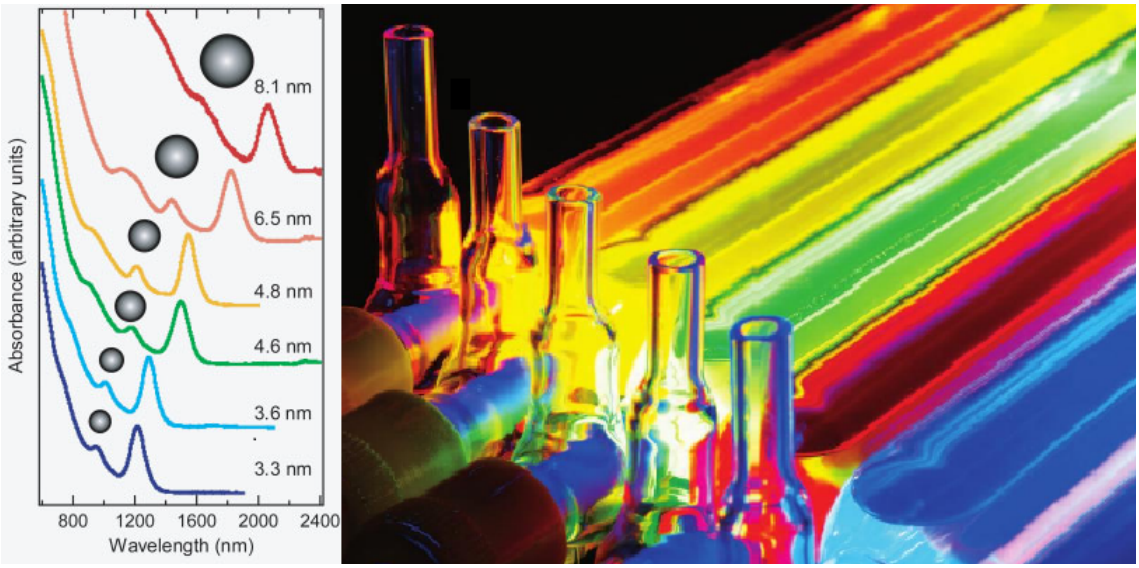

Figure 1.8: (Left) Absorption spectra of PbSe nanoparticles as a function of size[40] (Right)Image showing varying luminescence of nanoparticles with size[37] – as the nanoparticle size is decreased, the band-gap of the particle is increased, and as such both the photo-absorption and photoluminescence due to recombination of the electron-hole pair are shifted towards the blue end of the spectrum.

The ability to alter the band gap of a material simply by changing particle size has immediately obvious uses for photovoltaics – if the band gap can be tailored, this allows direct customisation of its absorption and emission properties[21] (figure 1.8).

This customisation provides obvious advantages for the production of multi-band-gap cells, theoretically allowing the production of cells tailored to absorb across the entire solar spectrum. A further advantage of quantum-dot-based solar cells is their cost; most routes to their production investigated currently are based upon colloidal chemistry or other relatively low-temperature chemical methods of manufacture. This renders them substantially cheaper to produce that first-generation cells.

In 2004, researchers at Los Alamos national laboratory in the USA showed that lead selenide quantum dots (QDs) showed an effect known as carrier multiplication or multiple-exciton generation (MEG)[22] to a much greater degree than the bulk material. In this process, photons of energy greater than twice the band gap of the QD are capable of creating more than one excited electron-hole pair, as the energy released by charge carrier

relaxation to the band gap is capable of exciting a second electron-hole pair, as shown in figure 1.9.

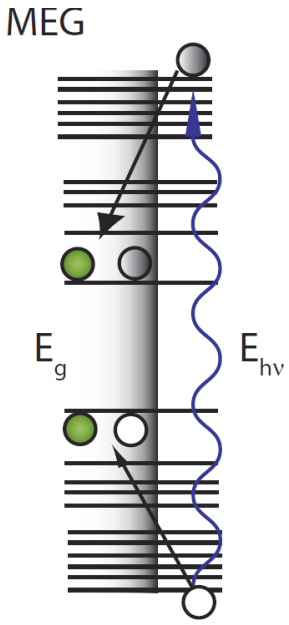

Figure 1.9: Schematic diagram depicting the conditions for multiple exciton generation, in which an electron-hole pair excited by a photon of equal to or greater than twice the band gap energy results in the excitation of a second electron-hole pair upon relaxation to the band edges[40].

This potentially reduces one major source of energy loss in standard photovoltaic devices, i.e. thermal relaxation of excited electrons with excess energy. This therefore raises the potential limiting efficiency of photovoltaic devices based on quantum dots. While initial estimates of the efficiency of this process – claims of up to seven excitons being produced from a single photon[23] – were later considered to be overestimates due to the presence of false positives[24], the potential of higher-efficiency PVDs has still excited a substantial amount of research into the production of QDs, especially those which may present strong MEG. MEG has been demonstrated to occur in a wide range of different QD materials, including PbSe, PbS, InP, Si, CdSe and others[25–31].

1.4 - Lead Sulfide (PbS) Nanoparticles

Lead sulfide (PbS) nanoparticles have attracted particular interest as potential materials for use in photovoltaic devices for several reasons. Lead sulphide was one of the first materials to be shown to exhibit strong MEG when in nanoparticle form [29]. Bulk PbS also has a particularly small band gap of ~0.41 eV[32] and relatively high exciton Bohr-radius of 18 nm[32]. These properties grant it high tunability (due to the large Bohr-radius) over a range of energies which are well-suited to the solar spectrum (due to its low initial band

gap), together rendering it one of the most easily customisable materials for solar photovoltaics. Lead and sulphur themselves are moderately inexpensive, and as with nanoparticles as a whole, there are many low-cost synthesis routes for forming lead sulfide nanoparticles[33]. Photovoltaic devices manufactured using lead sulfide nanoparticles synthesised using colloidal techniques have been reported achieving 2-7% efficiency[34,35]. The current record efficiency for a quantum-dot-based solar cell is held by a device produced at the University of Toronto in 2012[36] consisting of a film of colloidally-synthesised lead sulfide quantum dots, spin-coated onto a TiO_2 substrate on FTO-coated glass, with a MoO_3/Au/Ag stack as the top electrode. The device achieved a power conversion efficiency of >7% using lead sulfide nanoparticles with an optical band -gap of 1.3 eV, treated using a 'hybrid' passivation scheme involving the introduction of halide anions during the latter stages of synthesis, as well has passivation using organic ligands. The use of halide anions allows passivation of trap sites unreachable by larger organic ligands, thus reducing the rate of electron-hole recombination due to such states, resulting in the increased efficiency observed.

In the work presented here, lead sulfide nanoparticles synthesised *via* a novel technique involving the formation of a film of solid particles at the interface between two immiscible liquids (discussed in detail in chapter 3) are characterised using a variety of techniques described in chapter 2. The production of a solid film of particles is required for use in many optoelectronic devices such as photovoltaics, and thus a synthesis technique which produces such films directly is advantageous. The aims of this work were to synthesise such films, and characterise their features such as particle size, photoabsorption, and surface oxidation, which are important factors in the manufacture and efficiency of photovoltaic devices.

References

(1) International Energy Agency - Statistics http://www.iea.org/statistics/ (accessed Sep 29, 2013).

(2) Croxford, B.; Scott, K. Can PV or Solar Thermal be cost effective ways of reducing CO2 emissions for residential buildings? **2006**.

(3) Böer, K. W. *Introduction to Space Charge Effects in Semiconductors*; Springer Berlin Heidelberg: Berlin, Heidelberg, 2010; Vol. 160, pp. 201-218-218.

(4) Shockley, W.; Queisser, H. J. *Journal of Applied Physics* **1961**, *32*, 510.

(5) Kazmerski, L. *Journal of Electron Spectroscopy and Related Phenomena* **2006**, *150*, 105.

(6) Trupke, T.; Green, M. A.; Würfel, P. *Journal of Applied Physics* **2002**, *92*, 1668.

(7) Shalav, A.; Richards, B.; Green, M. *Solar Energy Materials and Solar Cells* **2007**, *91*, 829.

(8) Geisz, J. F.; Friedman, D. J.; Ward, J. S.; Duda, A.; Olavarria, W. J.; Moriarty, T. E.; Kiehl, J. T.; Romero, M. J.; Norman, A. G.; Jones, K. M. *Applied Physics Letters* **2008**, *93*, 123505.

(9) Brabec, C. J.; Sariciftci, N. S.; Hummelen, J. C. *Advanced Functional Materials* **2001**, *11*, 15.

(10) Brabec, C. *Solar Energy Materials and Solar Cells* **2004**, *83*, 273.

(11) Roncali, J. *Chemical Society Reviews* **2005**, *34*, 483.

(12) Forrest, S. R. *MRS bulletin 30*, 28.

(13) Shaheen, S. E.; Brabec, C. J.; Sariciftci, N. S.; Padinger, F.; Fromherz, T.; Hummelen, J. C. *Applied Physics Letters* **2001**, *78*, 841.

(14) Hagfeldt, A.; Boschloo, G.; Sun, L.; Kloo, L.; Pettersson, H. *Chemical reviews* **2010**, *110*, 6595-663.

(15) Hardin, B. E.; Snaith, H. J.; McGehee, M. D. *Nature Photonics* **2012**, *6*, 162-169.

(16) Gerischer, H.; Michel-Beyerle, M. E.; Rebentrost, F.; Tributsch, H. *Electrochimica Acta* **1968**, *13*, 1509-1515.

(17) O'Regan, B.; Grätzel, M. *Nature* **1991**, *353*, 737-740.

(18) Gust, D.; Moore, T. A.; Moore, A. L. *Accounts of chemical research* **2009**, *42*, 1890.

(19) Hensel, J.; Wang, G.; Li, Y.; Zhang, J. Z. *Nano letters* **2010**, *10*, 478-83.

(20) Delley, B.; Steigmeier, E. *Physical Review B* **1993**, *47*, 1397.

(21) Ledoux, G.; Gong, J.; Huisken, F.; Guillois, O.; Reynaud, C. *Applied Physics Letters* **2002**, *80*, 4834.

(22) Schaller, R.; Klimov, V. *Physical Review Letters* **2004**, *92*, 1.

(23) Schaller, R. D.; Sykora, M.; Pietryga, J. M.; Klimov, V. I. *Nano letters* **2006**, *6*, 424.

(24) Tyagi, P.; Kambhampati, P. *The Journal of chemical physics* **2011**, *134*, 094706.

(25) Beard, M. C.; Knutsen, K. P.; Yu, P.; Luther, J. M.; Song, Q.; Metzger, W. K.; Ellingson, R. J.; Nozik, A. J. *Nano letters* **2007**, *7*, 2506.

(26) Hardman, S. J. O.; Graham, D. M.; Stubbs, S. K.; Spencer, B. F.; Seddon, E. A.; Fung, H.-T.; Gardonio, S.; Sirotti, F.; Silly, M. G.; Akhtar, J.; O'Brien, P.; Binks, D. J.; Flavell, W. R. *Physical chemistry chemical physics : PCCP* **2011**, *13*, 20275-83.

(27) Stubbs, S. K.; Hardman, S. J. O.; Graham, D. M.; Spencer, B. F.; Flavell, W. R.; Glarvey, P.; Masala, O.; Pickett, N. L.; Binks, D. J. *Physical Review B* **2010**, *81*.

(28) Nair, G.; Bawendi, M. *Physical Review B* **2007**, *76*, 5.

(29) Ellingson, R. J.; Beard, M. C.; Johnson, J. C.; Yu, P.; Micic, O. I.; Nozik, A. J.; Shabaev, A.; Efros, A. L. *Nano letters* **2005**, *5*, 865.

(30) Luther, J. M.; Beard, M. C.; Song, Q.; Law, M.; Ellingson, R. J.; Nozik, A. J. *Nano letters* **2007**, *7*, 1779.

(31) Murphy, J. E.; Beard, M. C.; Norman, A. G.; Ahrenkiel, S. P.; Johnson, J. C.; Yu, P.; Mićić, O. I.; Ellingson, R. J.; Nozik, A. J. *Journal of the American Chemical Society* **2006**, *128*, 3241.

(32) Cao, H.; Wang, G.; Zhang, S.; Zhang, X. *Nanotechnology* **2006**, *17*, 3280.

(33) Akhtar, J.; Azad Malik, M.; O'Brien, P.; Wijayantha, K. G. U.; Dharmadasa, R.; Hardman, S. J. O.; Graham, D. M.; Spencer, B. F.; Stubbs, S. K.; Flavell, W. R.; Binks, D. J.; Sirotti, F.; El Kazzi, M.; Silly, M. *Journal of Materials Chemistry* **2010**, *20*, 2336.

(34) Barkhouse, D. A. R.; Pattantyus-Abraham, A. G.; Levina, L.; Sargent, E. H. *ACS Nano* **2008**, *2*, 2356.

(35) Seo, J.; Cho, M. J.; Lee, D.; Cartwright, A. N.; Prasad, P. N. *Advanced materials (Deerfield Beach, Fla.)* **2011**, *23*, 3984.

(36) Ip, A. H.; Thon, S. M.; Hoogland, S.; Voznyy, O.; Zhitomirsky, D.; Debnath, R.; Levina, L.; Rollny, L. R.; Carey, G. H.; Fischer, A.; Kemp, K. W.; Kramer, I. J.; Ning, Z.; Labelle, A. J.; Chou, K. W.; Amassian, A.; Sargent, E. H. *Nature nanotechnology* **2012**, *7*, 577-82.

(37) Nanoco Technologies Ltd http://www.nanocotechnologies.com/index.aspx (accessed Mar 27, 2011).

(38) Khan, A. *Nature* **2006**, *441*, 299.

(39) Suzuki, K.; Kanisawa, K. Imaging of Quantum Confinement and Electron Wave Interference | NTT Technical Review https://www.ntt-review.jp/archive/ntttechnical.php?contents=ntr200808sp2.html (accessed Sep 29, 2013).

(40) Beard, M. C.; Ellingson, R. J. *Laser & Photonics Review* **2008**, *2*, 377.

(41) NREL: National Center for Photovoltaics Research Cell Efficiency Records, accessed 16/09/2013 http://www.nrel.gov/ncpv/ (accessed Sep 16, 2013).

(42) School of Photovoltaic and Renewable Energy Engineering - University of New South Wales Third Generation Photovoltaics http://www.pv.unsw.edu.au/Research/3gp.asp (accessed Mar 23, 2011).

(43) Steve Byrnes's Homepage http://sjbyrnes.com/ (accessed Sep 28, 2013).

Chapter 2: Techniques and Instrumentation

2.1 X-ray Diffraction (XRD)

X-ray diffraction (XRD) is a useful tool for gaining information on the crystallographic structure, crystallinity, crystal size and preferred orientation of a sample. By subjecting a sample to a beam of X-rays and measuring the intensity of X-rays reflected with respect to angle, a distinct diffraction pattern for the sample can be obtained, analogous to a fingerprint. By comparing the diffractograms to known diffraction patterns for specific elements or compounds, information regarding the shape of the unit cell of the crystal lattice can be determined, with each peak corresponding to a specific lattice plane. Information regarding the size of crystallites present can be obtained when analysing samples containing crystallites with diameters less than 500 nm due to a characteristic broadening of the diffraction peaks that occurs at these sizes[1].

2.1.1 – Theory

Crystalline solids are typically defined *via* the use of a 'unit cell', which represents the smallest repeating structure within the solid. The unit cell is defined in terms of its lattice parameters, which describe the length of the sides of the unit cell and the angles between them. The 'basis' of a crystal is the set of atoms that are repeated throughout the crystal, occurring at each lattice point within the unit cell (where the lattice points depend on the bravais lattice of the crystal). Within a crystalline solid it is possible to imagine various families of planes which pass through its unit cell at various angles. In order to define the geometry of these planes, Miller indices are used; a set of three numbers (when considering three dimensions) typically labelled h, k, and l, corresponding to the vector normal to the plane(s) they describe (figure 2.1).

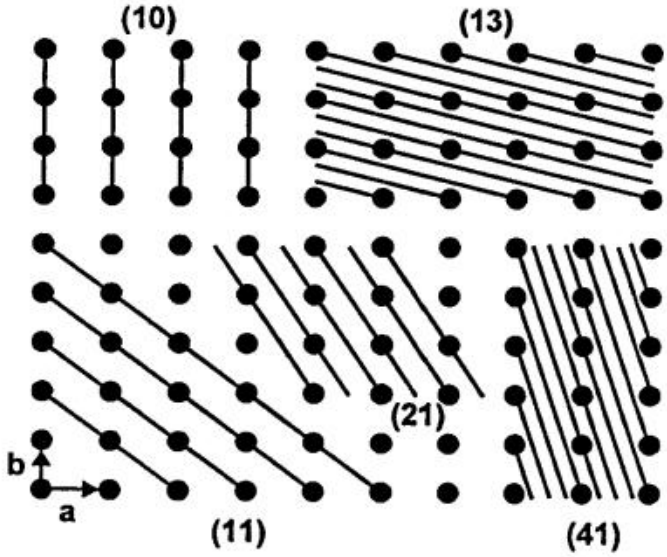

Figure 2.1: An example of Miller indices in two dimensions[2]. The vectors 'a' and 'b' are the lattice parameters of the unit cell.

When X-rays are incident upon a crystalline solid, the photons will reflect from the atoms in such a way that the crystallographic planes described earlier can be treated as analogous to a set of parallel reflective planes in optics. A set of parallel reflective planes subject to a beam of electromagnetic radiation will act in a manner similar to a diffraction grating, as shown in figure 2.2.

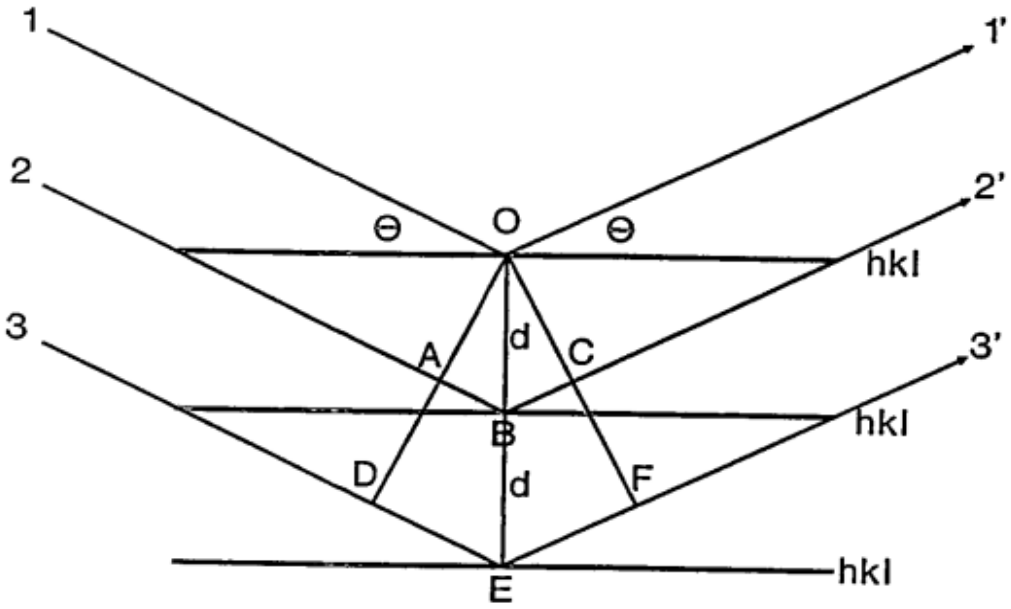

Figure 2.2: A crystal lattice can be shown to cause diffraction by to a set of reflective planes[2].

Incoming electromagnetic radiation reflecting off different planes within the lattice will result in a path length difference through basic geometry; it is clear from Figure 2.2 that ray 2 will have travelled a greater distance than ray 1, with the difference being equivalent to the length of ABC. It is also apparent that ray 3 will travel the further by the same amount again. Thus when the distance ABC is equal to one wavelength of the incident radiation, the distance DEF (the path length difference between rays 1 and 3) will be equal to two wavelengths, and so on through the crystal. The distance ABC is dependent on the spacing between the planes, *d*, and the sine of the angle of the incident radiation, θ. AB and BC are equal, and since

$$AB = d\sin(\theta) \tag{1}$$

it is simple to determine that

$$ABC = 2d\sin(\theta) \quad . \tag{2}$$

When constructive interference occurs, the path length difference ABC must be equal to a multiple of the wavelength, λ. This results in Bragg's Law:

$$n\lambda = 2d\sin(\theta) \quad . \tag{3}$$

This law is the fundamental principle behind the use of X-ray diffraction to determine crystallographic structure of samples. By analysing the diffracted intensity of X-rays over a range of angles, various parameters of the crystal lattice can be determined. Specifically, it is possible to determine which crystallographic planes predominate in the sample, with each peak in X-ray intensity corresponding to a particular plane. This is useful in the characterisation of differing structures of the same substance – for instance, if the sample was formed in a way which results in preferential growth along a specific plane, the diffraction pattern will show this.

Typically, X-ray diffraction is performed upon powdered samples. In this case, the crystals within the sample can be treated as being randomly oriented, and the ratios of X-ray intensities of each reflection relative to that reflection's intrinsic intensity will correspond to the proportions of planes present on the exposed crystal faces. X-ray diffraction can also be performed on 'textured' samples, i.e. those with some form of preferential orientation, such as thin films. Direct quantitative analysis of the sample is

difficult in this case, as certain planes will be more prevalent in the resulting diffraction pattern. Finally, X-ray diffraction can also be performed upon single crystals, however this requires large individual crystals to be formed.

2.1.2 - Method and Equipment

A typical X-ray diffractometer has three key parts; an X-ray source, a sample stage, and a detector. A typical X-ray source will consist of a filament, usually made of tungsten, and an anode, often made of copper, although other elements can also be used. The process of generating X-rays is relatively simple; a current is passed through the filament in order to excite its electrons, which are emitted from the filament inside a vacuum tube. These electrons, incident upon the anode, produce X-rays via a combination of several effects. A continuous background spectrum of X-rays is emitted due to the Bremsstrahlung effect – as the electrons are decelerated in the potential of the anode, they emit electromagnetic radiation at various wavelengths. Specific 'characteristic peaks' in the intensity of emitted X-rays are also produced, so-called as they are dependent upon the element used as the anode (figure 2.3).

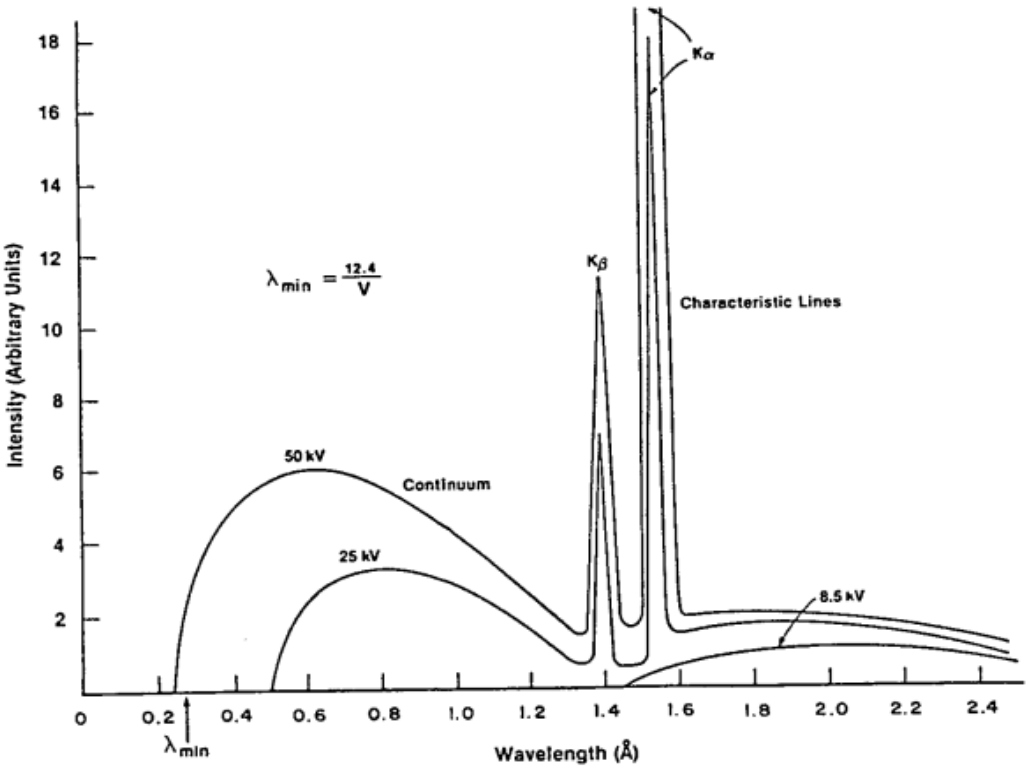

Figure 2.3: Example spectrum of X-rays produced by electrons incident upon an anode, consisting of a broad Bremsstrahlung background and sharp characteristic peaks[2].

These characteristic peaks are produced by specific energy level transitions within the anode. When an incident electron or photon has enough energy, they may excite one of the electrons within the anode, ejecting it from its orbital. If this occurs, it will leave behind an empty state, which will shortly be filled by an electron from a higher energy level taking its place. This electron must therefore lose some energy in the course of dropping down to fill the lower orbital. This energy can be emitted in one of two forms – either as a characteristic X-ray photon, or by the emission of another electron in an outer orbital in a process known as the Auger effect (figure 2.4).

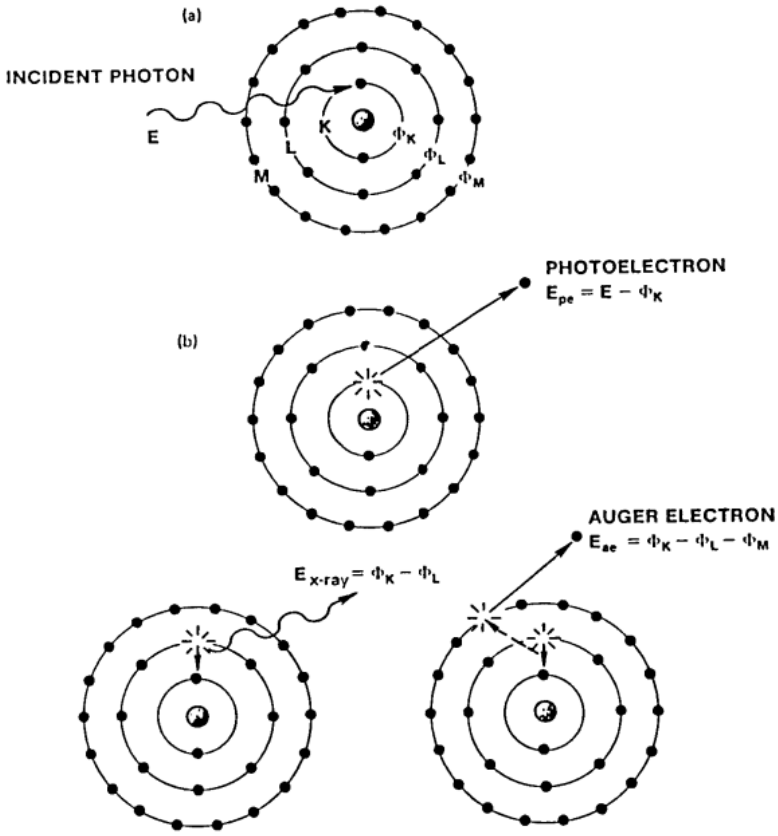

Figure 2.4: Diagram showing the two competing effects after the emission of a core electron - emission of an X-ray photon on the left, and emission of an Auger electron, on the right[2].

The Auger effect thus acts to reduce the overall intensity of produced X-rays. The probability of an Auger electron being emitted increases as atomic number, Z, decreases, and thus X-ray production is limited for elements with lower Z. Production of X-rays is typically inefficient, with as little as ~1% of incident electron energy resulting in production of X-rays[2]. Most of the remaining energy is converted to heat, thus the cooling of the anode is extremely important. Copper is often used as an anode, as not only does its high thermal diffusivity aid in the cooling process, but the wavelength of its Kα line is one of the best suited for general XRD use.

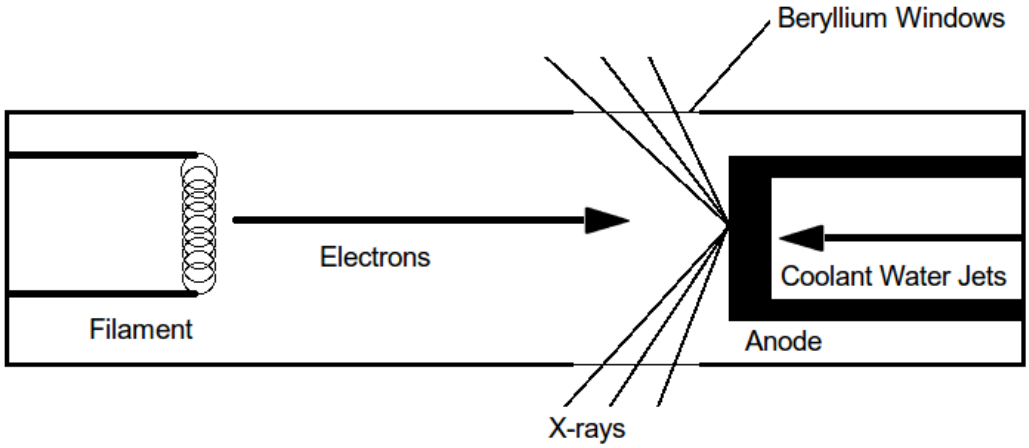

Figure 2.5: Simplified diagram of a typical X-ray tube.

The structure of an X-ray tube will usually consist of the filament and anode at opposite ends of the vacuum chamber, with beryllium windows placed so as to limit the direction of emitted X-rays (figure 2.5). The anode is often placed at an angle such that X-rays which pass through the windows have all originated from an approximately equal depth within the anode, preventing what is known as 'anode heel effect' – where the X-ray intensity is uneven across the profile of the beam. Together with water constantly sprayed on the rear of the anode, some X-ray tubes incorporate a rotating anode, such that only a small portion of it is exposed to the electron flux at any one time in order to prevent the anode getting too hot.

Many diffractometers contain a monochromator either between the X-ray tube and the sample stage, or between the sample stage and the detector, with the latter being more common[2]. The purpose of a monochromator is to remove as much of the unwanted Bremsstrahlung radiation as possible and any characteristic lines other than the $K\alpha_1$. Allowing the full $K\alpha_1 - K\alpha_2$ doublet through is sometimes preferred, however, when signal to noise ratio is considered of greater importance than resolution[2]. An X-ray monochromator typically consists of a quartz crystal with a well-known diffraction pattern, placed at an appropriate point in order to diffract only radiation of the desired wavelength through the remainder of the system (figure 2.6).

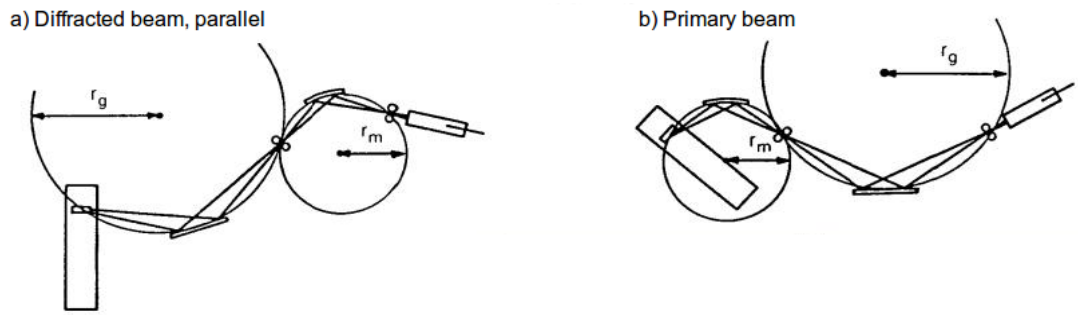

Figure 2.6: a) A monochromator located after the sample stage. b) A monochromator located before the sample stage[2]

The monochromator is usually mounted as a part of either the detector or source, one or both of which are mounted on motorised arms. These arms themselves are mounted as part of a circular stage, forming the core of the diffractometer. This arrangement is known as a goniometer – the detector and/or X-ray source moves across the range of angles specified by the user, mapping out the angular distribution of X-rays diffracted from the sample. The user is able to control both the step size between points of data collection and the duration of data collection, allowing the angular resolution of the resultant plot to be controlled up to the resolution limit of the detector (figure 2.7).

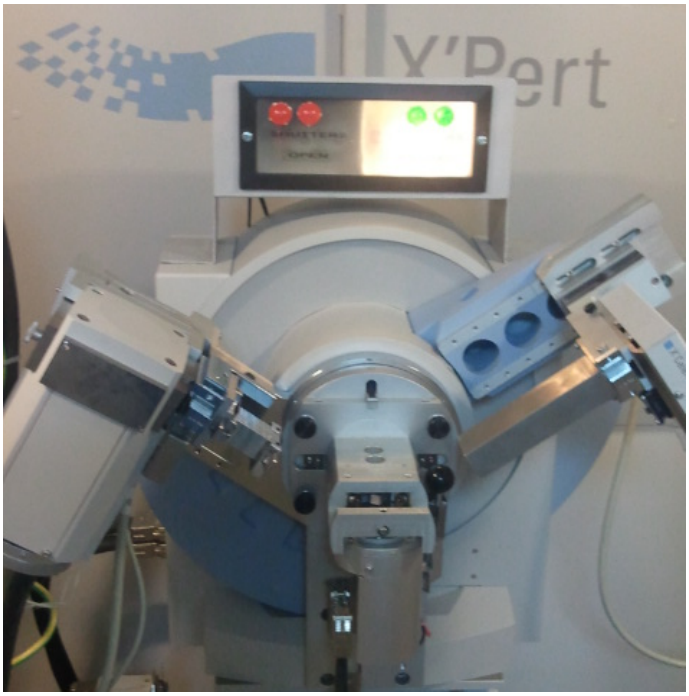

Figure 2.7: Picture of a typical goniometer sample stage.

Several types of detector used in modern diffractometers, however most operate on similar principles. All must consist of an X-ray-sensitive element which, upon interaction with an X-ray, will produce some form of signal proportional to the energy of the X-ray. Many include some form of amplification step between production of this initial signal and output to a computer. One of the most common types of detector used, and an excellent example of the principles, is a scintillation counter. Such a detector consists of a sheet of phosphor (commonly thallium-doped sodium iodide[2]) attached to a photomultiplier tube. Upon impact by an incident X-ray, the phosphor is excited, before re-emitting the light in the form of several lower-frequency photons. Each of these photons will subsequently impact upon the cathode of the photomultiplier tube, exciting an electron via the photoelectric effect. This electron then passes through a series of ~10 dynodes within the tube, each with a higher potential than the last, which accelerate the electron down the tube. Upon impact with each dynode, the electron will excite more electrons using the kinetic energy gained from its acceleration through the tube, eventually resulting in a pulse of current at the anode (figure 2.8).

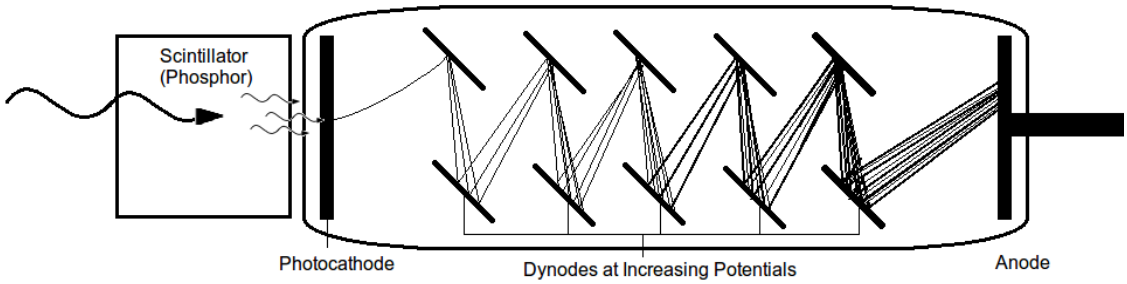

Figure 2.8: Diagram of a basic Scintillation Counter

2.1.3 - Analysis

Analysis of an XRD pattern often relies substantially on prior knowledge about the likely composition of a sample; with this knowledge, however, the process of analysis is relatively simple. The International Centre for Diffraction Data provides a database of powder diffraction files (PDFs) which are incorporated into many of the avilable analysis programs that exist (figure 2.9). Regardless of the software used, the basic principle is the same; the diffraction pattern obtained is compared to the PDF's of the likely elements and

compounds present in the sample, and based on this comparison conclusions can be drawn about the structure of the sample.

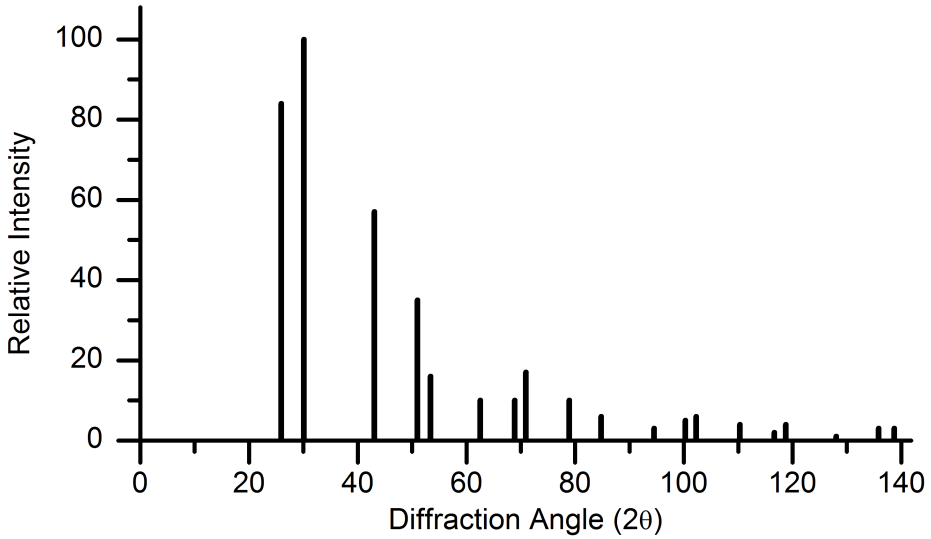

Figure 2.9: The powder diffraction file of lead sulfide[31]. Each line represents a specific reflection and their typical relative intensities in a randomly oriented sample[28].

Other factors that must be considered when analysing an XRD pattern are the broadening of peaks due to crystallite size, sample orientation, and, often, the presence of the $K\alpha_2$ shoulder in the data. As the wavelength of the $K\alpha_2$ (0.154439 nm) line is slightly different to the wavelength of the $K\alpha_1$ (0.154056 nm) line, they are only diffracted to slightly different angles. This results in a small shadow peak appearing next to every primary peak in the resultant XRD pattern often as a shoulder on the primary peak. Most XRD analysis software is capable of subtracting this shoulder, since the $K\alpha_1$ and $K\alpha_2$ lines form a doublet, and thus have fixed relative intensities.

Peaks in XRD spectra can be broadened by a number of factors, including broadening based on the instrument and broadening due to strain within the sample. Of more interest, however, is peak broadening due to crystallite size. When the crystallites within a sample are below approximately 500 nm in size[1] then the decreased periodicity in diffracting domains results in a broadening of the final diffraction peak. This effect is described by the Scherrer Formula:

$$\tau = \frac{K\lambda}{\beta \cos\theta} \quad , \qquad (4)$$

where τ is the average crystallite size, K is the shape factor, λ is the wavelength of the incident radiation, β is the line broadening at the full width half maximum of the peak, and θ is the diffraction angle[3]. This effect is useful in that it can act as a rough gauge of crystallite size in the sub-micron range. It is worth noting that this is not a reliable method however, as the shape factor, K (which is typically around 0.9 for approximately spherical particles) is fairly arbitrary due to the inherent complexity involved in characterising the shape of particles present. It will also only ever provide a lower bound for particle size, as the crystallite size in the formula refers to the size of individual diffracting crystal domains within the sample. This is often equivalent to particle size, but in the case of particles composed of multiple crystal domains, the particle size may be many times larger than the domain size.

2.2 High and Ultra-high Vacuum

Ultra-high vacuum (UHV) is a term used to refer to a vacuum with pressures less than ~10^{-9} mbar. In many techniques, pressures between 10^{-3} and 10^{-9} mbar are required – known as high vacuum - typically to minimise interactions between air and whatever particles are used in the technique (e.g. electrons). Ultra-high vacuum is required in circumstances where the rate of contamination of a surface must also be minimised, for example in surface-sensitive spectroscopy such as X-ray photoelectron spectroscopy (XPS) and Auger electron spectroscopy (AES), or for thin-film deposition techniques requiring high purity, such as molecular beam epitaxy or chemical vapour deposition.

To achieve UHV is not a simple task; material requirements alone are more stringent than those required for high vacuum. Metals such as aluminium and palladium cannot be used within the chamber, as their ability to absorb water causes them to act as a constant source of pressure within the system – known as 'outgassing'[4]. The permeability and absorption of metals used must therefore be considered when constructing a chamber for UHV. Chambers for UHV must also be 'baked' at over 100 ºC before use in order to remove potential sources of outgassing. Gaskets used for UHV are in general made of high purity copper, and are typically only used once. Even the construction methods used

must be taken into account – standard welding will often leave voids in the material which will hold air and act as a source of outgassing when the chamber is pumped down.

Construction of a suitable chamber is not all that is required to achieve UHV however; standard mechanical pumps will usually only be capable of achieving pressures of ~10^{-5} mbar, and often become inefficient at higher pressures[4]. Pumps capable of efficiently pumping to UHV pressures however are often incapable of dealing with atmospheric pressures, often suffering damage if exposed to high pressures while in operation. Many systems requiring UHV therefore have a combination of standard mechanical pumps and pumps capable of reaching UHV, with the UHV pumps only being used once a good enough vacuum is reached. Often, such systems will often have separate chambers which these pumps are attached to, acting as airlocks for the sample such that the pumps in the UHV chamber need never be switched off. This type of arrangement can vastly improve the speed at which samples may be exchanged, lowering the required time to perform experiments, and thus are quite common. An explanation of some of the more common pumps and gauges used to achieve UHV follows.

2.2.1 – Rotary Pumps

One of the most common mechanical pump designs is the rotary pump. At its most basic, a rotary pump consists of an asymmetric vane immersed in oil, with inlet and outlet ports perpendicular to its axis of rotation. This vane acts to compress incoming gases and sweep them towards the outlet. Rotary pumps are often used to initiate pumping down from atmosphere and often to 'back' other pumps – placed behind another pump in series, they remove the output of a pump capable of reaching lower pressures.

2.2.2 – Turbomolecular Pumps

A turbomolecular pump is a form of mechanical pump, capable of achieving UHV conditions starting from atmospheric pressure. They must always be backed by another pump, however, as they will stall if their outlet is at atmospheric pressure.

A turbomolecular pump consists of a series of alternating rotors and stators decreasing in size, with their blades at alternating angles. Thus, when the rotors rotate they impart kinetic energy to the gas in the direction of the stator blades, which then deflect the gas

molecules towards the next, smaller, rotor. This acts to produce a series of pressure differentials between each set of rotors and stators, evacuating the gas.

2.2.3 - Diffusion Pumps

A diffusion pump operates *via* removal of molecules that diffuse into it. At the top of a diffusion pump is a throat leading to the chamber to be evacuated. Gas molecules diffuse into this throat, where they are caught by jets of hot oil vapour, sprayed downwards from a set of conical openings on a central chimney. This vapour is then cooled and condensed by cooling coils around the outside of the pump; the oil and any captured gas is thus brought to the base of the pump where the oil is reheated by a heater and the gas is removed by a backing pump. Diffusion pumps usually have a liquid nitrogen trap at the top of their throat – a region cooled to low temperatures, in order to prevent hot oil vapour from flowing into the chamber. Diffusion pumps are fairly durable, and can, under good conditions, be used to pump down from ~10^{-2} mbar to almost UHV conditions.

2.2.4 - Ion Pumps

An ion pump operates by producing a cloud of electrons at an anode, which impact upon gas molecules that pass through, ionising them. These ionised gas molecules are then accelerated towards the cathode, where they impact upon the surface and are chemically bound into it, effectively removing them from the system. Ion pumps can pump from 10^{-3} to 10^{-11} mbar, but can be damaged by exposure to higher pressures. The process involved in ion pumping can also be used as a gauge – the current produced at the cathode is directly proportional to the number of gas molecules impacting upon it, which is itself proportional to the density of gas molecules present. A gauge of this type is known as a Penning gauge.

2.2.5 – Titanium Sublimation Pumps

Titanium sublimation pumps (TSPs) do not act continuously like other pumps, rather, they can be 'fired', which each firing acting to reduce the pressure within the chamber. When fired, a current is passed through a titanium filament, subliming a cloud of ultrafine titanium particles into the chamber, which rapidly attach to the chamber walls. Gas molecules present react with this titanium layer, either while it is passing through the

chamber, or, more likely, on the surfaces of the chamber walls. The gas molecules are thus chemically bound to titanium on the walls of the chamber, effectively removing them from the system and reducing the pressure.

2.2.6 – Pressure Gauges

There are two commonly used types of gauge. At higher pressures, from atmospheric to ~10^{-3} mbar, Pirani gauges are usually used. A Pirani gauge consists of a heated filament – in the regime where convection is the dominant source of heat loss of the filament, any decrease in chamber pressure will result in a corresponding effect on the rate of change of temperature of the filament. This can continue to provide an accurate measure of the pressure until convection is no longer the dominant source of heat loss, at around 10^{-3} mbar. Below this pressure, the most commonly used type of gauge is the Penning gauge, described above – this gauge is effectively the same as an ion pump in operation, and both functions are often combined in one device.

2.3 Scanning and Transmission Electron Microscopy (SEM/TEM)

Electron microscopy, developed as a tool in the mid-1900's[4], can greatly surpass the limits present in optical microscopy, allowing the observation of objects even down to a few ångstroms in size. There are two ways in which an electron microscope can function; the most analogous to traditional optical microscopy is transmission electron microscopy (TEM), in which electrons are passed through a sample to form an image upon a fluorescent screen in a similar manner to photons of light in an optical microscope forming an image on the retina. Scanning electron microscopy (SEM) operates in a different manner, relying on electrons scattered from the sample in order to form an image. This has the added advantage of producing images that appear more 3-dimensional than those obtained by other methods – their enhanced depth of field results in a thicker portion of a sample being in focus at any one time[4]. These capabilities render electron microscopy an extremely useful tool in the analysis of nanometre-scale surfaces.

2.3.1 – Electron Microscopy Theory

Conventional microscopy is limited in resolution by several factors, but the effective 'hard' limit (i.e. that which cannot be easily circumvented through ingenuity) is caused by

diffraction of light as it passes through the lens, limiting the minimum focal spot size that can be formed. For a microscope used for observing waves of wavelength λ, the smallest resolution achievable, in the absence of other sources of distortion, is given by

$$d = \frac{0.612\,\lambda}{n \sin \alpha} \qquad (10)$$

where n is the refractive index of the medium through which the wave is travelling, and α is the aperture angle. De Broglie's theory of wave-particle duality implies that electrons have their own, extremely short, wavelengths which can be calculated from their energy. This leads to the use of electron beams in microscopy, greatly reducing this diffraction limit, and allowing much smaller distances to be resolved.

2.3.2 – SEM

Instead of the beam passing through the sample to be observed and detected on the other side, a SEM detects the electrons released from the sample as a result of ionisation by the beam, known as 'secondary' electrons. These electrons are used to produce a signal which when plotted against the coordinates from which the electrons were emitted, produces a graph of intensity against position. By translating these data into pixel brightness, an 'image' of the sample is obtained. An entire sample cannot be imaged in this way instantaneously – the data for each position must be collected separately. The electron beam and detector are synchronised to raster over the surface together, taking data for each point at a time.

In addition to proximity to the detector, the intensity produced from a given point on the sample is increased or decreased by the local topology – peaks produce higher intensities of detected electrons than plateaus or valleys. This is due to the fact that secondary electrons are not just produced from the surface; the incident electrons interact over a teardrop shaped area known as the interaction volume, as shown in figure 2.10. Raised areas thus have a greater proportion of this volume close enough to the surface for electrons to escape, resulting in a higher signal.

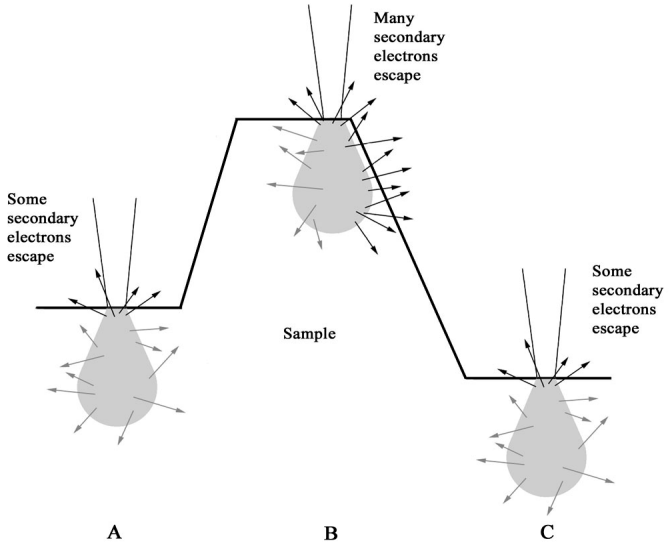

Figure 2.10: Diagram showing how the SEM 'edge effect' results in increased signal intensity from slopes[26].

As the electron beam is typically very narrow, there is a region either side of the beam focus in which the divergence of the beam is not enough to cause blurring between pixels. Any material within this depth range will therefore appear 'sharp' and as if in focus; this is what causes the large depth of field achieved in SEM (figure 2.11). All of these effects combined result in the characteristic 3-dimensional appearance of SEM images, such as that shown in figure 2.12.

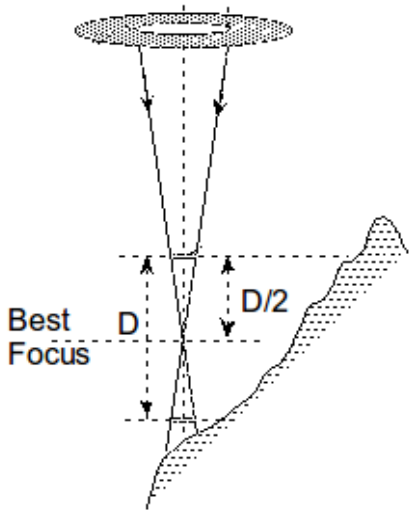

Figure 2.11: Diagram showing depth of field, where D is depth of field. D/2 is the depth before beam widening results in blurring between pixels (adapted from [24]).

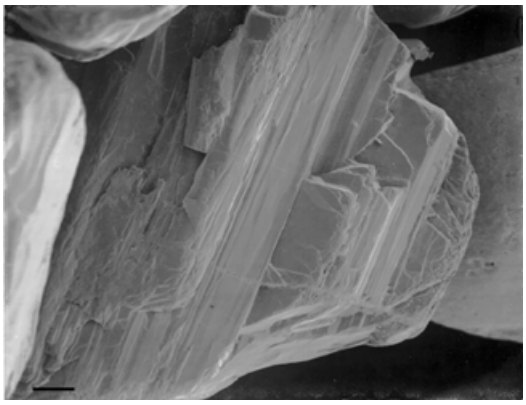

Figure 2.12: An SEM micrograph of a sand grain, showing the depth of field characteristic of SEM and the edge effect[26].

Both SEM and TEM must be performed at high vacuum in order to prevent electron interactions with gas molecules, which would block both the electron beam and secondary electrons emitted from the sample. The basic structure of electron microscopes of either type usually consists of a loading chamber for samples and a main chamber kept at HV. Within the main chamber, the apparatus used is very similar to devices discussed earlier. Electrons are typically produced in the same manner as in an X-ray tube – *via* thermionic emission from a tungsten filament. The tungsten filament is usually followed by a device known as a Wehnelt cylinder – kept at a slightly higher negative potential than the filament itself. This cylinder acts to focus the electrons through its aperture and help accelerate them towards a grounded anode. Whereas in an X-ray tube the anode is used as a target for the electrons to interact with, in an electron microscope it is used to accelerate the electron beam and repel some low-energy background electrons.

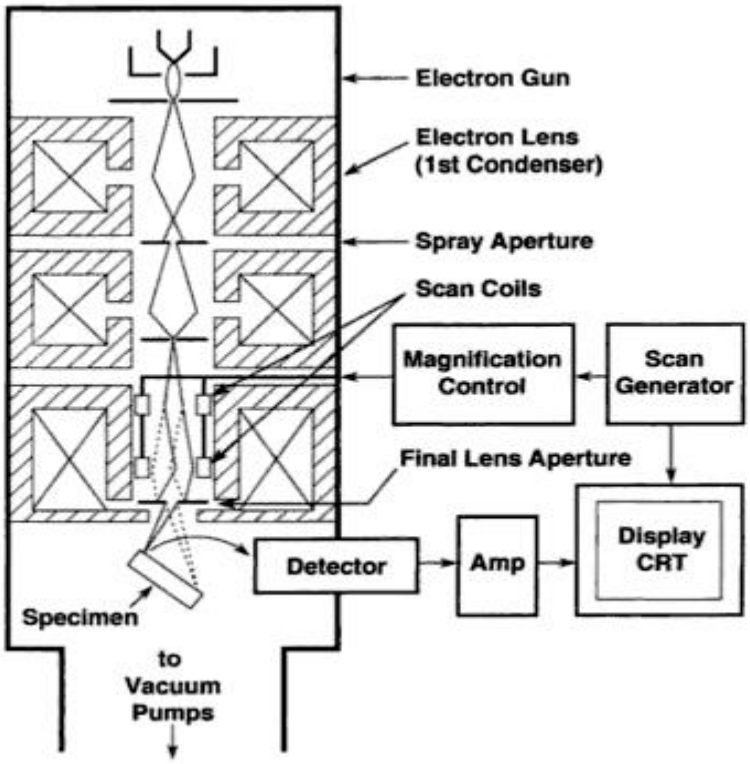

Figure 2.13: Diagram of an SEM column showing the arrangement of the magnetic lenses used to focus the beam[25].

After the beam passes through the aperture of the anode, it passes through two sets of magnetic condenser lenses which focus the beam before passing it through spray apertures that 'trim off' non-homogeneous and scattered electrons from the beam[4] (figure 2.13). Apertures are also used in order to reduce spherical aberration in the final lens. The 'lenses' are typically electromagnets with alterable currents so as to move their focal point; this can also be achieved by moving fixed-field magnets, but only in the case of relatively low beam energies.

After passing through condensers and apertures in order to refine the beam, stigmators may be used in order to correct for a non-circular beam profile before the beam hits the sample. The final lens is used to focus the beam upon the sample, and adjusting the position of the final lens aperture can also be used to alter the depth of field – in figure 2.11 it is clear that a change in relative position of the aperture and beam focus would result in a narrowing or widening of the beam, changing D, the depth of field.

Once the electrons have interacted with the sample, the secondary electrons are accelerated towards the detector by a potential applied between it and the sample. The

detector itself is often a scintillation counter similar to the one described in section 2.1.2, with a scintillator material appropriate to the electron beam.

2.3.3 TEM

TEM is of great use for the investigation of nanoscale samples, as it provides imaging at a resolution superior to the resolution achievable using a scanning-electron microscope. In principle, atomic resolution is achievable. Conventional TEM operation is analogous to that of a typical optical microscope; a beam of electrons is focussed upon a sample and the intensity of the transmitted beam is detected and forms an image of the sample with contrast dependent on thickness (though other forms of contrast are also possible). The electron beam is focussed through a series of lenses formed by magnetic and electrostatic fields in much the same way as that described for an SEM . A schematic diagram of a typical TEM is shown in figure 2.14.

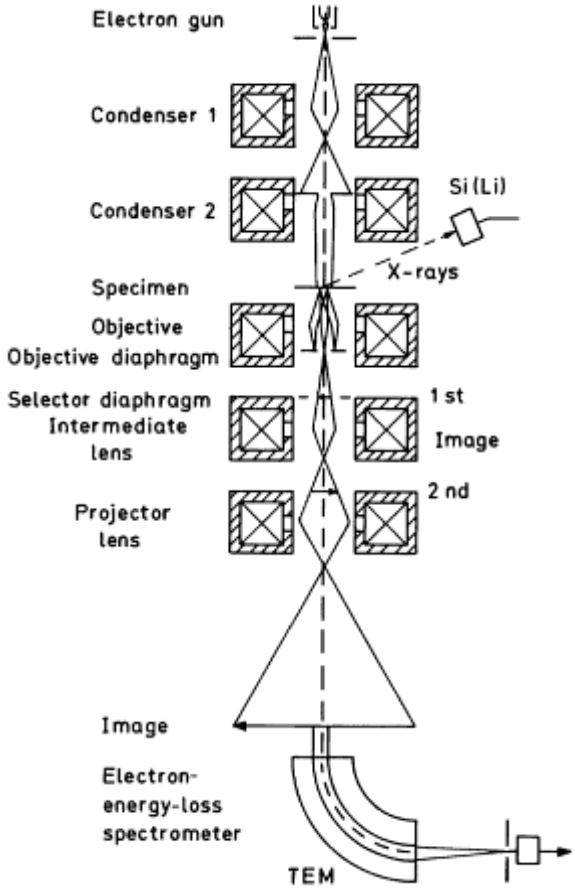

Figure 2.14: Schematic ray diagram for a TEM equipped with electron-energy-loss and X-ray spectrometers. Typically a TEM may contain an interchangeable fluorescent screen and CCD where the image is formed[23].

As with SEM, TEM must be performed at high vacuum in order to prevent rapid destruction of the electron gun filament and to ensure a high electron mean-free-path. Samples are typically mounted on thin copper grids, and must be thinned to ≤ 100 nm in thickness to allow transmission of electrons (dependent on the beam energy). In TEM, focus is achieved by alteration of the electrostatic and magnetic fields used to control the electron beam. Typically TEM micrographs are taken with a slight underfocus, as the contrast at perfect focus is lower. Slightly defocussing the image produces Fresnel fringes at sample edges as seen in figure 2.15, providing increased contrast with little appreciable loss of resolution. Fresnel fringes are formed by interference between the undiffracted beam and rays that pass close to an edge and are diffracted.

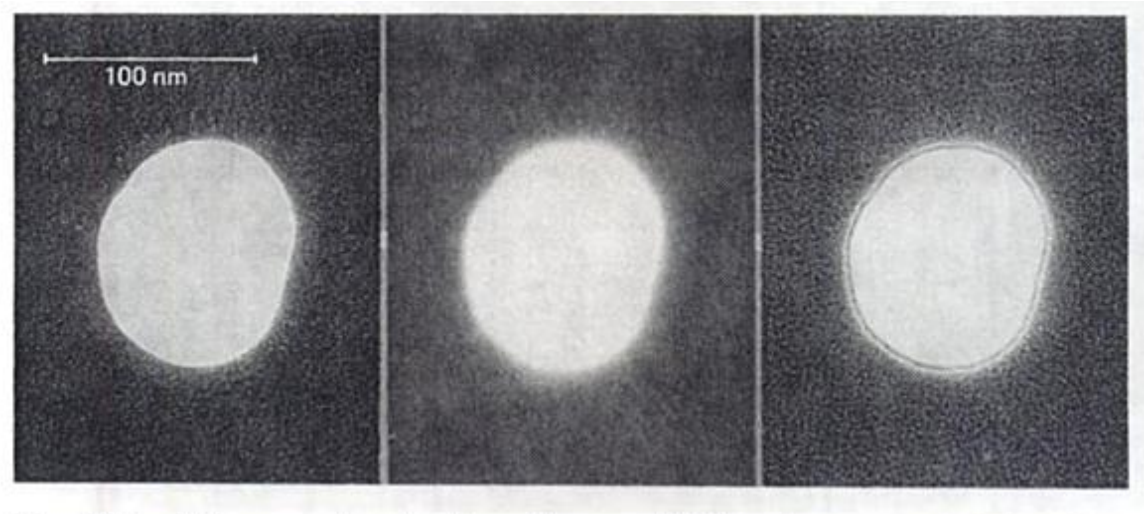

Figure 2.15: From left to right: Underfocussed, focussed, and overfocussed TEM images[30].

2.4 X-ray Photoelectron Spectroscopy (XPS)

X-ray photoelectron spectroscopy (XPS) is a technique commonly used for the analysis of surfaces. XPS can provide complex quantitative information about the chemical and electronic states and the proportion of elements at the surface of a sample, as well as how these properties vary over the first 2-10 atomic layers[5]. XPS is based upon the X-ray induced photoemission of electrons; by measuring the intensity of emitted electrons over a range of kinetic energies, spectra are produced. Using these spectra, specific peaks corresponding to the electron shells of elements present can be quantified, and their chemical state identified.

2.4.1 - Theory

The production of a photoelectron occurs when photons of sufficient energy incident upon a surface result in the excitation of an electron due to the photoelectric effect. This process can be described by the equation

$$E_\gamma = E_K + E_B + \phi \tag{5}$$

where E_γ is the energy of the exciting photon, E_K is the kinetic energy of the emitted electron, E_B is the binding energy of the electron, and φ is the work function of the material[6]. In the case of a typical XPS set-up with a conductive sample, the sample and spectrometer are placed in electrical contact which results in their Fermi levels being at the same energy. The advantage of this is that when calculating the binding energy of the electrons that are detected, only the work function of the spectrometer need be considered[6]. A side effect of the XPS process is the production of Auger electrons (as mentioned earlier in section 2.1.2). In the Auger process a core electron removed from an atom will leave behind an empty state, and it is possible for an electron from a higher energy state to drop down to fill the empty state. When this occurs, an amount of energy equal to the transition between the two states must be released, usually either in the form of a photon, or as another electron being expelled from the atom as shown in figure 2.16.

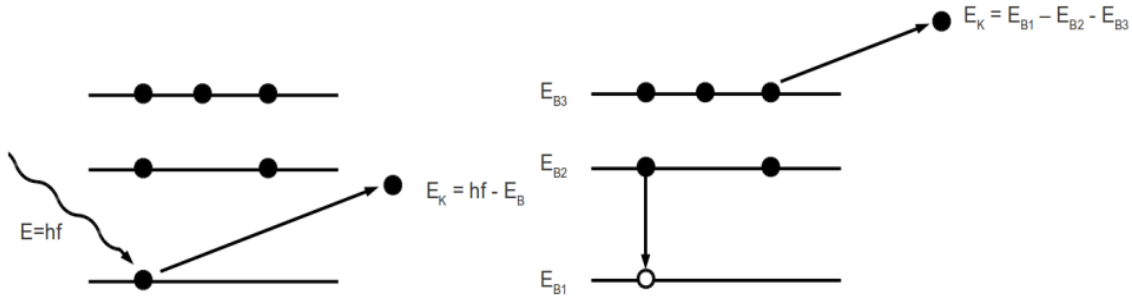

Figure 2.16: a) Diagram of the process of photoemission. b) Diagram of the emission of an Auger Electron.

As the Auger effect is caused by transitions between specific atomic energy levels, each transition will result in an electron with a specific kinetic energy. Both photoemission and the Auger effect can produce high intensities of emitted electrons at well-defined

energies.

The majority of photoelectrons leaving the sample suffer inelastic collisions while exiting the sample; electrons that have undergone inelastic collisions are known as 'secondary electrons' and do not provide useful analytical information, instead forming a part of the background. Those electrons which do not suffer inelastic collisions are referred to as 'primary' electrons and it is these that provide the desired signal. The X-rays used in photoemission experiments are capable of penetrating to a depth that is orders of magnitude larger than the depth from which electrons can escape, and thus there is little change in the X-ray intensity over the thickness of sample from which primary electrons originate. The sample can therefore be considered as an electron source with (approximately) fixed intensity, I_0 [6] originating from beneath a thin layer (d) of the sample which acts to attenuate the emitted electrons. We can therefore use Beer's Law, below, to describe the intensity loss over the depth of the sample,

$$I_T = I_0 e^{(-d/\lambda \cos\theta)} \qquad (6)$$

where I_T is the transmitted electron intensity, λ is the inelastic-mean-free-path, and θ is the angle between the path of the electron and the normal to the sample surface. Thus the sample depth which may be probed is primarily dependant on the inelastic-mean-free-path (IMFP) of the electron within the sample, defined as the depth of sample over which the photoelectron flux is reduced to 1/e, ~37%, of its original value. This itself is heavily dependent on the kinetic energy of the electron, as shown in figure 2.17.

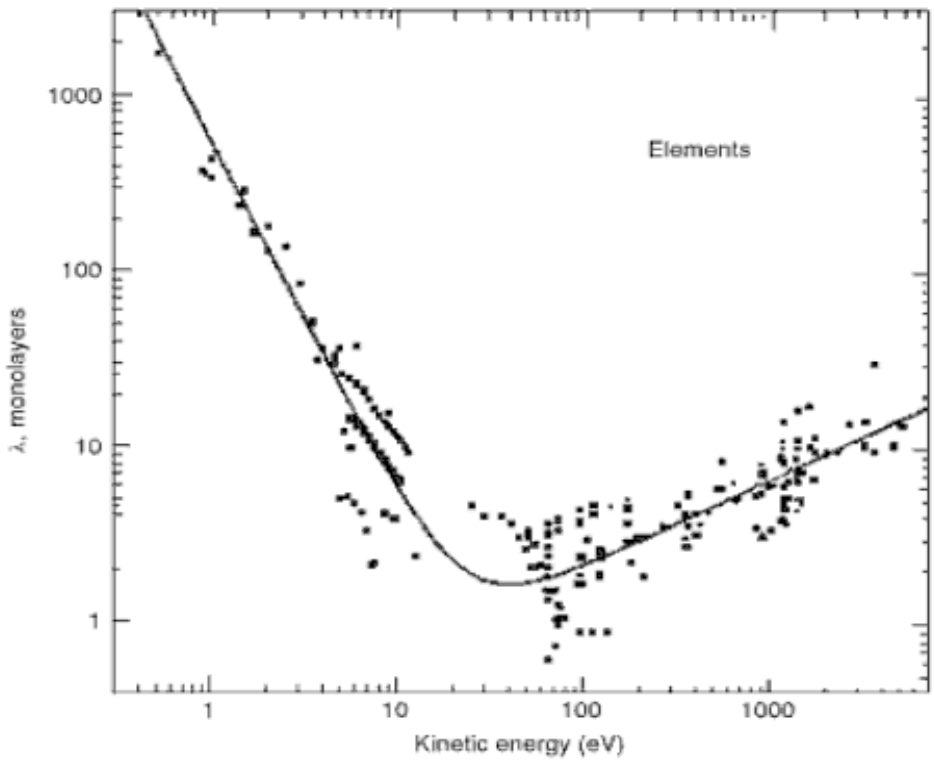

Figure 2.17: Relationship between electron kinetic energy and inelastic-mean-free-path[5].

It can be seen from figure 2.17 that over most of the energies probed by XPS (i.e. from ~10-1500 eV), those electrons with higher kinetic energy will be able to penetrate further. The increase in IMFP below ~10 eV is due to the electrons having insufficient energy to interact with the valence electron plasmons within the sample, thus decreasing the likelihood of inelastic collisions. Above the minimum at ~50 eV, it can be inferred that electrons with a higher kinetic energy (i.e. those with lower binding energies) will be able to be detected from deeper within the sample. This allows depth analysis to be performed, allowing information on the relative concentrations of different chemical states over the first few nm of sample to be obtained.

2.4.2 - Analysis

There are many features to be considered in the analysis of XPS spectra in order to correctly characterise the sample. The background count rate of the spectra is mostly due to inelastically scattered electrons from the sample, and thus increases towards the lower

kinetic energy end of the spectrum, with step increases at each peak. Primary photoelectron peaks can be represented by a convolution of a Lorentzian and a Gaussian lineshape. The Gaussian portion derives from instrumental factors, whereas the Lorentzian contribution is due to the core hole lifetime of the state. The effect of this is to alter the full-width-half-maximum (FWHM) of the Lorentzian portion of the peak by an amount given by the uncertainty principle:

$$\Gamma \approx \frac{h}{\tau} \qquad (7)$$

where Γ is the FWHM, h is Planck's constant, and τ is the core hole lifetime.

Peaks in a spectrum often consist of multiplets, each separate peak corresponding to a different chemical or electronic state of the element in question. Deconvoluting these peaks allows analysis of the proportions of the various states that are present. The process involved in fitting these peaks is made substantially simpler by the use of fitting software which automates much of the procedure, however a certain level of expertise is required to determine whether a given fit is realistic (figure 2.18).

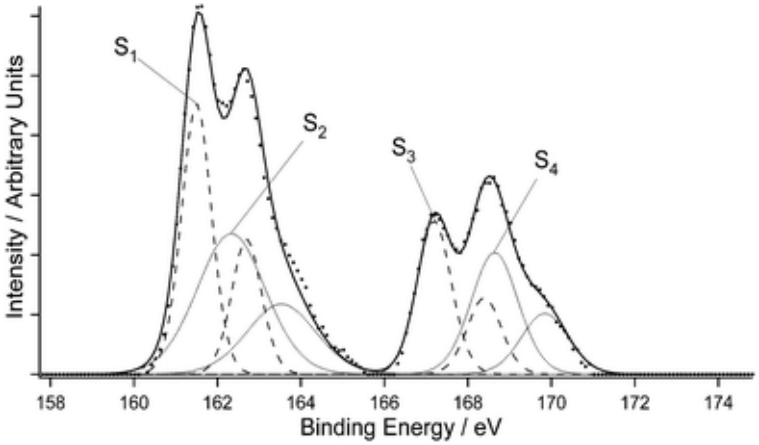

Figure 2.18: An example of the fitting of 4 different chemical states of the sulfur 2p doublet [27]

Most peaks are split into doublets. This is because of the spin-orbit coupling of a particular state, i.e. the interaction between the electron's orbital angular momentum, *l*, and its spin, *s*. *l* can take the value of any real integer, 0, 1, 2 etc. up to *n*-1, where *n* is the electron shell number, and corresponds to the sub-shells s, p, d, f etc. The electron's spin, *s*, is 1/2, and the total angular momentum of the electron is given by:

$$j = |l \pm s| \qquad (8)$$

where j is the total angular momentum, l is the orbital angular momentum, and s is the spin. It is clear, therefore, that for values of l greater than 0, e.g. the p, d, f etc. orbitals, the total angular momentum can take 2 values ($l \pm 1/2$). The resulting doublets always occur in specific ratios related to the degeneracy of the states, e.g. for a p state, with j values of 1/2 and 3/2 and degeneracy of $2j+1$, the peak areas will be in a ratio of 4:2, or 2:1. As the relative intensities are fixed in this manner, and so is the energy separation of the peaks, these parameters can be constrained in any fit to the peaks. For example, in the spectrum shown in figure 2.18, peaks within the same doublet were constrained to have the same FWHM, the doublet separation was fixed as 1.2 eV (the known separation for this species), and the ratio of peak areas within each doublet was set to be 2:1 (for p orbitals).

Depending on the X-ray source, spectra may also include what are known as 'satellites'. Satellites are smaller copies of the primary peaks at a constant separation from them; they are caused by the use of an X-ray source that is not monochromatic, a result of photoelectrons excited by unwanted characteristic lines from the X-ray anode. Usually they can be automatically removed by the analysis software, as their positions and intensities in comparison to the primary peaks are well known (typically the $K\alpha_3$ and $K\alpha_4$ characteristic lines of the anode)

2.4.3 Lab-Based XPS

The main components of a lab-based XPS kit are an X-ray source, sometimes with a monochromator, and an analyser. All of these components, along with the sample itself, must be housed within a chamber at ultra-high vacuum, to prevent reaction of the surface under the x-ray beam. The types of X-ray source used for XPS are fundamentally the same as those described in section 2.1, above. However, the anodes used are typically made of aluminium or magnesium, rather than copper, and many modern XPS systems utilise what are known as 'dual anodes', where one side of a conical anode is plated with aluminium and the other with magnesium. This type of system allows the sample to be analysed using X-rays of two different energies - 1253.6 eV from the magnesium $K\alpha_{1,2}$ lines and 1486.6 eV from the aluminium $K\alpha_{1,2}$ lines. The advantage of this is that it allows easier identification of Auger peaks in the spectra – these will always occur at the

same electron kinetic energy while all photoemission peaks will be shifted if the photon energy is changed.

Monochromators used in XPS are functionally identical to those of an XRD system, operating via diffraction of the X-ray beam from a diffraction element selected dependent on x-ray energy. XPS analysers are substantially more complicated than the detectors used in XRD as the energy of the electrons must be measured; most XPS systems use what is known as a concentric hemispherical analyser (CHA). As its name suggests, this consists of two conductive hemispheres concentric to one another, each at a set potential (figure 2.19). Electrons are allowed into the space between the hemispheres through a small slit, and deflected by the potential between them, such that only electrons of a specific energy, known as the 'pass energy', will traverse the the entire analyser to be detected and amplified by a channeltron or microchannel plate. These devices act as electron multipliers, similar to the photomultiplier tube described earlier. Electrons are focussed into the entrance of the analyser by an electrostatic lens, which also acts to retard the electrons as they arrive. In order to resolve the energy of incident electrons, an analyser can either operate with a fixed retardation potential and alter the potential of the hemispheres during a scan (known as 'Fixed Retardation Rate', or FRR mode) or the pass energy can remain fixed and the retardation potential can be altered (known as 'Constant Analyser Energy' or CAE mode)[5]. CAE mode (also known as Constant Pass Energy mode) is the more common of the two, one reason for which being that the the relative energy resolution of the analyser is defined as

$$\frac{\Delta E}{E_a} \qquad (9)$$

where E_a is the energy of the electron at the point it passes through the analyser, thus if this is fixed, the energy resolution of the analyser is fixed[6]. FRR mode is typically used for low kinetic energy regions, for example in Auger Spectroscopy.

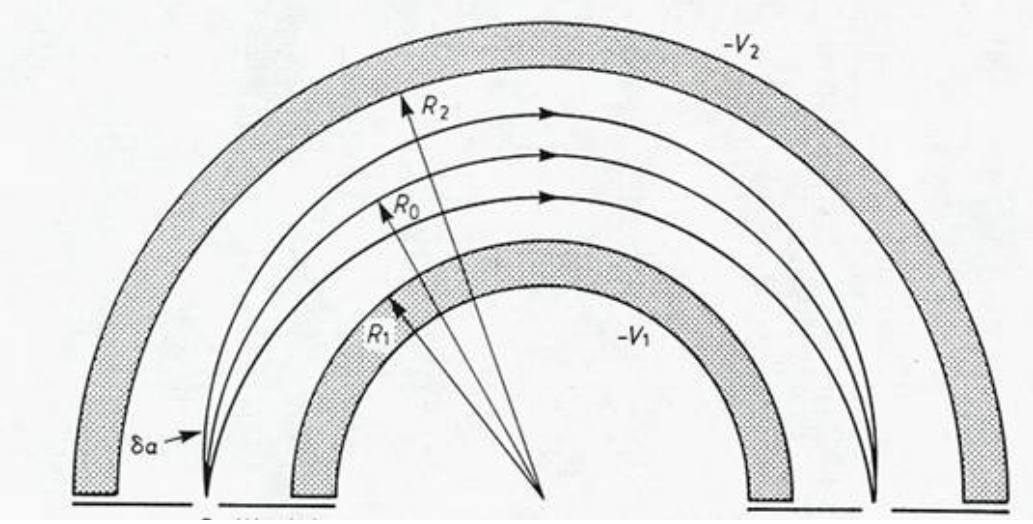

Figure 2.19: Cross section of a CHA, where R1 and R2 are the radii of the hemispheres, and V1 and V2 are the potentials applied to them. δa is the small variation in angle, known as the acceptance angle, at which electrons enter the analyser.

2.4.4 Synchrotron Based XPS

Synchrotrons are a type of particle accelerator which can be used to accelerate protons or electrons to extremely high velocities, allowing x-ray radiation to be produced when the electrons are passed through an oscillating magnetic field. The use of electron synchrotrons holds many advantages over using conventional XPS systems, such as the much greater X-ray intensities, and the ability to select the incident X-ray energy from a broad range *via* the use of a monochromator. Obviously, however, not every lab can contain a synchrotron, and their use is competitively allocated.

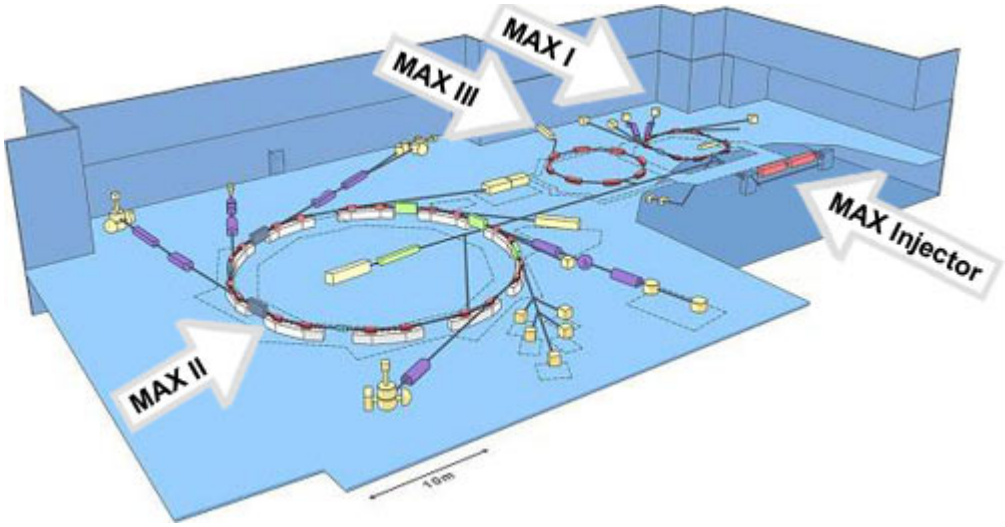

Figure 2.20: Schematic diagram of MAX-lab Synchrotron, showing the Linac (MAX injector) and the three main storage rings[29] .

Synchrotrons typically consist of a large 'storage' ring in which electrons are held at velocities close to the speed of light by an applied electric field, while a magnetic field is used to alter the electron trajectory, keeping them circulating in the ring. Synchrotrons are typically fed by a linear accelerator, sometimes with several smaller synchrotrons in between the main storage ring and the initial linear accelerator (figure 2.20). The electrons in a synchrotron travel around the ring in bunches, such that energy lost due to their circular acceleration can be replaced *via* the use of radio-frequency cavities operating at the appropriate frequency to accelerate electron bunches through an electromagnetic field when they pass through. Electrons lost from the beam must also periodically be replaced by re-injection.

Experiments can be performed at synchrotrons at equipment stations located on parts of the accelerator known as 'beamlines'. Often each beamline is dedicated to a specific type of experiment, with a set range of wavelengths of radiation that it can produce. The production of radiation at a beamline occurs via the use of arrays of magnets to produce a magnetic field with oscillating direction over a portion of the beamline. These come in two types commonly known as wigglers and undulators; wigglers produce a broader spectrum of radiation than undulators, but both operate on similar principles. By passing the electron beam through an undulator or wiggler, it experiences an oscillating magnetic field, causing it to oscillate transverse to its direction of motion as it passes (21). This

results in the production of the eponymous 'synchrotron' radiation due to the acceleration of the electron, at a wavelength determined by the strength and spatial frequency of the magnets. The beam of radiation produced is highly collimated due to the relativistic speed of the electron and extremely intense due to the amount of energy converted from the electron kinetic energy into the radiation. This beam can then be passed through a monochromator, and due to the intensity of the radiation over a large distribution of energies the wavelength to be used can be chosen from a broad range.

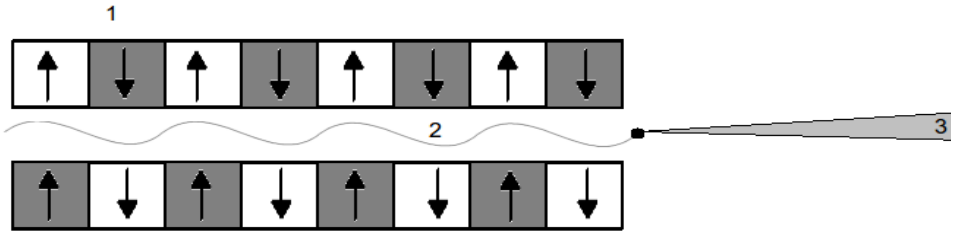

Figure 2.21: Basic diagram of an undulator, showing 1. Magnets, 2. Electron Path and 3. Produced beam of synchrotron radiation (emitted at every point on the electron's path through the undulator.

2.5 X-ray photoelectron spectroscopy literature review

2.5.1 XPS of bulk lead sulfide

The XPS of bulk lead sulfide has been heavily investigated, in part due to the importance of metal sulfide surface chemistry for ore recovery via flotation processes[7]. However the exact pathways of oxidation remain uncertain, with multiple explanations existing within the literature[8]. The most obvious oxidation products of lead sulfide are of course lead sulfite and lead sulfate, however other potential species present during the process can include lead carbonates[7–9], lead hydroxides[9,10], lead thiosulfate[10,11], hydrated lead oxides[12], neutral lead and neutral sulfur[8].

A mechanism for the oxidation of lead sulfide in an aqueous environment proposed by Hsieh and Hwang[13] and supported by Fornasiero *et al.*[10] is that the initial oxidation step of lead sulfide is protonation of the surface, with the following steps being either dissolution of lead sulfide (in the absence of oxygen) releasing lead (II) and sulfide ions into the bulk phase, or the adsorption of oxygen onto the protonated surface followed by the oxidation of sulfide into sulfate.

Studies of natural crystals of lead sulfide cleaved in air were performed by Buckley and Woods[12]. Studies of these crystals, held at temperatures below 150 K during spectroscopy, showed elemental sulfur formed as an oxidation product present on the surface after oxidation via exposure to hydrogen peroxide. This elemental sulfur was observed to be almost completely removed from the sample at ambient temperatures in vacuum, and was absent entirely after 15 hours. Signals due to oxidation observed after 15 minutes air exposure included a lead 4f doublet at ~1 eV higher binding energy than lead sulfide, which was attributed to lead hydroxide. After 1 day of exposure, the presence of lead carbonate was also confirmed *via* analysis of the carbon 1s peak. A small amount of sulfate formation was seen after 4 days' of exposure to air. Figure 2.22 shows XPS of the lead 4f and sulfur 2p peaks observed by Buckley and Woods.

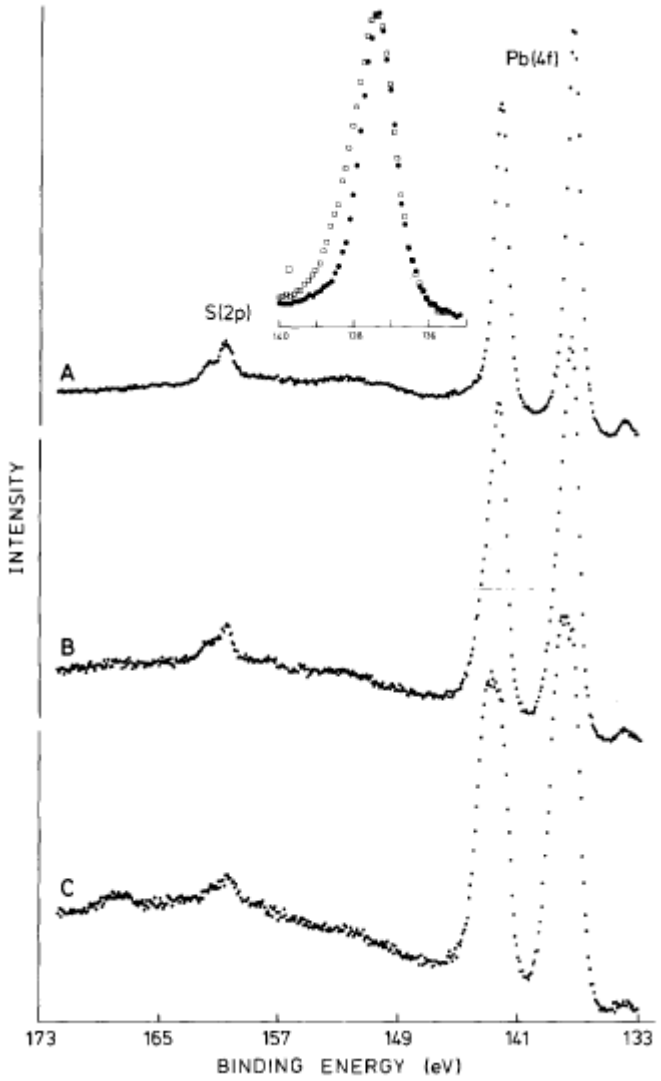

Figure 2.22: XPS of the lead 4f and sulfur 2p peaks of a cleaved lead sulfide surface after exposure to air for A: < 1 minute; B: 1 day; C: 9 days. Inset shows detail of lead $4f_{7/2}$ peak after exposure to air for less than one minute (circular points) and one hour (square points). Image from Buckley and Woods[12]

The presence of lead thiosulfate as a predominant oxidation product has also been reported, and oxidation routes involving the formation of lead oxide and neutral sulfur as the intial oxidation step have also been proposed, as described in Manocha and Park[11] and references therein. Regardless of the proposed oxidation route, rapid oxidation of the lead peak is reported[1112]. Sulfoxy groups, lead sulfate in particular, are reported as the final oxidation product in non-acidic conditions by the majority of workers[9,11,12,14].

A major point of contention within the literature is whether or not the oxidation of lead sulfide progresses in a congruent (lead and sulfur in equal proportion) or incongruent fashion, with evidence for both having been reported, on occasion by the same research groups[12,15,16].

The resistance of lead sulfide to oxidation in general has been commented upon in the literature[9], with passivation of the surface due to initial oxidation products or adsorption of organic molecules being a potential cause[12,17] The adsorption of various organic molecules used in flotation processes on metal ions including Pb^{2+} has been investigated by Porento *et al.*[17,18]. Their work found particularly strong interaction between ethyl thiocarbamates and metal ions, including Pb^{2+}.

Yashina *et al.* present a detailed study of the sulfur species present during oxidation of lead sulfide, along with supporting computational data[14]. They report the presence of multiple intermediate species present throughout the ageing process, with chemical shifts of 1-3 eV relative to that of the clean surface sulfur species. These intermediate species are attributed to the attachment of 1-3 oxygen atoms to an individual sulfur atom, as opposed to the formation of polysulfide particles as suggested in the work by Buckley and Woods on oxidation due to exposure of air-saturated acetic acid[12].

2.5.2 XPS of lead sulfide nanoparticles

Comparatively little in-depth XPS has been reported on lead sulfide nanoparticles, and even less about their ageing and oxidation. X-ray photoelectron spectroscopy has been reported for lead sulfide nanoparticles in polymer composites[19,20] and exhibited no visible oxidation, most likely due to the synthesis route minimising exposure to air. XPS of nanoparticles synthesised *via* a sonochemical method in an oil-in-water emulsion has been reported by Hui Wang *et al.*[21]. This work reported a concentration of lead on the surface of the particles, which the authors suggest is due to the absorption of lead ions onto the surface of their particles. A moderate amount of oxidation can be observed in the sulfur 2p spectra presented by the authors (figure 2.23).

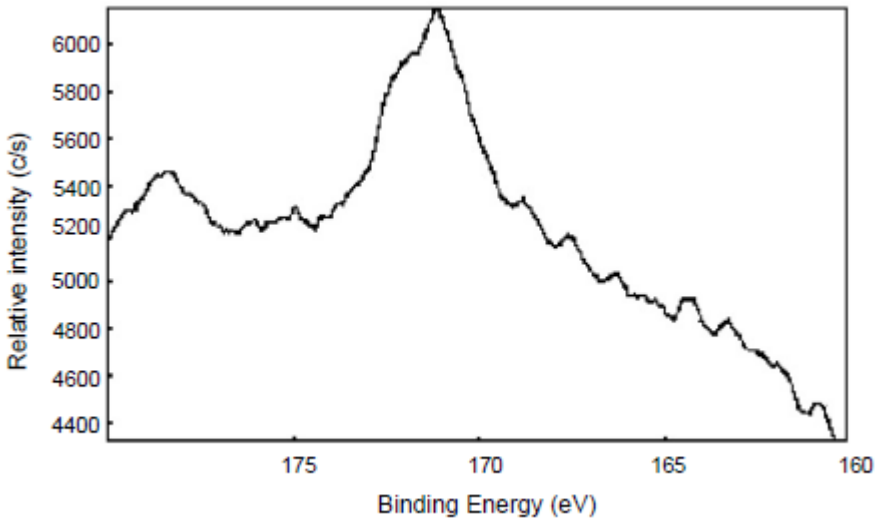

Figure 2.23: Sulfur 2p XPS spectra from work reported by Hui Wang et al.[21]. The smaller peak at ~178 eV binding energy is likely due to oxidised species.

The most detailed study of lead-sulfide nanoparticle oxidation is presented by S. Hardman *et al.*[22] on particles synthesised using standard colloidal methods. Relatively large amounts of both lead and sulfur oxidised species were reported after a few hours exposure to air. The proportion of oxidised products probed by XPS was found to decrease with particle size, indicating that surface-area to volume ratio is an important factor to nanoparticle oxidation, as might be expected. Depth profiling XPS showed that the oxidised products were concentrated at the surface of the nanoparticles, and thickness calculations resulted in an estimated 0.5 nm layer of oxidised sulfur species present at the surface of the particle exposed to air for a few hours. An example of the level of oxidation observed is given in figure 2.24. Peaks labelled Pb1, Pb2 and Pb3 were assigned to neutral lead, lead in lead sulfide, and lead in lead oxide respectively. Peaks labelled S1, S2, S3 and S4 were assigned to sulfur in lead sulfide, neutral sulfur, lead sulfite and lead sulfate, respectively.

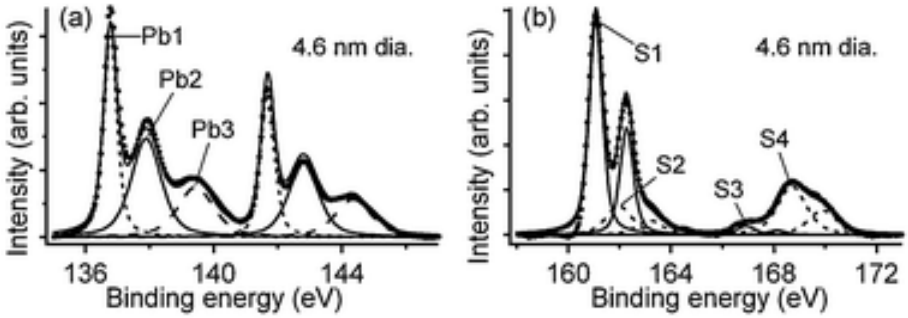

Figure 2.24: XPS spectra of the lead 4f (left) and S 2p (right) regions of 4.6 nm diameter butylamine-capped nanoparticles, sampled at a photon energy of 250 eV.[22]

References

(1) The University of Sheffield Materials Science and Engineering Dept. http://www.shef.ac.uk/materials/about/facilities/x-ray-diffraction/analysis.html (accessed Mar 16, 2011).

(2) Jenkins, R.; Snyder, R. L. .

(3) Patterson, A. *Physical Review* **1939**, *56*, 978-982.

(4) Postek, M. T. *Scanning Electron Microscopy - A Student's Handbook*; 1980.

(5) *Practical Surface Analysis 2nd Edition Vol. 1: Auger and X-Ray Photoelectron Spectroscopy*; Briggs, D.; Seah, M. P., Eds.; Wiley.

(6) Vickerman, J. C., Ed.; Wiley.

(7) Nowak, P.; Laajalehto, K. *Fizykochemiczne Problemy Mineralurgii* **2007**, *Vol. 41*, 107-116.

(8) Hampton, M. A.; Plackowski, C.; Nguyen, A. V. *Langmuir : the ACS journal of surfaces and colloids* **2011**, *27*, 4190-201.

(9) Nowak, P.; Laajalehto, K. *Applied Surface Science* **2000**, *157*, 101-111.

(10) Fornasiero, D.; Li, F.; Ralston, J.; Smart, R. S. C. *Journal of Colloid and Interface Science* **1994**, *164*, 333-344.

(11) Park, R. L. *Applications Of Surface Science* **1977**, *1*.

(12) Buckley, A. N.; Woods, R. *Applications of Surface Science* **1984**, *17*, 401-414.

(13) Hsieh, Y. .; Huang, C. . *Journal of Colloid and Interface Science* **1989**, *131*, 537-549.

(14) Yashina, L. V.; Zyubin, A. S.; Püttner, R.; Zyubina, T. S.; Neudachina, V. S.; Stojanov, P.; Riley, J.; Dedyulin, S. N.; Brzhezinskaya, M. M.; Shtanov, V. I. *Surface Science* **2011**, *605*, 473-482.

(15) Kartio, I.; Wittstock, G.; Laajalehto, K.; Hirsch, D.; Simola, J.; Laiho, T.; Szargan, R.; Suoninen, E. *International Journal of Mineral Processing* **1997**, *51*, 293-301.

(16) Laajalehto, K.; Kartio, I.; Suoninen, E. *International Journal of Mineral Processing* **1997**, *51*, 163-170.

(17) Porento, M.; Hirva, P. *Theoretical Chemistry Accounts: Theory, Computation, and Modeling (Theoretica Chimica Acta)* **2002**, *107*, 200-205.

(18) Porento, M.; Hirva, P. *Surface Science* **2003**, *539*, 137-144.

(19) Asunskis, D. J.; Hanley, L. *Surface Science* **2007**, *601*, 4648-4656.

(20) Asunskis, D. J.; Bolotin, I. L.; Wroble, A. T.; Zachary, A. M.; Hanley, L. *Macromolecular Symposia* **2008**, *268*, 33-37.

(21) Wang, H.; Zhang, J.-R.; Zhu, J.-J. *Journal of Crystal Growth* **2002**, *246*, 161-168.

(22) Hardman, S. J. O.; Graham, D. M.; Stubbs, S. K.; Spencer, B. F.; Seddon, E. A.; Fung, H.-T.; Gardonio, S.; Sirotti, F.; Silly, M. G.; Akhtar, J.; O'Brien, P.; Binks, D. J.; Flavell, W. R. *PCCP* **2011**, *13*, 20275-83.

(23) Reimer, L.; Kohl, H. *Transmission electron microscopy: physics of image formation*; Springer, 2008; p. 587.

(24) University of Michigan Electron Microbeam Analysis Laboratory http://emalwww.engin.umich.edu/courses/semlectures/focus.html (accessed Mar 19, 2011).

(25) Goldstein, J. *Scanning electron microscopy and x-ray microanalysis, Volume 1*; Springer, 2003; p. 689.

(26) Center for Microscopy and Imaging, Smith College http://131.229.114.77/microscopy/home.html (accessed Mar 20, 2011).

(27) Akhtar, J.; Azad Malik, M.; O'Brien, P.; Wijayantha, K. G. U.; Dharmadasa, R.; Hardman, S. J. O.; Graham, D. M.; Spencer, B. F.; Stubbs, S. K.; Flavell, W. R.; Binks, D. J.; Sirotti, F.; El Kazzi, M.; Silly, M. *Journal of Materials Chemistry* **2010**, *20*, 2336.

(28) Match! - Phase Identification from Powder Diffraction http://www.crystalimpact.com/match/Default.htm (accessed Mar 16, 2011).

(29) MAX-lab, Sweden www.maxlab.lu.se (accessed Mar 17, 2011).

(30) Watt, I. M. *The Principles and Practice of Electron Microscopy*; Cambridge University Press, 1997; p. 484.

(31) *Lead Sulphide Powder Diffraction File - PDF#00-003-0665 (accessed 21/03/12)*.

Chapter 3: Nanoparticle Synthesis

There are many routes for synthesis of nanoparticles, including thermal treatment of compounds doped into glass[1], the more common colloidal methods[2–4] and several methods of forming nanoparticles in the vapour phase[5]. Currently, colloidal synthesis methods dominate interest in the field of photovoltaics because they offer cheap, simple synthesis of nanoparticles of potentially very narrow size dispersions, and an almost limitless scalability of production. It is theoretically no more complex to produce a litre than a few millilitres of a nanoparticle dispersion in a liquid, as the reaction is independent of volume. Practical concerns such as the maintenance of the correct temperature across the entire solution may act as limiting factors in upscaling of production volumes, but otherwise colloidal synthesis lends itself well to bulk production.

The method of colloidal synthesis involves the decomposition of precursors in an organic solvent with a high boiling point, at a temperature on the order of 200-300 ^{o}C. Reaction time or precursor concentration is used to control the resulting nanoparticle size. Upon reaching the desired size however, the reaction is not easy to halt – even once cooled, a process known as 'Ostwald ripening' occurs. Larger nanoparticles are typically more stable than smaller ones as they have a higher lattice energy. As such they tend to clump together or grow, while smaller nanoparticles are more likely to dissolve[6]. In order to counter this, ligands are added which bind to the surface of the nanoparticles, halting their growth. These ligands are typically insulating organic molecules[7,8]. The presence of these ligands poses one of the main disadvantages present in most modern studies of nanoparticles for use in photovoltaic devices; the insulating nature of these ligands acts to inhibit the production of useful current from a given exciton. Another disadvantage of this method is that the resulting nanoparticles are dispersed in a liquid. While this state may prove useful when taking certain measurements of their properties, such as absorption and photoluminescence spectra, it is not conducive to use in a solar cell.

There are multiple issues with attempting to produce a solid device from a dispersion of nanoparticles. Primarily, the dispersion has to be deposited, adding an extra process to production of a device. Deposition of particles *via* drying of the solvent is likely to result in a non-uniform film, thus spin-coating is required. Dependent on the solvent used, deposition may also take a significant amount of time.

3.1 Crystal growth

There are multiple processes of nucleation and growth that may occur in the synthesis of nanoparticles from precursors in solution. In order to precipitate the growth of particles, there must exist a supersaturated solution, achieved typically either by saturating a solution at high temperature and cooling, or by the formation of a supersaturated solution from the reaction of multiple precursors[9]. The two primary mechanisms of nucleation are homogeneous nucleation and hetergeneous nucleation. Homogeneous nucleation occurs when there is no solid surface upon which nucleation may occur – particles are formed by the combination of dissolved molecules. The driving force of this process of nucleation is thermodynamic – the supersaturated solution is not energetically stable, and thus the formation of particles is favoured. Heterogeneous nucleation is the process whereby a new phase is nucleated upon an existing surface. Frequently, the free energy required for hetereogeneous nucleation is lower than that of homogeneous nucleation, so if homogeneous nucleation is desired it is prudent to ensure the absence of foreign particles from the supersaturated solution[10].

Once nucleation has occurred, particles typically grow *via* molecular addition, where soluble species are deposited on the surface of existing particles. Should the solution reach a point where it is no longer supersaturated due to depletion of the reactants, Ostwald ripening will occur, as the smaller particles may begin to re-dissolve in the solvent. Particles may also grow by aggregation with other particles, which is referred to as 'secondary growth'[9]. The rate of growth due to aggregation is typically much larger than the rate of growth due to molecular addition.

3.2 Self assembly of nanoparticles

The term 'self assembly' refers to any process whereby an ordered arrangement of particles may be achieved spontaneously, typically due to the presence of a combination of forces such as fluid tension, electrostatic repulsion/attraction, and chemical interactions[10]. Particles will self assemble into the structure with the lowest free energy reaching a state with a minimum of repulsive forces and a maximum of attractive force[11]. Self assembly of nanoparticles is important and useful phenomenon for the purpose of creating devices, as many potential applications (such as gas sensors, computer chips, etc.) either require or benefit from a uniform, large scale structure.

3.3 Liquid-liquid interfacial synthesis

One potential synthesis route which neatly sidesteps the issues inherent in colloidal synthesis is the use of liquid-liquid interfaces [12–14]. This method is similar to standard colloidal methods, in that it involves reaction of precursors in solution, albeit at lower temperatures than those used in colloidal synthesis (typically 50-70 ^{o}C). The difference lies in the fact that the two precursors are dissolved in a pair of separate immiscible liquids, and that the reaction takes place at the liquid-liquid interface between them (Figure 3.1).

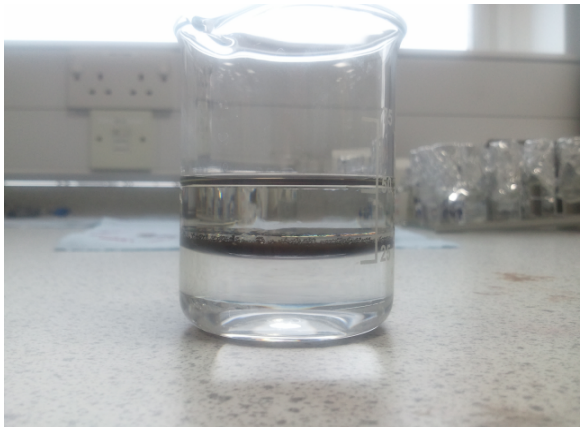

Figure 3.1: Lead sulfide thin film formed at the water-toluene interface.

The precursors are dissolved at the desired concentrations, typically with an ionic precursor in water and an organometallic precursor in toluene or another similar organic solvent, and then carefully layered upon each other so as to maintain an even interface. This combination of solvent and precursor types is chosen such that solvents are immiscible with one another, and neither precursor is soluble in the solvent it is not initially dissolved in. Depending on the precursors used and their concentrations, as well as the desired product, the layers may be heated or left at room temperature for a period ranging from a few minutes to several hours until a thin film of particles forms at the interface. These thin films can then be easily transferred onto a substrate of choice (e.g. glass slides) by either removing the top solvent layer and manually depositing the film, or by removal of the top layer and draining of the bottom layer in glassware designed for this purpose. The product is affected by precursor concentration, time and temperature, but can be most strongly controlled *via* the alteration of the heights of the precursor solutions, especially whichever rests on top, due to the effects of pressure at the interface[12]. This increases the growth rate of the films, affecting the morphology of the final product. Products formed by this method can range from nanoparticles on the order

of a few (≤10) nanometres in size, through nanofibres/rods to more unusual morphologies such as the pyramidal PbS crystals with base lengths of ~500 nm produced by D. Fan *et al.* [12]. The product of this method has clear advantages over traditionally produced colloidal nanoparticles: the growth ceases upon deposition and removal of the films from the interface with no stabilising ligand required; the product is obtained in one step as an evenly distributed solid film, with potential for mesostructure control due to self-assembly at the interface given appropriate conditions.

This method of synthesis works due to the processes which occur at the interface between the two liquids. While from a macroscopic point of view the interface between two immiscible liquids appears abrupt and discontinuous, it in fact forms a gradient of both solvents across the interface. In the case of the reaction described above, synthesising metal sulfides at the interface between water and toluene, the concentration of metal and sulfide ions across the interface varies as in the schematic diagram shown in figure 3.2.

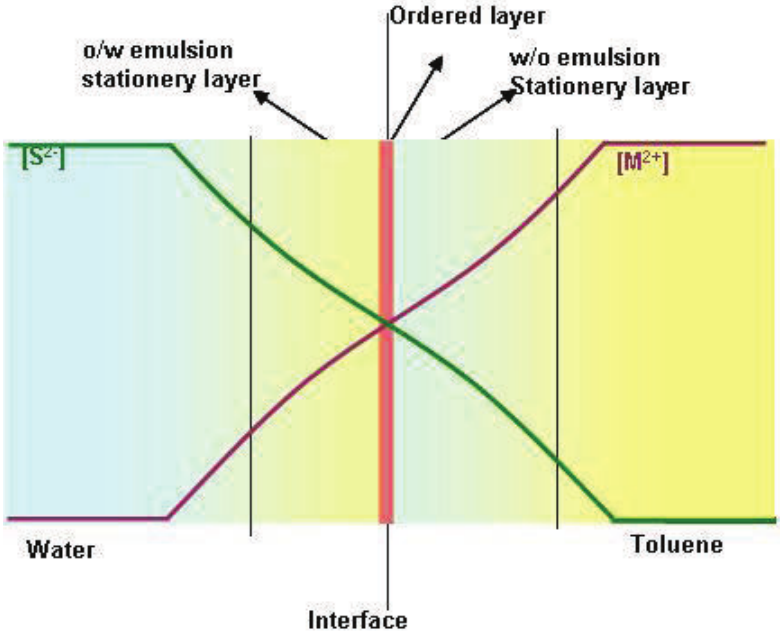

Figure 3.2: Diagram showing the variation in concentrations of M^{2+} and S^{2-} ions (purple and green lines, respectively) across the water-oil interface[10].

This gradient in concentration of the reactants allows the reaction to proceed directly at the interface. Particles of the product formed in this region will then adhere to the

interface, remaining buoyant due to the surface tension of the meniscus formed around them. Such particles will remain adherent to the interface unless their size becomes large enough that the force of gravity is enough to overcome that of the surface tension, as the energy required for desorption of particles from the interface is orders of magnitude greater than the thermal energy[10]. Due to the differing polarities of the two solvents, a dipole is created across the particle[12] as shown in figure 3.3.

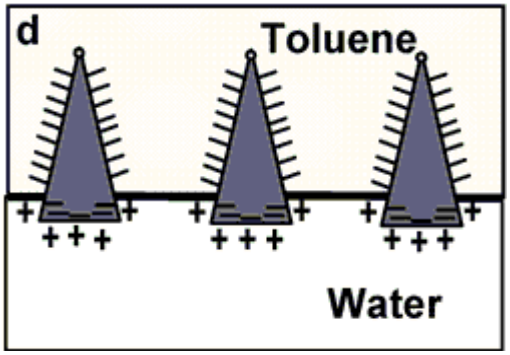

Figure 3.3: Schematic diagram of pyramidal particles forming a dipole at the interface between toluene and water, from D Fan et al.[12]

This thus prevents the particle from being able to rotate around any axis parallel to the interface. The particle is free to move within the interface however, and its motion is governed by complex interactions involving both capillary forces between particles which are close to each other (caused by the distortion of the interface due to the presence of the particle), and weaker, longer-range Coulomb repulsion due to the charge on the particles[10,12]. The combination of Brownian motion at the interface and the strong attractive capillary forces at close range typically result in the particles forming aggregates and 'clumping' together. Films synthesised using this technique have been shown to be self-assembled in a particular morphology and orientation[12], and to have properties controllable by alteration of various reaction conditions, including the height of the solvent layer, precursor concentration, temperature, and others. The reason for the solvent height dependence is unclear, but has been proposed to be due to its effect on the thickness of the emulsive layers at the interface[12].

It is this method of synthesis that has been explored in detail within this thesis; primary aims were to investigate and refine the synthetic technique towards producing thin films of nanoparticles useful for application in solar photovoltaics, and to characterise the products of this technique using an array of surface analysis and spectroscopic techniques including X-ray diffraction, X-ray photoelectron spectroscopy, and various electron

microscopies. A range of lead-containing precursors were used to synthesise PbS films, and are described in section 3.4. The sulfide precursor used in synthesis of these films was Na_2S. Initially, pure Na_2S was used, however due to the hygroscopic nature of Na_2S this caused inaccuracies in the concentration, and as such later syntheses used $Na_2S.9H_2O$.

3.4 Precursor Synthesis

Several precursor types that had been previously demonstrated to produce films of other metal chalcogenides were used, including a number of lead thiocarbamates, lead thiobiuret, and lead ketoacidoximate[15]. Synthesis *via* phase transfer of lead ions into toluene was also attempted, and this method is explained in section 3.4.4.

3.4.1 Lead Diethyldithiocarbamate

The lead diethyldithiocarbamate (DETC) was synthesised by first dissolving ~0.4 g of NaOH in 40 ml of methanol, and then carefully adding ~1.1 ml of diethylamine. Next, ~0.6 ml of carbon disulfide was added to the solution dropwise. Immediately after this step a solution of ~1g lead(II) acetate in 40ml of methanol was added and the resulting mixture was stirred vigorously to avoid polymerisation. A pale brown precipitate formed and was collected using filter paper. The precipitate was then dried to a pale yellow solid, and was confirmed to be lead diethyldithiocarbamate by elemental analysis. Elemental analysis found(%): C = 24.5;N = 4.1;H = 5.6 (expected C = 23.8;N = 4.0;H = 5.6). The structure of this precursor is given in figure 3.4.

Figure 3.4: The chemical structure of lead diethyldithiocarbamate (Et. represents an ethyl group, -C_2H_5).

X-ray diffraction was carried out on a sample of the precursor in order to aid in the identification of non-PbS related peaks in the diffraction patterns of the PbS films

themselves. The diffraction pattern obtained for lead diethyldithiocarbamate is shown in figure 3.5. This pattern is similar to that seen in previous work, shown in figure 3.6[10]; some variations in intensity are observed, but this is likely due to discrepancies in the preparation of the sample plate prior to measurement.

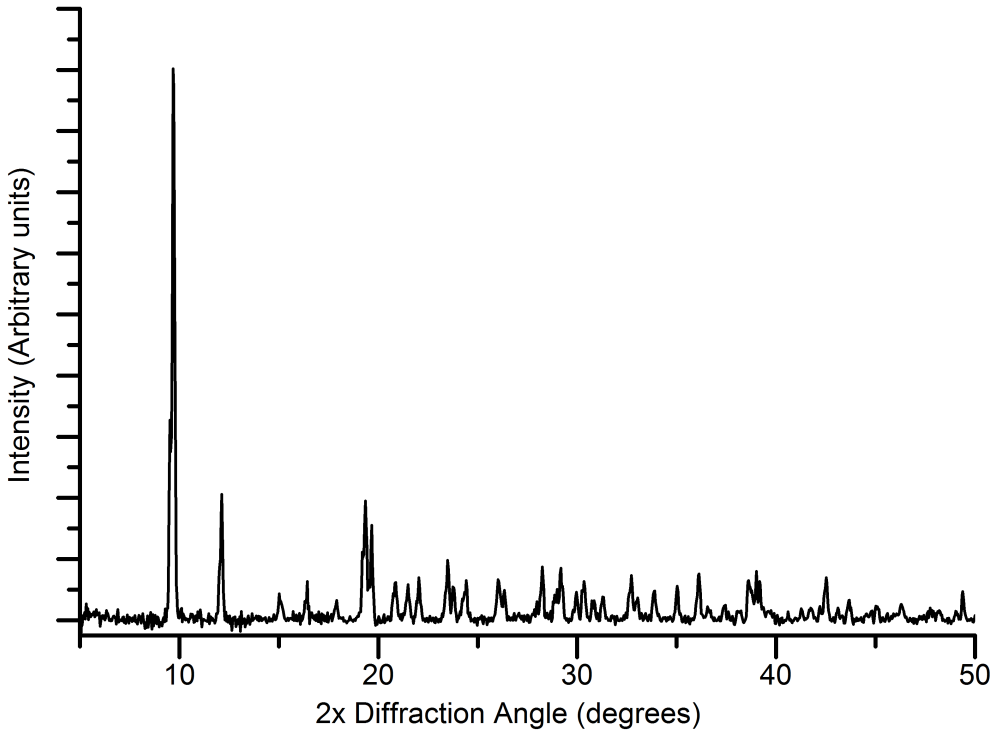

Figure 3.5: X-ray diffraction pattern of lead diethyldithiocarbamate.

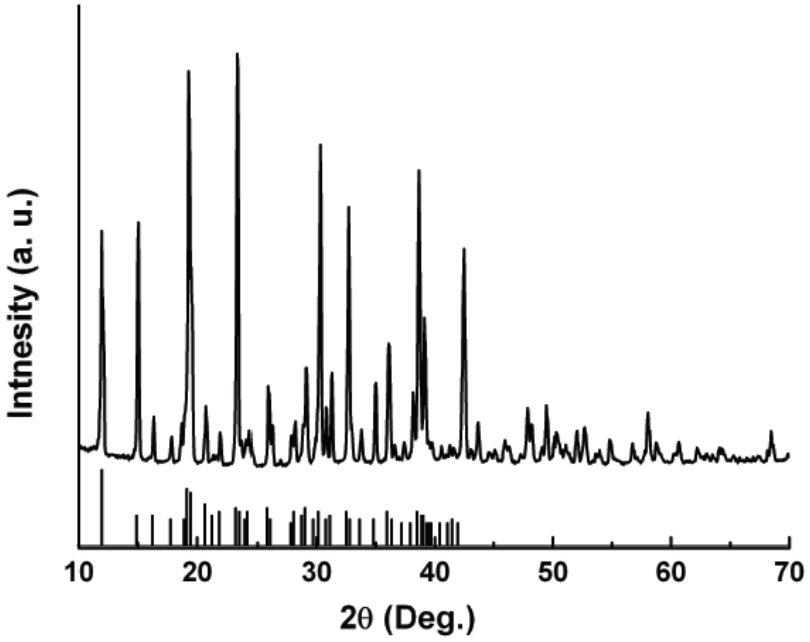

Figure 3.6: X-ray diffraction pattern of the lead DETC precursor as prepared by D. Fan[10], provided for comparison.

3.4.2 Lead dibutyl- and dipentyldithiocarbamate

Films have been successfully synthesised using dithiocarbamate precursors with larger alkyl groups – specifically lead dibutyldithiocarbamate (DBTC) and lead dipentyldithiocarbamate (DPTC). These precursor differ only slightly from lead DETC – having butyl or pentyl groups where the original has ethyl groups. The synthesis of these precursors was similar to the synthesis of diethyldithiocarbamate, but used dibutylamine or dipentylamine instead of diethylamine. Lead DPTC and some of the lead DBTC used to synthesise lead sulfide films were provided by Edward Lewis of the School of Chemistry, University of Manchester, UK. The structure of lead dibutyldithiocarbamate is given in figure 3.7. Elemental analysis of the lead dibutyldithiocarbamate found(%): C =34.8 ;N = 6.2;H = 4.5 (expected: C = 35.1;N = 5.9;H = 4.6). Elemental analysis of the lead dipentyldithiocarbamate found(%): C = 40.2;N = 7;H = 4.2(expected: C = 39.3;N = 6.6;H = 4.2).

Figure 3.7: The chemical structure of lead dibutyldithiocarbamate (Bu. represents a butyl group, C_4H_9)

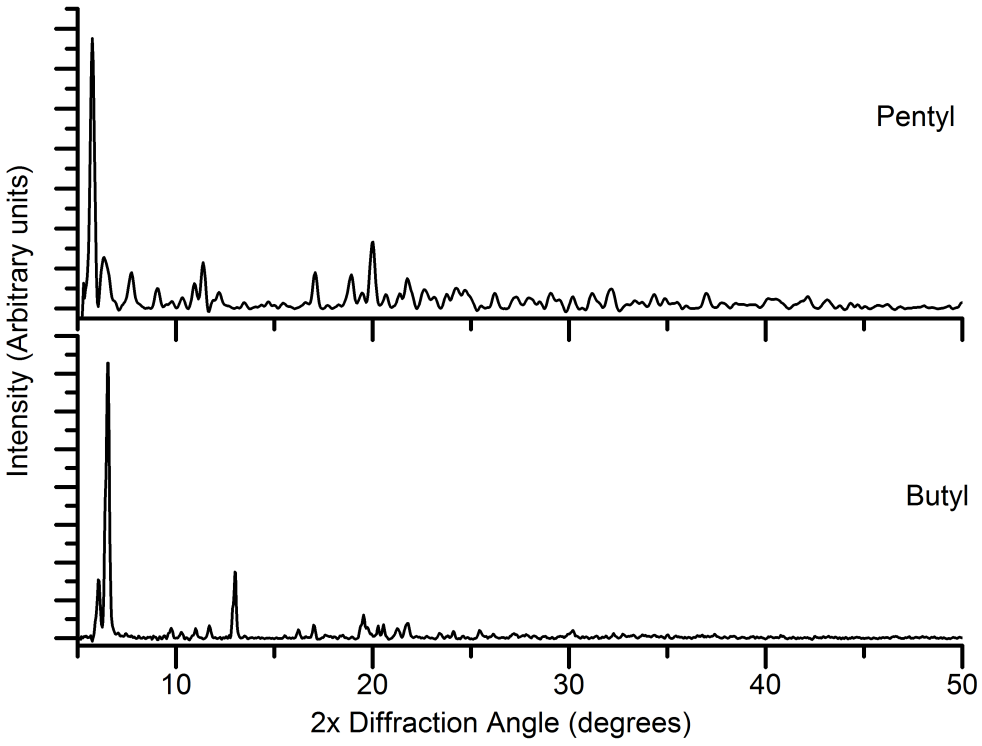

Figure 3.8: X-ray diffraction pattern of lead dibutyl and dipentyl dithiocarbamates.

X-ray diffraction of lead DBTC and DPTC gave the patterns shown in figure 3.8. X-ray diffraction of these precursors has not been reported previously, and so cannot be provided for comparison.

3.4.3 Lead thiobiuret

The synthesis of the thiobiuret precursor was carried out by heating ~1 g of diisopropylcarbamoyl chloride and ~0.5 g of sodium thiocyanate dissolved in 25 ml of acetonitrile under reflux for 1 hour. This mixture was then cooled and ~1.5 ml of diisopropylamine was added and stirred for 30 minutes. Finally, ~1 g of lead(II) acetate was added to the mixture and stirred for 30 minutes. The resulting pale-brown precipitate was collected and dried using filter paper.

Attempts to synthesise films of lead sulfide using lead thiobiuret were conducted using 30 ml layers of 2 mM solutions at both 50^{o} and 70^{o} C. Both of these attempts initially failed to produce PbS. The precursor displayed comparatively low solubility in toluene and settled at the interface. Synthesis using thiobiuret was reattempted with the addition

of 10ml of octanol to the toluene layer. This improved the solubility and resulted in a film of PbS.

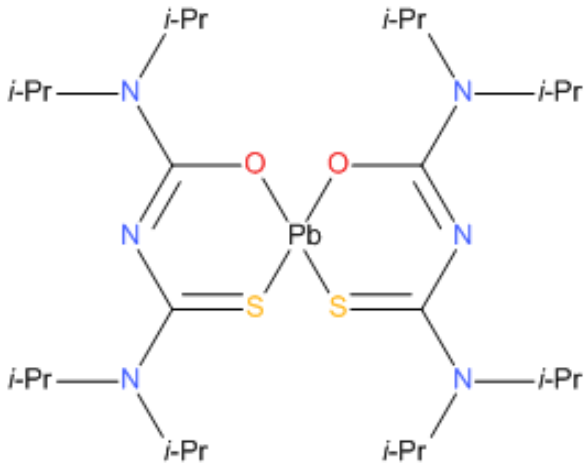

Figure 3.9: The chemical structure of the lead thiobiuret complex(ipr. represents an isopropyl group, -C_3H_7)

After successful syntheses had been achieved using this precursor, routine micro-analysis indicated different proportions of elements to the expected result for a pure sample with the structure shown in figure 3.9. XPS performed on samples synthesised using this precursor revealed the presence of sodium within the films. Further micro-analysis revealed the presence of sodium within the precursor, as sodium chloride was formed as a bi-product of the precursor synthesis from the sodium and chlorine present in the sodium thiocyanate and diisopropylcarbamoyl chloride respectively. Further synthesis, assisted by Emmanuel Ezenwa of the School of Chemistry, University of Manchester was conducted to attempt to obtain a purer form of the precursor. Synthesis under a nitrogen atmosphere, and recrystallisation of the product from tetrahydrofuran (THF) resulted in a purer version of the precursor as confirmed by elemental analysis, which found (%): C = 43.04; H = 7.90; N = 10.69 S=8.06 Pb = 26.49 (Expected C = 43.1; H =7.1; N =10.8; S = 8.2 Pb =26.6)

X-ray diffraction of this precursor gave the pattern shown in figure 3.10.X-ray diffraction of this precursor has not been reported previously, and as such cannot be shown for comparison.

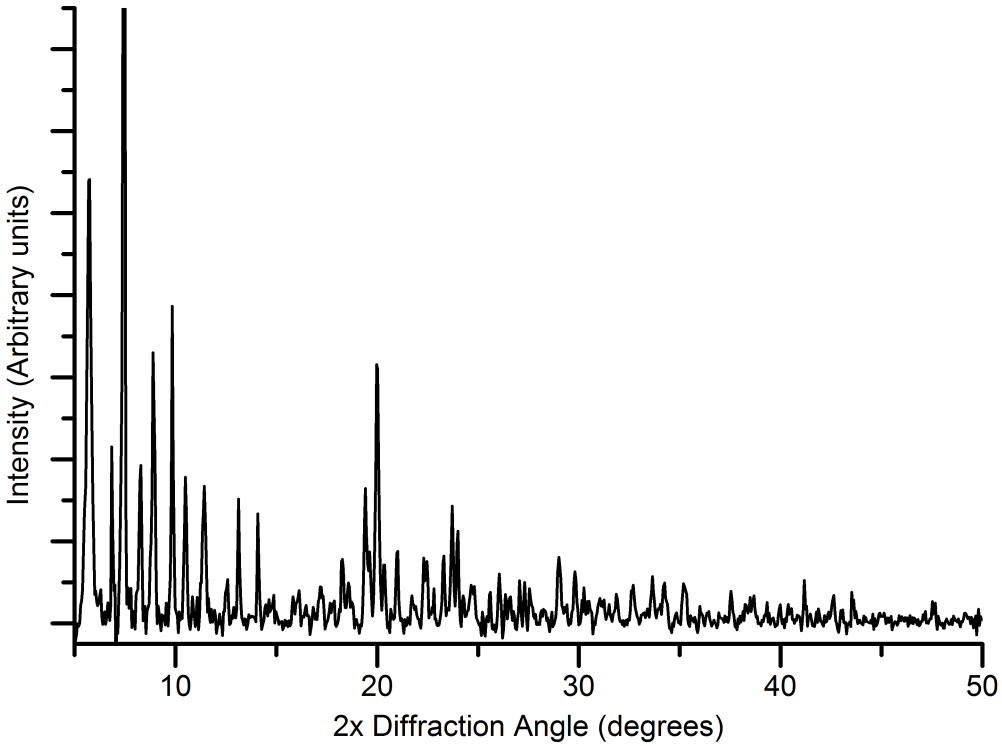

Figure 3.10: X-ray diffraction pattern of the lead thiobiuret.

3.4.4 Other syntheses

Attempts to synthesise PbS films were also made using lead ketoacidoximate, synthesised by Alex Lockett of the School of Chemistry, University of Manchester. Syntheses were conducted using a 2 mM concentration of precursors at a solvent height of 19±1 mm at both 50° and 70° Celsius for two hours. These syntheses suffered from the same lack of precursor solubility as seen in the initial syntheses using lead thiobiuret, and failed to produce PbS films as the precursor settled at the interface.

Attempts were made to synthesise films *via* phase transfer of lead ions from an aqueous solution to toluene. This method, described by Ying *et al.*[16] involves the transfer of the lead ions into the toluene layer by adding 1 ml of dodecylamine to an aqueous solution of a lead salt (lead(II) acetate was used in this case). Toluene was then layered on top of the mixture, which was stirred for one minute. The toluene was then pipetted off and layered

onto the aqueous Na_2S solution. Unfortunately, this method did not produce any films, and the addition of potassium iodide (which should produce lead iodide as a yellow precipitate on reaction with lead ions) to toluene prepared in this manner revealed that the transfer of lead ions into the toluene had failed.

During attempts to synthesise a pure lead thiobiuret precursor, the synthesis of other similar compounds was attempted. Attempts to synthesise a lead selenobiuret by replacing the use of sodium thiocyanate with potassium selenocyanate were unsuccessful. Synthesis of an iron thiobiuret precursor as previously reported in [17] was also performed, and was used in the attempted synthesis of iron sulfide nanoparticle thin films *via* the use of the liquid-liquid interface method. Attempted synthesis of FeS films using this technique resulted in a yellow precipitate at the interface, however this precipitate gave no XRD pattern, and thus could not be confirmed to be FeS.

References

1. P. Naves, T. Gonzaga, a Monte, and N. Dantas, *Journal of Non-Crystalline Solids*, 2006, **352**, 3633-3635.

2. J. Akhtar, M. Azad Malik, P. O'Brien, K. G. U. Wijayantha, R. Dharmadasa, S. J. O. Hardman, D. M. Graham, B. F. Spencer, S. K. Stubbs, W. R. Flavell, D. J. Binks, F. Sirotti, M. El Kazzi, and M. Silly, *Journal of Materials Chemistry*, 2010, **20**, 2336.

3. A. a. Patel, F. Wu, J. Z. Zhang, C. L. Torres-Martinez, R. K. Mehra, Y. Yang, and S. H. Risbud, *The Journal of Physical Chemistry B*, 2000, **104**, 11598-11605.

4. J. E. Murphy, M. C. Beard, A. G. Norman, S. P. Ahrenkiel, J. C. Johnson, P. Yu, O. I. Mićić, R. J. Ellingson, and A. J. Nozik, *Journal of the American Chemical Society*, 2006, **128**, 3241.

5. M. Swihart, *Current Opinion in Colloid & Interface Science*, 2003, **8**, 127-133.

6. D. V. Talapin, A. L. Rogach, M. Haase, and H. Weller, *The Journal of Physical Chemistry B*, 2001, **105**, 12278-12285.

7. P. Guyot-Sionnest, B. Wehrenberg, and D. Yu, *The Journal of chemical physics*, 2005, **123**, 074709.

8. a Lobo, T. Möller, M. Nagel, H. Borchert, S. G. Hickey, and H. Weller, *The journal of physical chemistry. B*, 2005, **109**, 17422-8.

9. C. Burda, X. Chen, R. Narayanan, and M. A. El-Sayed, *Chemical reviews*, 2005, **105**, 1025-102.

10. D. Fan, *Thesis submitted to the University of Manchester*, 2008.

11. R. A. F., Tandra Goshal, Justin D. Holmes and Michael A. Morris Colm T. O'Mahony, *Thermodynamics - Systems in Equilibrium and Non-Equilibrium*, InTech, 2011.

12. D. Fan, P. J. Thomas, and P. O'Brien, *Journal of the American Chemical Society*, 2008, **130**, 10892-4.

13. C. N. R. Rao, G. U. Kulkarni, V. V. Agrawal, U. K. Gautam, M. Ghosh, and U. Tumkurkar, *Journal of colloid and interface science*, 2005, **289**, 305-18.

14. D. Fan, P. J. Thomas, and P. O'Brien, *Journal of Materials Chemistry*, 2007, **17**, 1381.

15. Y. S. Wang, P. J. Thomas, and P. O'Brien, *The journal of physical chemistry. B*, 2006, **110**, 4099-104.

16. J. Yang, E. H. Sargent, S. O. Kelley, and J. Y. Ying, *Nature materials*, 2009, **8**, 683-9.

17. K. Ramasamy, M. A. Malik, M. Helliwell, F. Tuna, and P. O'Brien, *Inorganic chemistry*, 2010, **49**, 8495-503.

Chapter 4: Initial synthesis and variation in solvent height using lead diethyldithiocarbamate precursor

4.1 Introduction

Initial attempts to synthesise PbS nanoparticles were made using lead diethyldithiocarbamate (DETC) precursor and sodium sulfide concentrations of 1.67 mM and a solvent height of 19±1 mm based on prior results reported by D. Fan[1]. After several films synthesised using these conditions displayed inconsistent results, the sodium sulfide (Na_2S) was replaced with sodium sulfide nonahydrate ($Na_2S.9H_2O$). This is because the hygroscopic nature of the sodium sulfide leads to measured weights being incorrect due to absorbed water. Use of sodium sulfide nonahydrate is preferable as the presence of water within the precursor can be accounted for in the measured weight, resulting in a higher accuracy in the concentration. Samples were synthesised at several solvent heights of 19±1, 22±1 and 25±1 mm using the sodium sulfide nonahydrate precursor, with both lead and sulfur precursors at a concentration of 1.67 mM. Initial samples (synthesised using sodium sulfide) were characterised using XRD, SEM, and XPS. Samples at varying solvent heights (synthesised using sodium sulfide nonahydrate) were characterised using XRD and XPS. The results of this characterisation are presented below.

4.2 Initial syntheses

4.2.1 XRD

Syntheses using sodium sulfide produced films of lead sulfide with varied appearance and moprphology due to the inaccuracy presented by the hydroscopic nature of the precursor. XRD of a typical film is shown in figure 4.1.

Typically, these films showed a slightly higher relative intensity of the (200) peak when compared to a standard (Figure 4.1) lead sulfide powder pattern, indicating a small degree of preferred orientation in the films. Peak widths were relatively narrow, indicating relatively large particles. Particle sizes estimated using the Scherrer equation[2] are shown for each quantifiable reflection in table 1. These crystallite size estimations are largest for those planes corresponding to the cube faces of the PbS sodium chloride structure ((200) and (400)) and smallest for those corresponding to

higher energy faces ((331) and (422)). In general, the typical crystallite size estimate is approximately 20-30 nm.

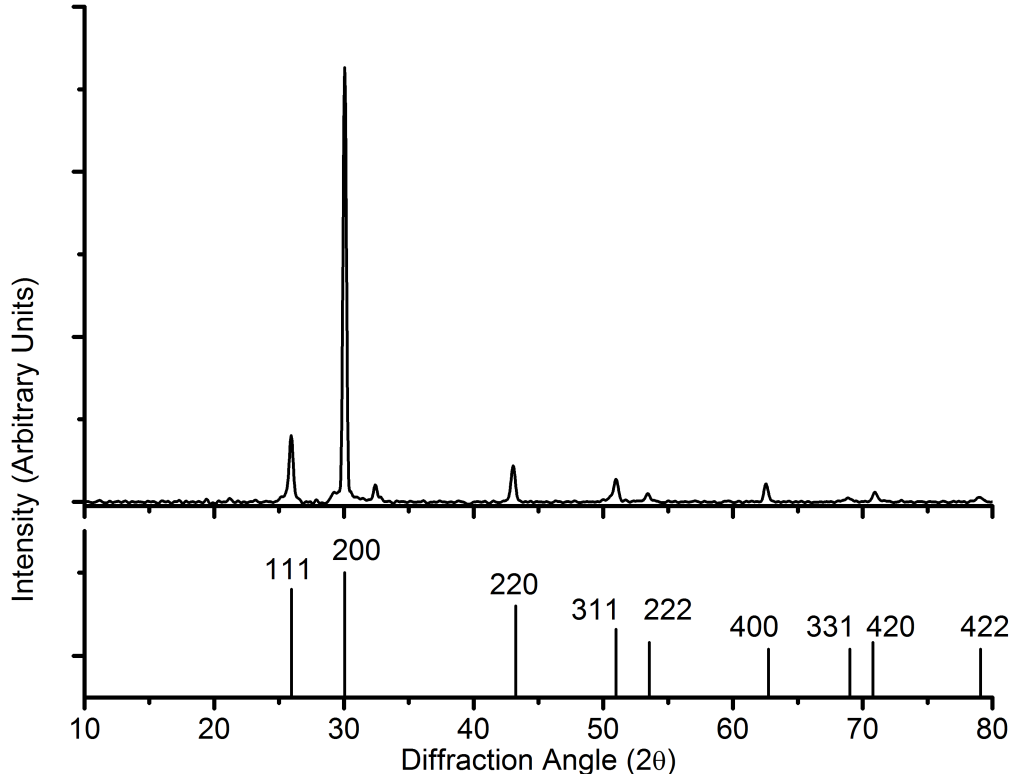

Figure 4.1: XRD of a sample synthesised using 1.67 mM solutions of lead DETC and sodium sulfide at solvent heights of 19±1 mm. XRD pattern of lead sulfide is provided as a reference[10].

Reflection	Estimated particle size (nm)
(111)	24.9±1.2
(200)	32.3±1.6
(220)	25.9±1.3
(311)	22.6±1.1
(222)	24.7±2.5
(400)	29.1±2.9
(331)	15.4±1.5
(420)	25.7±2.6
(422)	19.7±2.0

Table 1: Table of estimated minimum crystallite sizes from all quantifiable peaks in figure 4.1.

The size estimates given in table 1 are considered a minimum estimate of particle size, as calculated sizes from the Scherrer equation are governed by the sizes of individual crystal domains, of which there may be multiple within a single particle, and the presence of a small amount of peak broadening due to instrumental factors. Instrumental broadening was minimised *via* appropriate configuration of the diffractometer.

4.2.2 SEM

SEM of the film giving the XRD pattern of figure 4.1 is shown in figure 4.2 alongside a 5 micron scalebar. The inset image is taken at a higher zoom, and shown alongside a 1 micron scalebar.

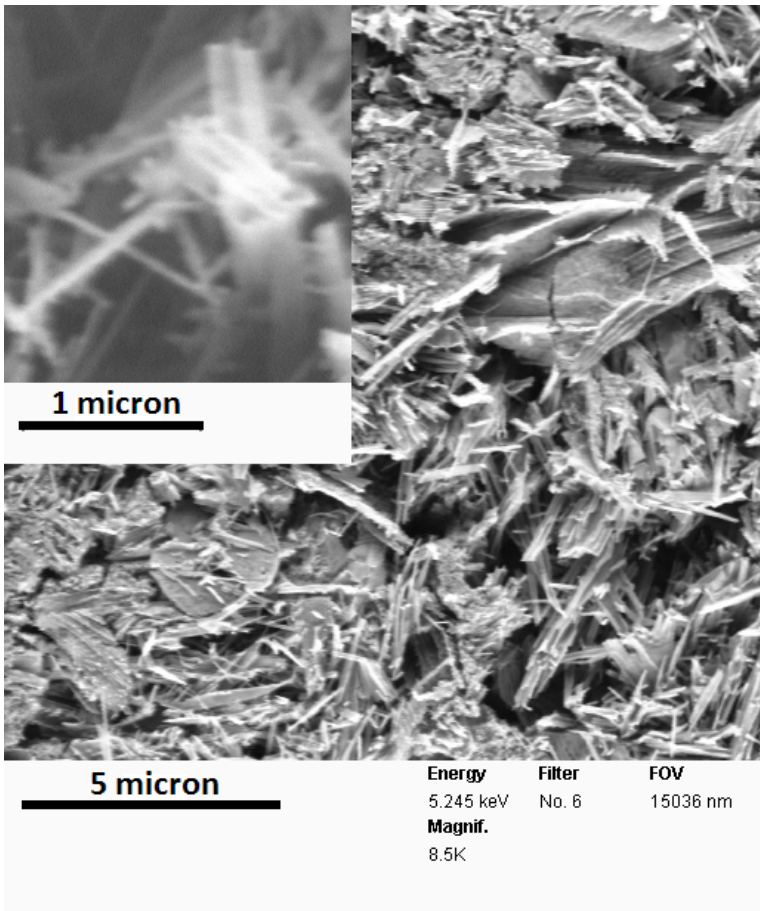

Figure 4.2: SEM micrograph of the sample synthesised using 1.67 mM solutions of lead DETC and sodium sulfide at solvent heights of 19±1 mm.

From the SEM image shown in figure 4.2, it appears that the film consists of thin flakes or long rods of PbS, rather than more isotropic particles. The diameter of the thinnest

measurable rod was approximately 75±5 nm, and the rods typically have lengths on the order of microns. The high aspect-ratio of the particles supports the indication from the XRD size estimates that crystallites have preferential growth along specific planes. The disparity between apparent particle sizes in the XRD and SEM can be explained *via* multiple factors; estimates of particle sizes from the XRD provide a minimum value based upon the crystal domains present – particles visible in SEM may be formed of multiple crystal domains, or indeed even agglomerates of individual particles.

4.2.3 X-ray photoelectron spectroscopy

Figure 4.3 shows XPS of the same sample, taken at the National Centre for Electron Spectroscopy and Surface Analysis (NCESS) in Daresbury, Warrington.

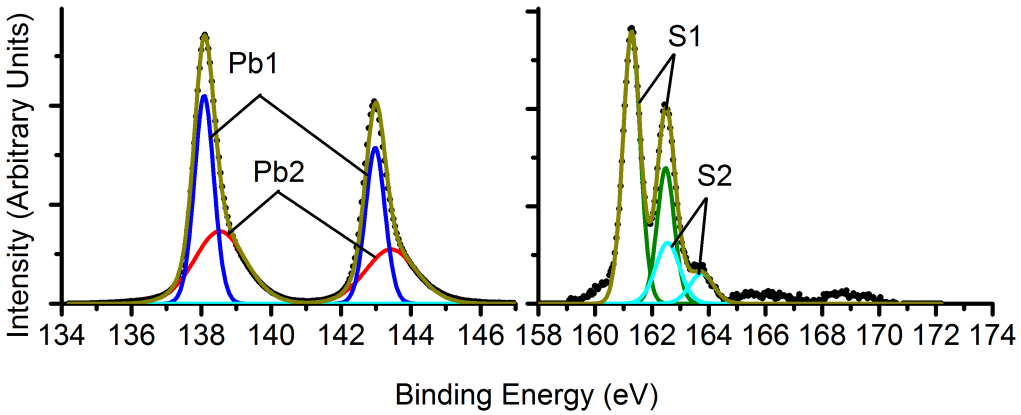

Figure 4.3: XPS of lead 4f and sulfur 2p regions for a sample synthesised with sodium sulfide. The sample was introduced to vacuum approximately two weeks after synthesis, and was examined at a photon energy of 1486 eV, corresponding to a sampling depth of ~8.8 nm at the lead 4f and sulfur 2p binding energies.

Peak assignments are given in table 2. Sulfur 2p peaks for sulfoxy species ($PbSO_3$ and $PbSO_4$) occur between binding energies of 164 eV and 172 eV if present. A small amount of oxidised sulfur species can be seen, but these were not large enough to be accurately fitted. The ratio of lead to sulfur observed was 1 : 1.15, and the ratio of lead in lead sulfide to oxidised lead species was 1:1.09. The large proportion of observed oxidised lead species (Pb2) in comparison to oxidised sulfur species is believed to be due to oxidation proceeding *via* initial separation of lead and sulfur and formation of lead hydroxide, carbonate, or oxide as has been suggested previously in the literature[3–5]. The binding energy of the oxidised lead species is most consistent with that of lead hydroxide[5].

Peak label	Assignment	Literature Binding Energy (eV)	Observed Binding Energies (eV)	Observed FWHM (eV)
Pb1	Lead in PbS	138	138	0.7
Pb2	Oxidised lead	~138.4 - 139	138.55	1.7
S1	Sulfur in PbS	161.1	161.3	0.7
S2	Neutral sulfur	162	162.55	1

Table 2: Table of peak assignments. Spectra were aligned to the binding energy of the lead 4f PbS peak at 138 eV[3,5,6] . Binding energies refer to the lower binding energy peak of a doublet.

4.3 Effect of varying solvent height

Samples synthesised using lead DETC and sodium sulfide nonahydrate precursors at solvent heights of 19±1, 22±1 and 25±1 mm were investigated *via* the use of XRD and XPS. The results of this characterisation are presented below.

4.3.1 X-ray diffraction

Figure 4.4 shows XRD of samples synthesised using lead DETC and sodium sulfide nonahydrate precursors at solvent heights of 19±1, 22±1 and 25±1 mm.

As with the sample synthesised using sodium sulfide, all of these samples show similar lead sulfide diffraction patterns with a slightly higher than expected intensity of (200) planes relative to a standard lead sulfide powder diffraction pattern. Estimated minimum crystallite sizes are shown in figure 4.5.

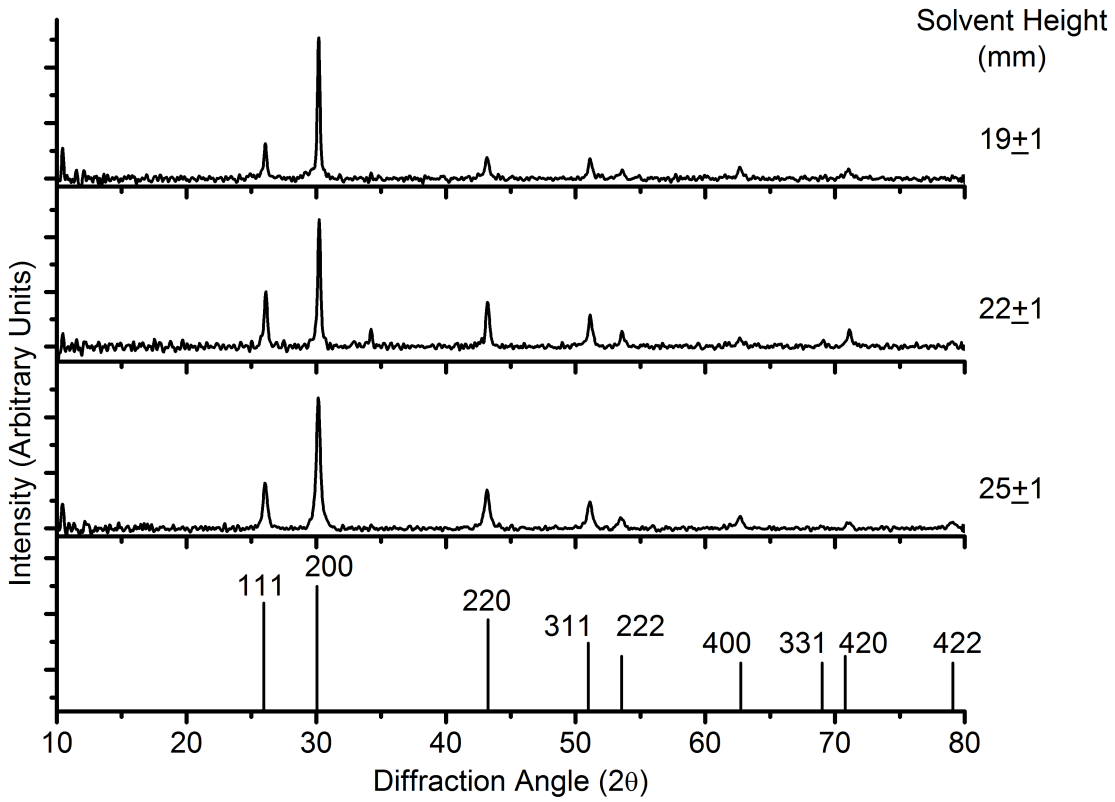

Figure 4.4: XRD patterns of samples synthesised at varying solvent heights using the sodium sulfide nonahydrate precursor. XRD pattern of lead sulfide is provided as a reference[10].

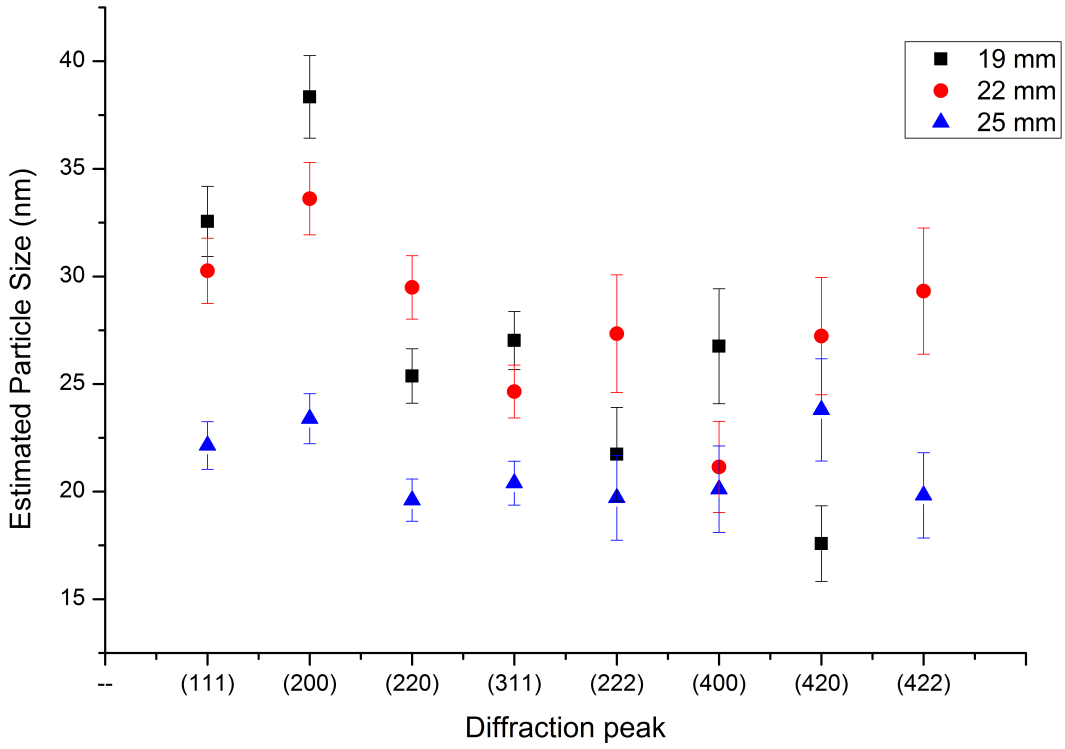

Figure 4.5: Estimated particle sizes from all quantifiable diffraction peaks for samples at various solvent heights (Solvent heights shown in legend).

As with the initial synthesis attempts using sodium sulfide, the samples synthesised using sodium sulfide nonahydrate also show a moderate amount of preferential growth, with the (111) and (200) planes typically having the highest particle size estimates. This preferential growth is greatest in the sample synthesised at a solvent height of 19 mm, with the difference between the highest and lowest particle size estimates decreasing for the sample synthesised at a 22 mm solvent height, and the lowest spread in particle size estimates for the sample synthesised at a solvent height of 25 mm. The particle size follows a similar trend, with the sample synthesised at a solvent height of 25 mm having the lowest average estimated particle size.

4.3.2 X-ray photoelectron spectroscopy

XPS of the samples synthesised at varying solvent heights was performed at beamline I311 at MAXLab synchrotron, Sweden. Samples were exposed to air for approximately a week between synthesis and introduction to vacuum.

Spectra from a variety of sampling depths were obtained *via* varying the energy of photons incident on the sample. This allows control over the kinetic energy of emitted electrons (which will be approximately similar for the lead 4f and sulfur 2p peaks). As electrons with different kinetic energies have different inelastic-mean-free-paths, the proportion of electrons detected from different depths within the material will change with electron kinetic energy. 'Sampling Depth' refers to the depth from which 95% of the signal originates. Sampling depths listed refer to values obtained from data collected by Tanuma, Penn, and Powell[7].

Figures 4.6, 4.7 and 4.8 show XPS spectra at varying sampling depths for the samples synthesised at 19, 22, and 25 mm respectively. Peak assignments are given in table 3.

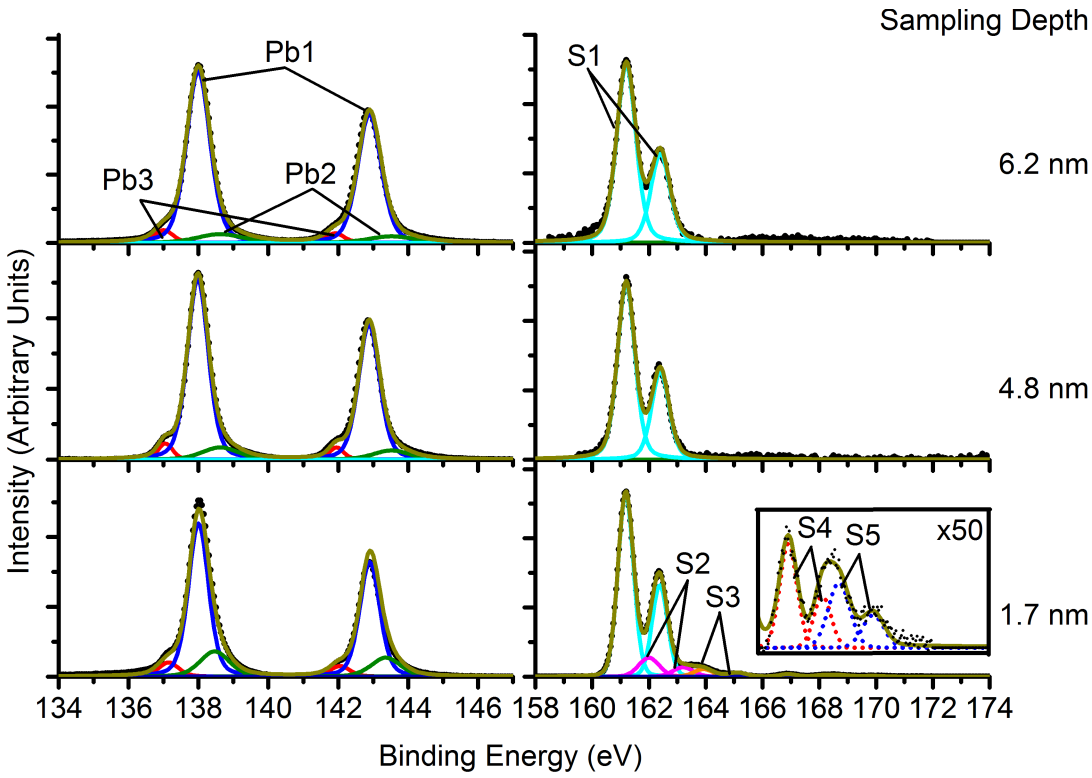

Figure 4.6: Depth profiling XPS spectra of lead 4f and sulfur 2p regions for the sample synthesised at a solvent height of 19 mm. Inset shows oxidised sulfur species at 50x magnification. Sampling depths from top to bottom correspond to photon energies of 1000, 700, and 250 eV respectively.

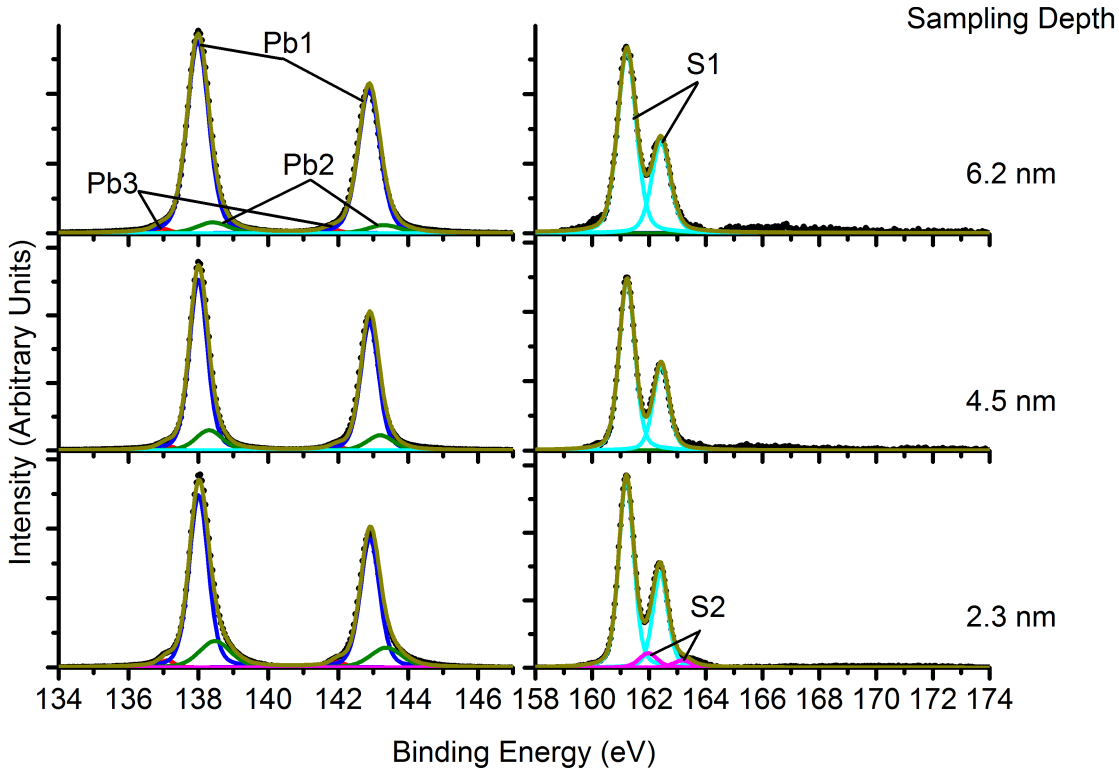

Figure 4.7: Depth profiling XPS spectra of lead 4f and sulfur 2p regions for the sample synthesised at a solvent height of 22 mm. Sampling depths, from top to bottom correspond to photon energies of 1000, 700, and 350 eV respectively.

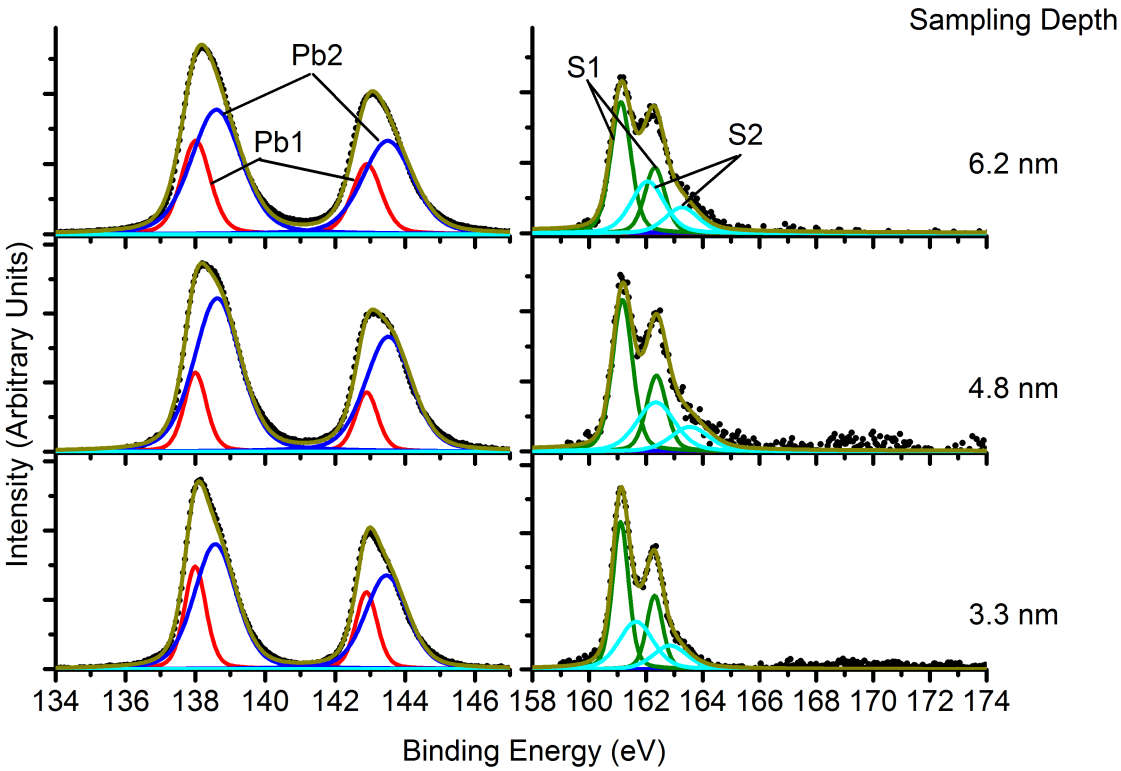

Figure 4.8: Depth profiling XPS spectra of lead 4f and sulfur 2p regions for the sample synthesised at a solvent height of 25 mm. Sampling depths from top to bottom correspond to photon energies of 1000, 700, and 500 eV respectively.

Peak label	**Assignment**	**Literature Binding Energy (eV)**	**Observed Binding Energies (eV)**	**Observed FWHM (eV)**
Pb1	Lead in PbS	138	138	0.6-1.0
Pb2	Oxidised lead	138.4-138.9	138.3-138.65	1.0-1.7
Pb3	Neutral lead	136.8	137-137.15	~0.5
S1	Sulfur in PbS	161.1	161.1	0.6-0.9
S2	Neutral sulfur	162	161.7-162.3	0.8-1.4
S3	$PbSO_n$	~163-165	163.9	~0.8
S4	Sulfur in $PbSO_3$	166.9	166.9	~0.7
S5	Sulfur in $PbSO_4$	168.6	168.7	~0.9

Table 3: Table of peak assignments. Spectra were aligned to the binding energy of the

lead 4f PbS peak at 138 eV [3,5,6,8]. Binding energies refer to the lower binding energy peak of a doublet.

The samples synthesised at solvent heights of 19 and 22 mm display very little oxidation of the sulfur, with oxidised sulfur species only being visible in very small amounts at a sampling depth of 1.7 nm in the sample synthesised at a 19 mm solvent height. No oxidation was seen at all in the sample synthesised at a solvent height of 22 mm, however a small amount of neutral sulfur is present at the lowest sampling depths for both of these samples. Both 19 and 22 mm samples show a small amount of neutral and oxidised lead species throughout. The sample synthesised at a solvent height of 25 mm however, displays a relatively large amount of an oxidised lead species, as well as a relatively large amount of neutral sulfur throughout. There is still very little oxidation of the sulfur visible in this sample. This supports the suggestion that the initial oxidation process involves decomposition of the lead sulfide and oxidation of the resultant lead. As previously, the oxidised lead species observed are most consistent with literature values for lead hydroxide[5]. The small amounts of neutral lead seen in several of these samples are believed to have been formed due to degradation of the sample under exposure to synchrotron radiation, as they have not been observed in the lab-based XPS.

Figures 4.9, 4.10, and 4.11 show the measured ratios for all solvent heights of; lead in lead sulfide to oxidised lead; sulfur in lead sulfide to oxidised sulfur; and total lead to total sulfur.

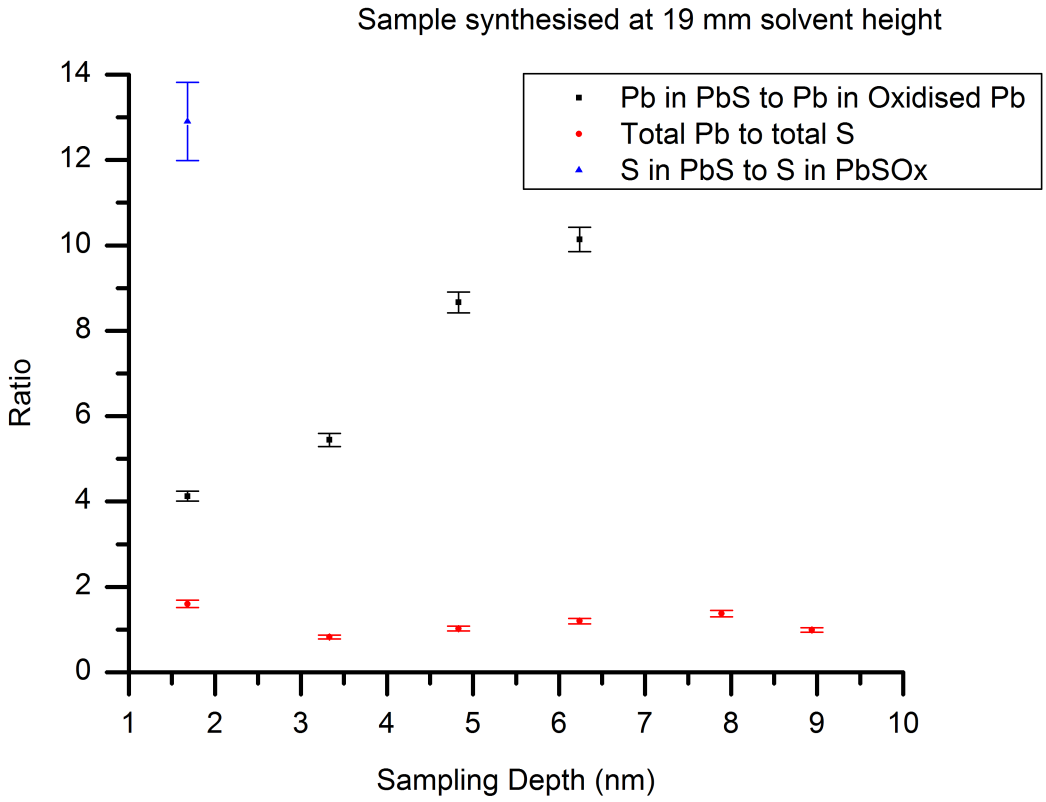

Figure 4.9: Ratios from XPS of total lead to sulfur, lead in lead sulfide to oxidised lead species, and sulfur in lead sulfide to oxidised sulfur species at varying sampling depths for the sample synthesised at 19 mm solvent height.

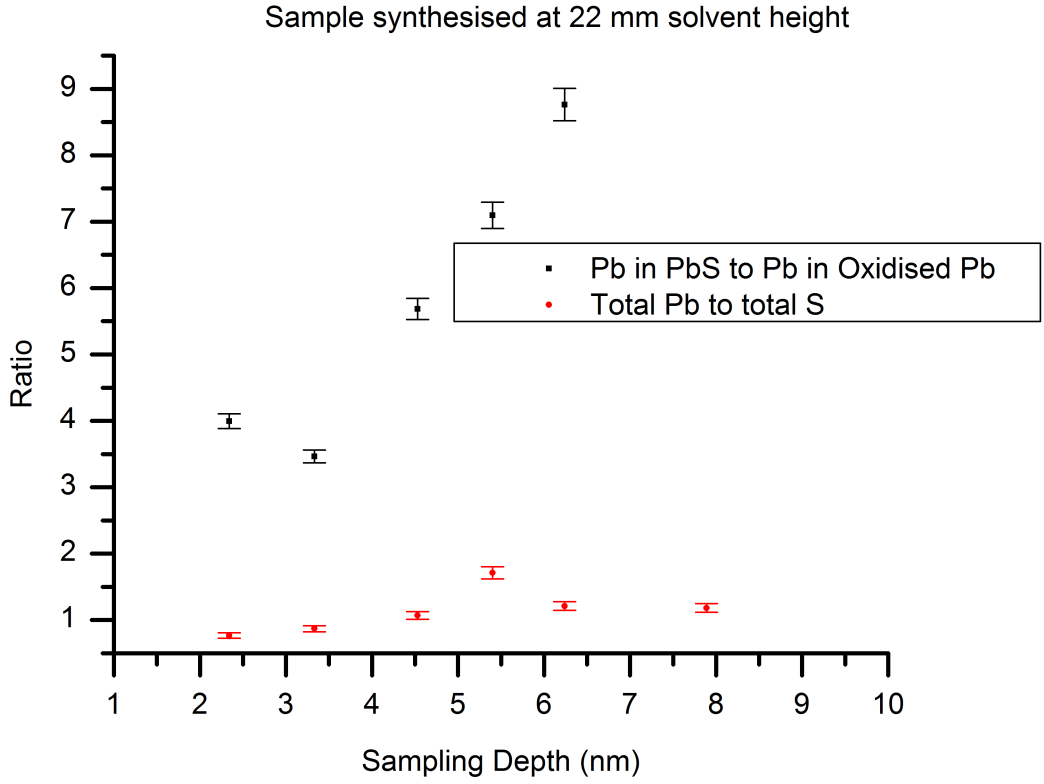

Figure 4.10: Ratios from XPS of total lead to sulfur and lead in lead sulfide to oxidised lead species at varying sampling depths for the sample synthesised at 22 mm solvent height.

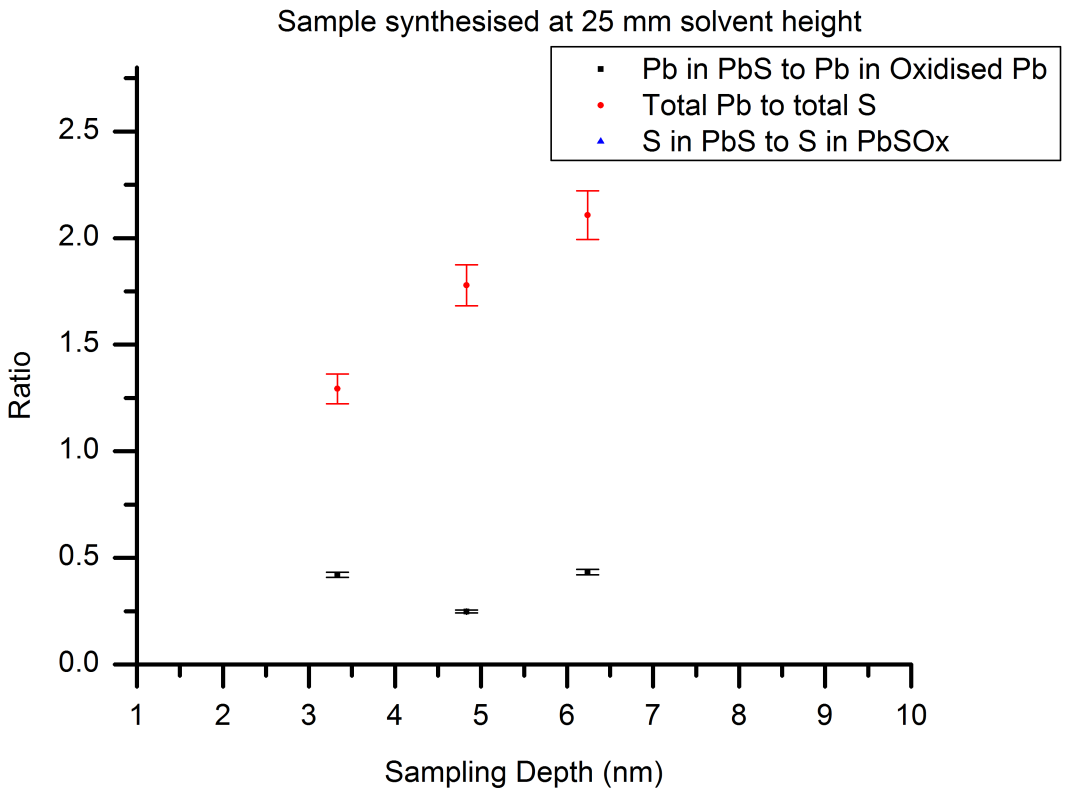

Figure 4.11: Ratios from XPS of total lead to sulfur and lead in lead sulfide to oxidised lead species at varying sampling depths for the sample synthesised at 25 mm solvent height.

The samples synthesised at 19 and 22 mm solvent heights both show very similar behaviour with regards to ratios of species present. Both show a significant rise in the ratio of lead in lead sulfide to oxidised lead species, indicating concentration of the oxidation on the surface of the particle. They also show a relatively uniform ratio of lead to sulfur throughout, approximately in the region of 1:1. A slight increase in lead to sulfur ratio with sampling depth can be seen in the sample synthesised at a solvent height of 22 mm. The sample synthesised at a solvent height of 25 mm however displays significantly different properties, with a lead in lead sulfide to oxidised lead ratio that is low throughout the sample, and a ratio of total lead to total sulfur that is greatest at the largest sampling depth. As the ratio of lead to sulfur is above 1:1 throughout, it is unlikely that this is due to lead being lost from the surface of the particles. A possible explanation for this is that the neutral sulfur mentioned previously is migrating to the surface of the particles, where it may be removed in the vacuum, as has been observed in the literature[4,9]. The sample synthesised at a solvent height of 25 mm displays the greatest proportion of oxidised lead. As this sample exhibited the smallest estimated particle size

from XRD, it is likely that this is due to the effects of the increased surface-area to volume ratio.

Summary and Conclusions

The quality of initial samples synthesised using lead DETC and sodium sulfide was inconsistent across multiple syntheses, likely to be due to the hygroscopic nature of sodium sulfide causing overestimation in the concentration of sulfur ions. SEM of a sample synthesised in this way showed the growth of rod-like structures, while XRD indicated minimum particle sizes much lower in dimension than the observed rods. This suggests a preferential direction of agglomeration of crystallites to produce the longer rod-like structures.

Samples synthesised using lead DETC and sodium sulfide nonahydrate exhibited films of particles with a minimum particle size calculated from XRD peak broadening of approximately 20 nm. Experiments aimed at exploring the effect of solvent height showed a greater degree of preferential growth in samples synthesised at the lower solvent height of 19 mm. Samples synthesised at the greatest solvent height of 25 nm exhibited a more uniform level of peak broadening across all diffraction peaks, as well as a lower average estimated particle size. Relative to previous work on colloidal nanoparticles[6], XPS of all samples displayed a much lower level of surface sulphate formation, however this can likely be explained by the greater relative particle size resulting in a lower surface area to volume ratio and thus a lower rate of oxidation. Neutral sulfur was observed at the surface of samples synthesised at all solvent heights, as well as a greater amount of oxidised lead species present at the surface. Both oxidised lead and neutral sulfur were seen in much greater amounts in the sample synthesised at the highest solvent height indicating that these features are related, and likely due to a process whereby lead sulfide is decomposed into neutral sulfur and oxidised lead.

References

(1) Fan, D. *Thesis submitted to the University of Manchester* **2008**.

(2) Patterson, A. *Physical Review* **1939**, *56*, 978-982.

(3) Park, R. L. *Applications Of Surface Science* **1977**, *1*.

(4) Nowak, P.; Laajalehto, K. *Applied Surface Science* **2000**, *157*, 101-111.

(5) Buckley, A. N.; Woods, R. *Applications of Surface Science* **1984**, *17*, 401-414.

(6) Hardman, S. J. O.; Graham, D. M.; Stubbs, S. K.; Spencer, B. F.; Seddon, E. A.; Fung, H.-T.; Gardonio, S.; Sirotti, F.; Silly, M. G.; Akhtar, J.; O'Brien, P.; Binks, D. J.; Flavell, W. R. *Physical chemistry chemical physics : PCCP* **2011**, *13*, 20275-83.

(7) Tanuma, S.; Powell, C. J.; Penn, D. R. *Surface and Interface Analysis* **1991**, *17*, 927-939.

(8) Yashina, L. V.; Zyubin, A. S.; Püttner, R.; Zyubina, T. S.; Neudachina, V. S.; Stojanov, P.; Riley, J.; Dedyulin, S. N.; Brzhezinskaya, M. M.; Shtanov, V. I. *Surface Science* **2011**, *605*, 473-482.

(9) Hampton, M. A.; Plackowski, C.; Nguyen, A. V. *Langmuir : the ACS journal of surfaces and colloids* **2011**, *27*, 4190-201.

(10) *Lead Sulphide Powder Diffraction File - PDF#00-003-0665 (accessed 21/03/12)*.

Chapter 5: Experiments using lead thiobiuret precursor

5.1 Introduction

Synthesis of PbS nanoparticle films using the lead thiobiuret precursor at solvent heights of 16±1, 14±1, 13±1, 8±1, and 6±1 mm was conducted, and samples were characterised using XRD, TEM, SEM, XPEEM, and XPS. The presence of NaCl as an impurity in the precursor, formed as a byproduct during precursor synthesis, was indicated by XPS and XPEEM of the samples, and by elemental analysis of the precursor. This lead to re-synthesis of the precursor and purification *via* recrystalisation from tetrahydrofuran, performed with assistance from Emmanuel Ezenwa of the School of Chemistry at the University of Manchester, UK. Samples synthesised using this purified version of the precursor were characterised using XPS and XRD and exhibited similar properties to those synthesised using the impure precursor, indicating that the impurity did not significantly effect sample synthesis other than by introducing an error in the calculated concentration. The results of characterisation of the samples synthesised using the lead thiobiuret precursor are presented here.

5.2 Samples synthesised using unpurified precursor

5.2.1 X-Ray diffraction

X-ray diffraction patterns of the samples synthesised using the lead thiobiuret precursor are shown in figure 5.1. Reflections originating from PbS are highlighted. The pattern clearly contains multiple peaks that are not due to PbS. The most readily identifiable of these is the NaCl (200) peak, located at ~31.5^{o} in every pattern. Other reflections present , particularly those in every sample located at ~13^{o}, ~34^{o}, and ~40^{o}, are presumed to be a combination of peaks arising from the NaCl impurity and biproducts of the lead precursor. The peak assigned to the PbS (111) reflection (located at ~26^{o}) is further complicated by the fact that it forms a shoulder on the lower diffraction angle side of the NaCl (111) peak. Although the signal is small, there are clearly peaks arising from PbS present in every diffraction pattern, confirming that PbS was successfully synthesised using this precursor. The low signal of these peaks relative to the impurities is likely due to the broadening of the PbS peaks due to their size, which reduces their intensity. Particle sizes estimated using the Scherrer equation[1] from all quantifiable PbS reflections are given in figure 5.2.

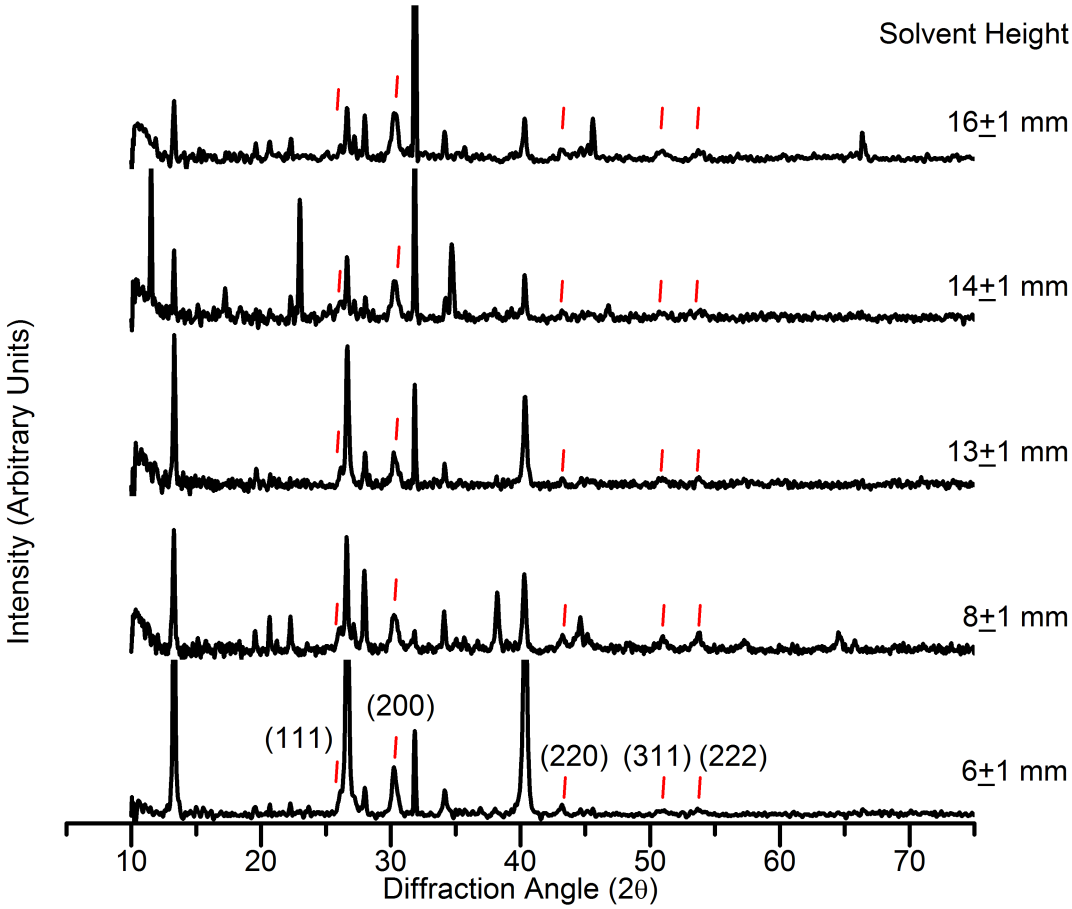

Figure 5.1: X-ray diffraction patterns of samples synthesised using the unpurified lead thiobiuret precursor at a range of solvent heights.

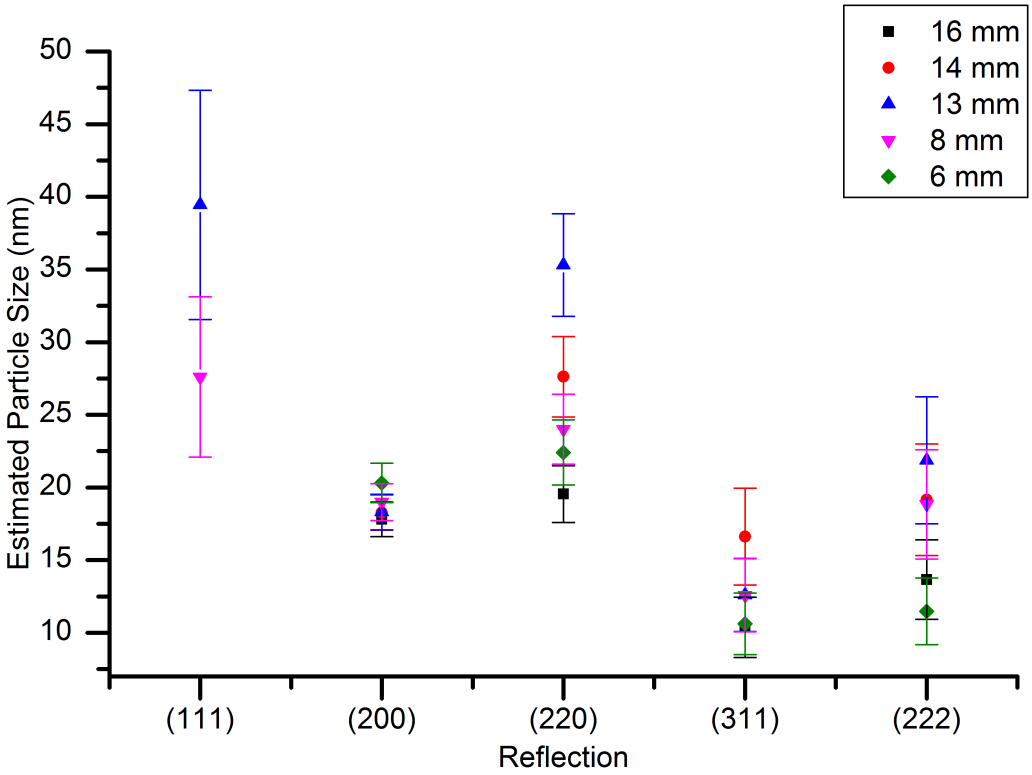

Figure 5.2: Estimated particle sizes from all quantifiable PbS reflections for each sample.

All samples display a fairly similar variation in estimated particle size across the different reflections. The smallest particle sizes consistently appear in the samples synthesised at 6 and 16 mm solvent heights, with the exception of the (200) reflection, for which particle size consistently decreases with increasing solvent height, however this may be attributable to error, as this sample also exhibits the least variation in size across all samples.

5.2.2 TEM

The samples were transferred onto carbon-film-coated copper TEM grids immediately following synthesis, and examined using a Delong Low-Voltage Electron Microscope (LVEM)[2] operating in TEM mode. The grey background visible in all images is the carbon film.

Figure 5.3 shows particles and agglomerates from the sample synthesised at a solvent height of 16±1 mm. A broad range of agglomerate sizes can be observed, with the smallest particles visible (shown in figure 5.4) being ~10 nm in size. Larger portions of film were observed; these cannot be penetrated by the electron beam and therefore appear opaque.

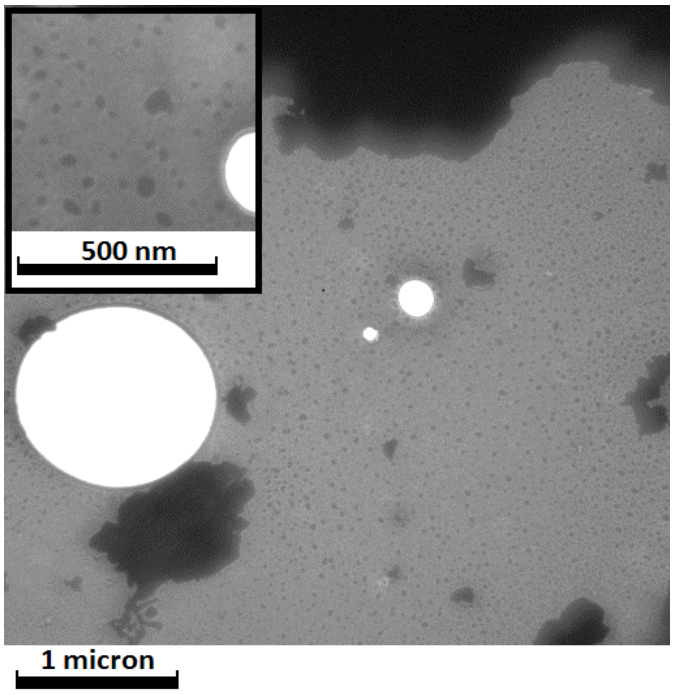

Figure 5.3: Transmission electron micrograph of a sample synthesised using the unpurified lead thiobiuret precursor at solvent height of 16±1 mm.

Figure 5.4 show particles and agglomerates from the remaining samples, synthesised at solvent heights of 14, 13, 8 and 6 mm. In general these samples were similar in appearance to the sample shown in figure 5.3, exhibiting broad ranges of particle agglomerates of different sizes, and a background of smaller particles, typically ~10 nm in diameter. A tendency towards a greater proportion of large agglomerates was seen with decreasing solvent height, with the sample synthesised at a solvent height of 6 mm consisting almost entirely of large branching agglomerates of particles on the order of ~20 nm in size. Whether or not smaller particles were present in this sample however may have been obscured by a lack of good signal and image contrast.

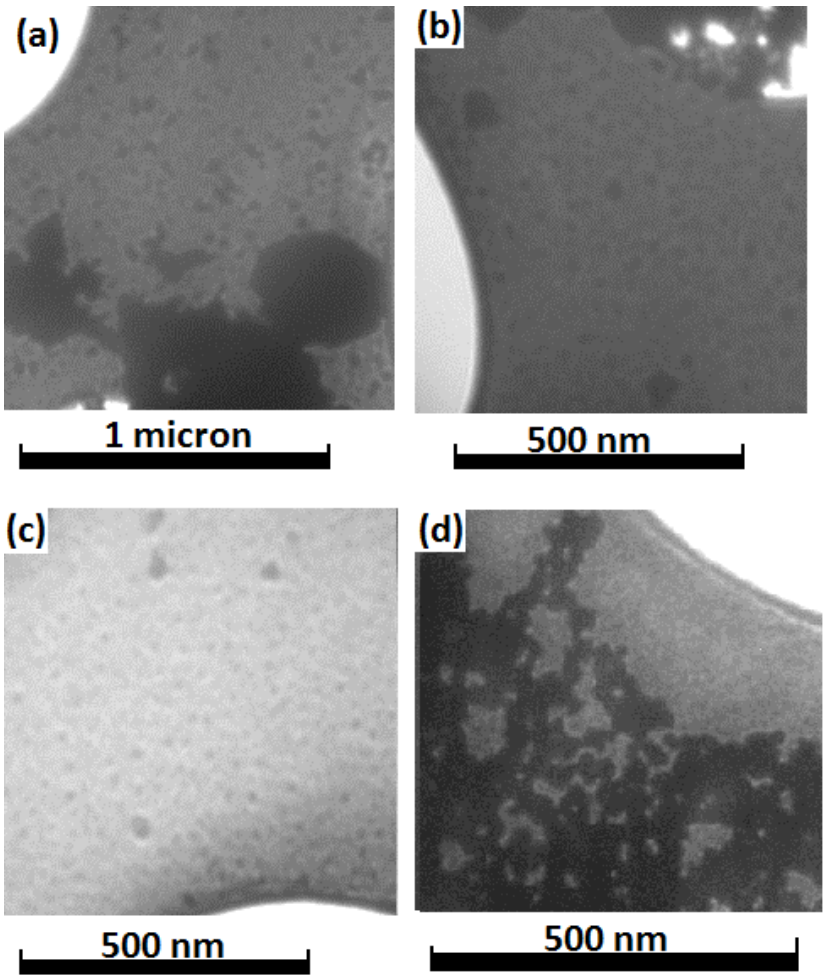

Figure 5.4: Transmission electron micrographs of samples synthesised using the unpurified lead thiobiuret precursor at solvent heights of (a): 14±1 mm; (b): 13±1 mm; (c): 8±1 mm; (d): 6±1 mm.

5.2.3 X-ray photo-electron emission microscopy.

X-ray photo-electron emission microscopy (XPEEM) was performed at beamline I311 at MAXLab synchrotron, Sweden. XPEEM operates *via* the same principles as XPS – electrons are ejected from the sample by the process of photo-emission due to an incident beam of x-ray radiation. As with XPS, the detected electrons are limited to those of a specific kinetic energy range. These electrons are then focussed through a series of lenses to provide an image. Contrast in this image is determined by the intensity of emitted electrons. In this way it is possible to achieve spacial resolution of the distribution of a photo-emission peak within a sample – in essence providing a way to image the amount of a particular element present throughout a sample. While the resolution of this technique is not ideal (being on the order of ~40 nm) the ability to observe variation in composition across a sample is extremely useful.

XPEEM was carried out upon the samples synthesised at solvent heights of 8 mm and 16 mm. The signal at binding energies of ~20 eV and ~160 eV was monitored in order to observe relative amounts of lead and sulphur within the samples from the lead 5d and sulfur 2p peaks. Initially images were also taken at energies corresponding to the lead 4f peaks, however it was found that the lead 5d peak gave far better signal.

Figures 5.5 and 5.6 show the relative intensities of the lead 5d and sulfur 2p peaks throughout the sample synthesised at a solvent height of 8mm. Overall the two elements are fairly uniformly distributed relative to each other. Their relative intensities are positively correlated, with 'holes' in the same locations for both elements, and regions of higher or lower intensity matched in both images. There are a few areas which show slightly lower intensity of one element that do not correspond to a similar area of the other, but these are typically small.

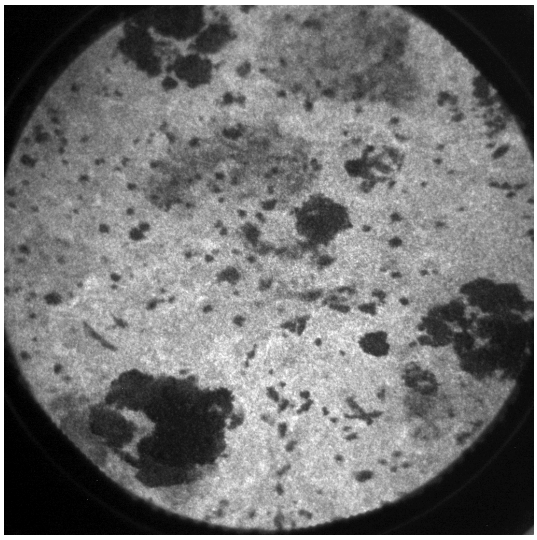

Figure 5.5: An XPEEM image showing the relative intensity of the S 2p emission peak throughout a section of the sample synthesised at a solvent height of 8 mm.

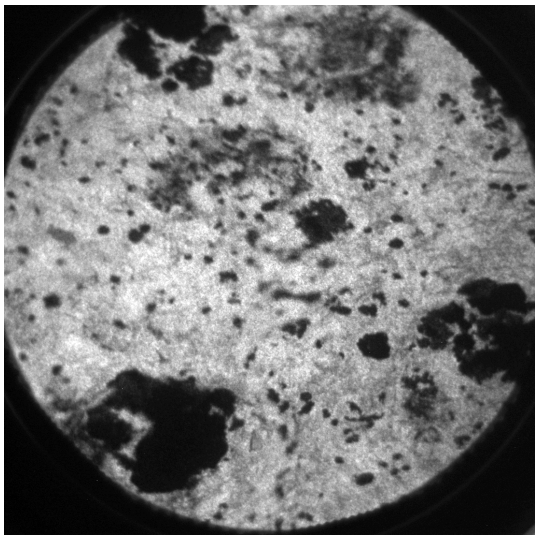

Figure 5.6: An XPEEM image showing the relative intensity of the Pb 5d emission peak throughout a section of the sample synthesised at a solvent height of 8 mm.

Due to concerns over the purity of the sample, potential impurities were also imaged. Concerns that the organic portion of the lead thiobiuret precursor may have contaminated the film prompted imaging of the carbon 1s peak at a binding energy of ~290 eV, this showed a low level of carbon evenly distributed throughout the entire sample. Another potential impurity identified was sodium chloride, produced as a by product during the synthesis of the precursor.

Figure 5.7 shows an image taken at a binding energy of ~30 eV corresponding to the sodium 2p peak. It is clear from this image that there were large amounts of sodium concentrated in regions of the sample where both lead and sulfur were less intense. The sodium appears to be localised to these regions, suggesting that the NaCl is inhomogeneously distributed throughout the film and did not affect the growth of the film as a whole.

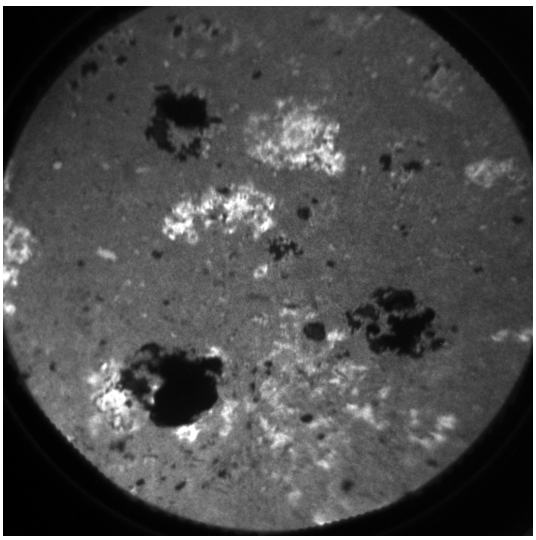

Figure 5.7: An XPEEM image showing the relative intensity of the Na 2p emission peak throughout a section of the sample synthesised at a solvent height of 8 mm.

Similar images were taken for the sample synthesised at a solvent height of 16mm, and are shown in figures 5.8, 5.9, and 5.10. As with the previous images, the sodium is localised in areas where the lead and sulfur are less intense. A notable trend that is more apparent here is the concentration of the sodium around the blank areas within the image. The blank spots are likely to be due to areas that are charging under the synchrotron beam, and thus producing no signal – concentrations or large crystals of NaCl have lower conductivity than the PbS film and thus are more prone to charging in XPEEM.

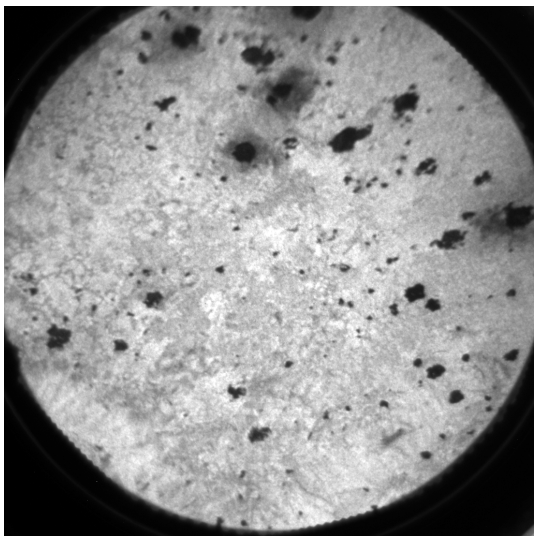

Figure 5.8: An XPEEM image showing the relative intensity of the Pb 5d emission peak throughout a section of the sample synthesised at a solvent height of 16 mm.

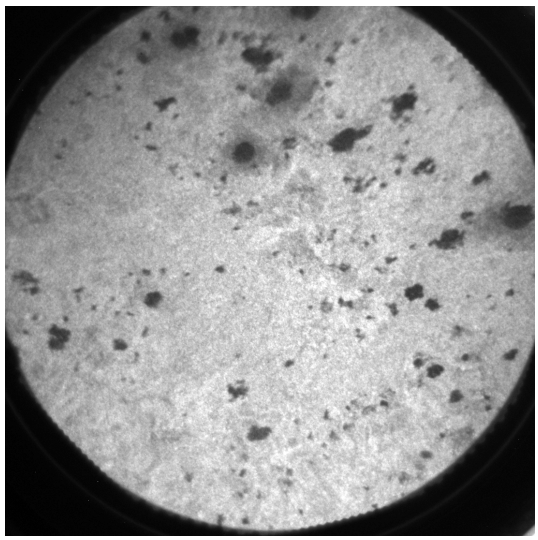

Figure 5.9: An XPEEM image showing the relative intensity of the S 2p emission peak throughout a section of the sample synthesised at a solvent height of 16 mm.

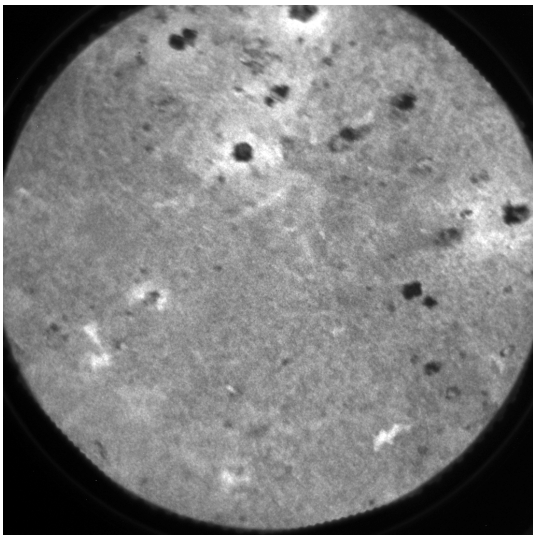

Figure 5.10: An XPEEM image showing the relative intensity of the Na 2p emission peak throughout a section of the sample synthesised at a solvent height of 16 mm

5.2.4 X-ray photo-electron spectroscopy

XPS was carried out at beamline I311 at MAXLab synchrotron, Sweden. The samples were scanned using various photon energies from 398 eV to 1400 eV. Samples were introduced to vacuum within 19 days of synthesis.

Figure 5.11 shows the lead 4f photo-emission peaks for all samples, as observed at a photon energy of 398 eV, corresponding to a sampling depth of ~2.7 nm[3]. The doublets labelled 'Pb1' and 'Pb2' were assigned to lead as found in lead sulfide, and oxidised lead species respectively. Binding energies were calibrated to literature values for the lead 4f PbS peak[4].

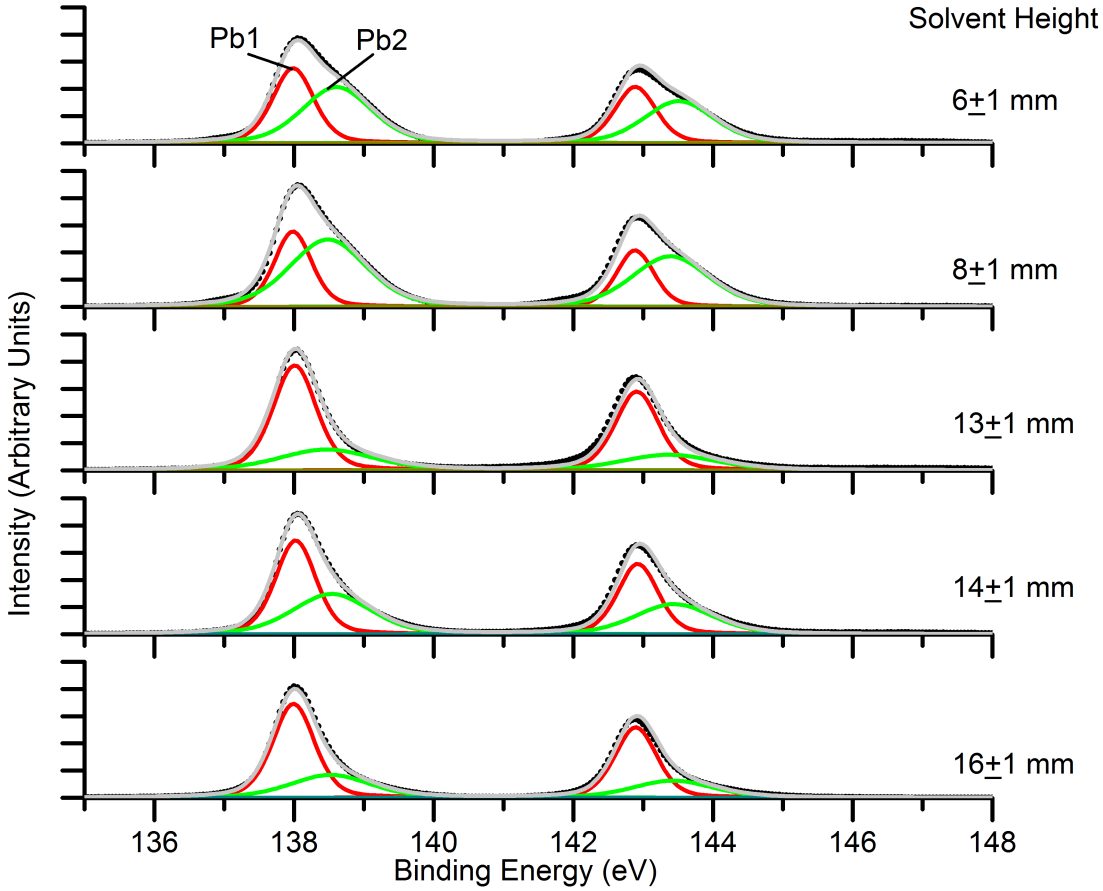

Figure 5.11: A graph showing the lead 4f peaks at a photon energy of 398 eV, corresponding to a sampling depth of 2.7 nm, for all solvent heights.

The lowest amount of oxidised lead was observed in the sample synthesised at 13 mm, which had the largest average calculated particle size from the XRD, suggesting that this

may be due to the lower surface-area to volume ratio. For the other samples, however, the proportion of oxidised lead does not follow any clear relationship with estimated particle size, as the sample synthesised at 16 mm had the smallest average estimated particle size , and yet also displays a relatively low amount of oxidised lead species. This is potentially due to the estimated particle sizes from the XRD representing a minimum particle size, and the broad size dispersion of particles within the films may mean that the average particle size throughout the film may differ from the estimated value significantly.

Figures 5.12 and 5.13 show the sulfur 2p peaks for all samples, observed at a photon energy of 398 eV, corresponding to a sampling depth of ~2.7 nm[3]. The various species were assigned as shown in table 1. There is a small but noticeable shoulder on the S2p PbS peak for most samples, although due to its low intensity it could only be fitted in the scan of the sample synthesised at a solvent height of 16 mm (in which it is labelled S3, see figure 5.13). This is attributed to partially oxidised lead sulfide[5]. A small amount of neutral sulfur, potentially present as part of an initial oxidation step, was also potentially present in several of the samples, though due to low intensity it could only be fitted in the scan of the sample synthesised at a solvent height of 14 mm. There is no clear relationship between solvent height and oxidation visible in the sulfur 2p peak.

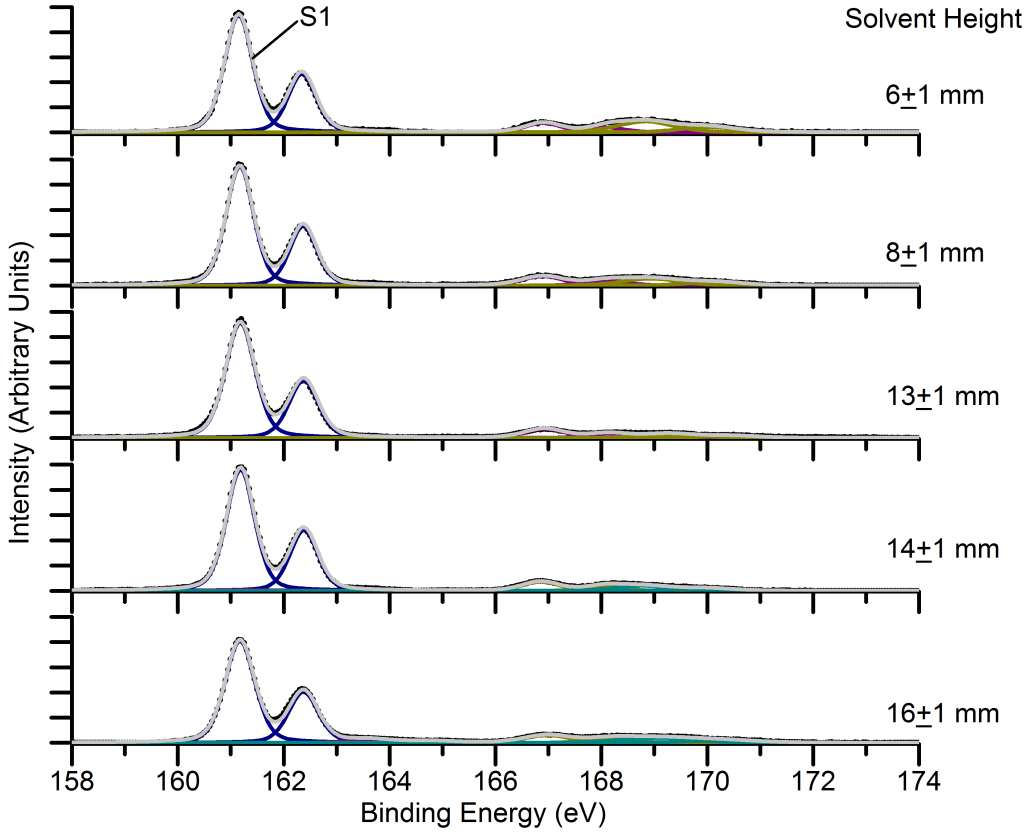

Figure 5.12: A graph showing XPS of the sulfur 2p peaks at a photon energy of 398 eV for all samples.

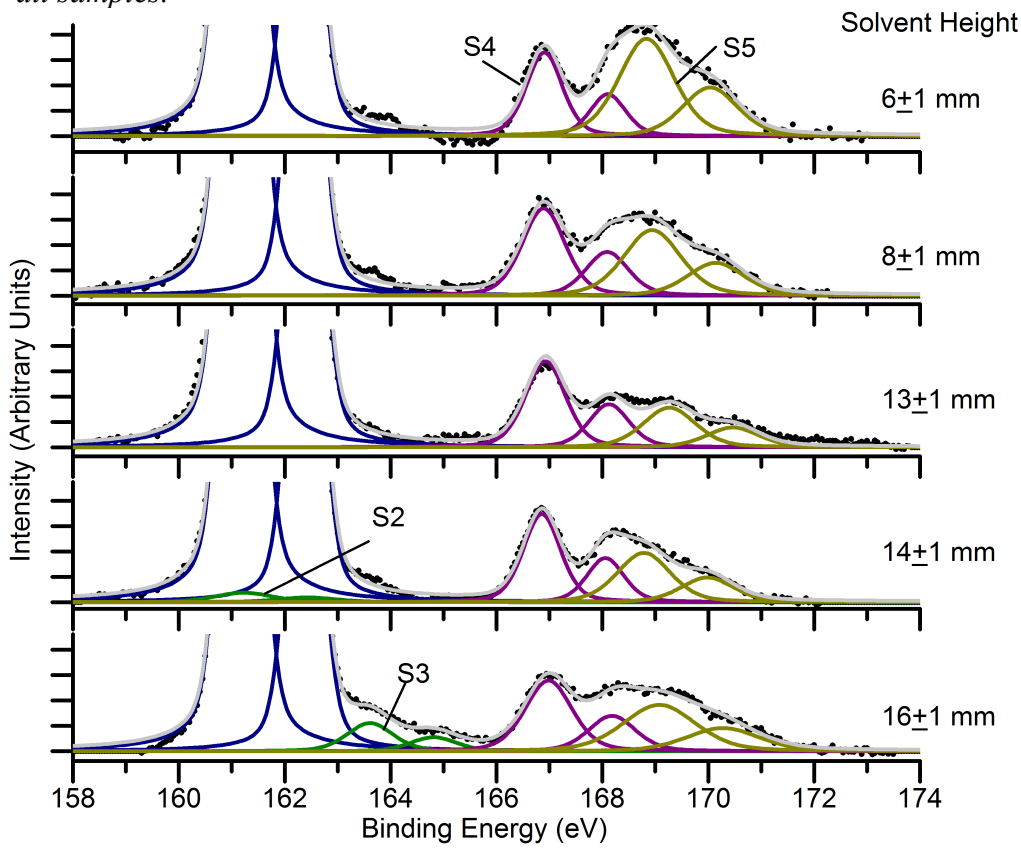

Figure 5.13: A graph showing XPS of the sulfur 2p peaks at a photon energy of 398 eV for all samples, 10x magnified in comparison to figure 5.12, to show the detail of the oxide species.

Peak label	Assignment	Literature Binding Energy (eV)	Observed Binding Energies (eV)	Observed FWHM (eV)
Pb1	Lead in PbS	138	138	0.7
Pb2	Oxidised lead	138.4-138.9	~138.45	1.2-1.7
Pb3	Neutral lead	136.8	-	-
S1	Sulfur in PbS	161.1	161.1	0.6-0.8
S2	Neutral sulfur	162	~161.3	~1.0
S3	$PbSO_n$	~163-165	163.6	~1.0
S4	Sulfur in $PbSO_3$	166.9	166.9	0.8-1.0
S5	Sulfur in $PbSO_4$	168.6	168.8-169.3	1.0-1.7

Table 1: Table of peak assignments[4–7]

Figures 5.14 to 5.17 show depth profiling spectra of the lead 4f and sulfur 2p peaks of samples synthesised at 6 mm and 16 mm solvent heights. Each figure 5.contains spectra taken at photon energies of 398, 580, and 1000 eV, corresponding to approximate sampling depths (for the lead 4f and sulfur 2p peaks) of 2.7, 3.8, and 6.2 nm^3.

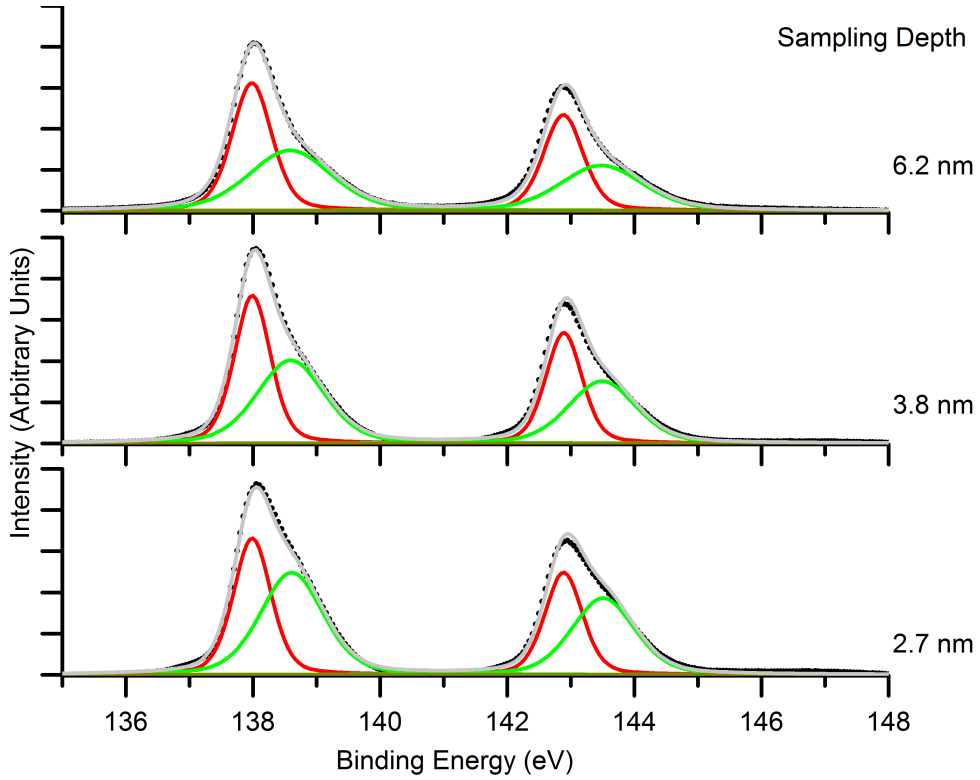

Figure 5.14: Depth profiling spectra for the lead 4f peak of the sample synthesised at 6 mm solvent height. Sampling depths from top to bottom correspond to photon energies of 1000, 580 and 400 eV respectively.

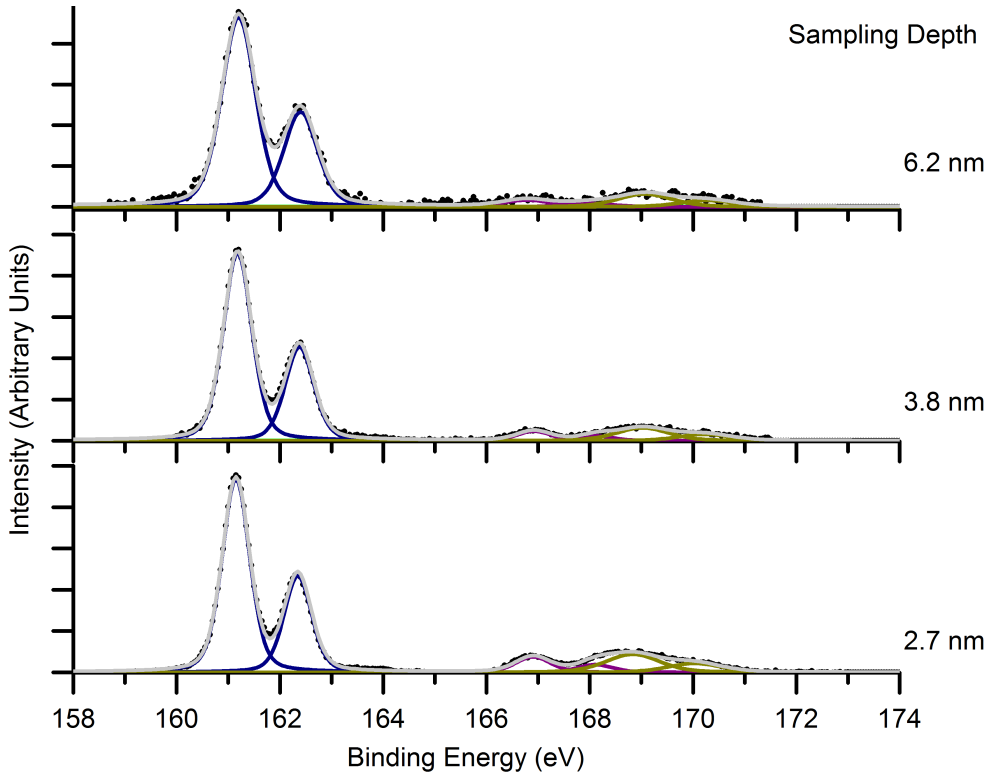

Figure 5.15: Depth profiling spectra for the sulfur 2p peak of the sample synthesised at 6 mm solvent height. Sampling depths from top to bottom correspond to photon energies of 1000, 580 and 400 eV respectively.

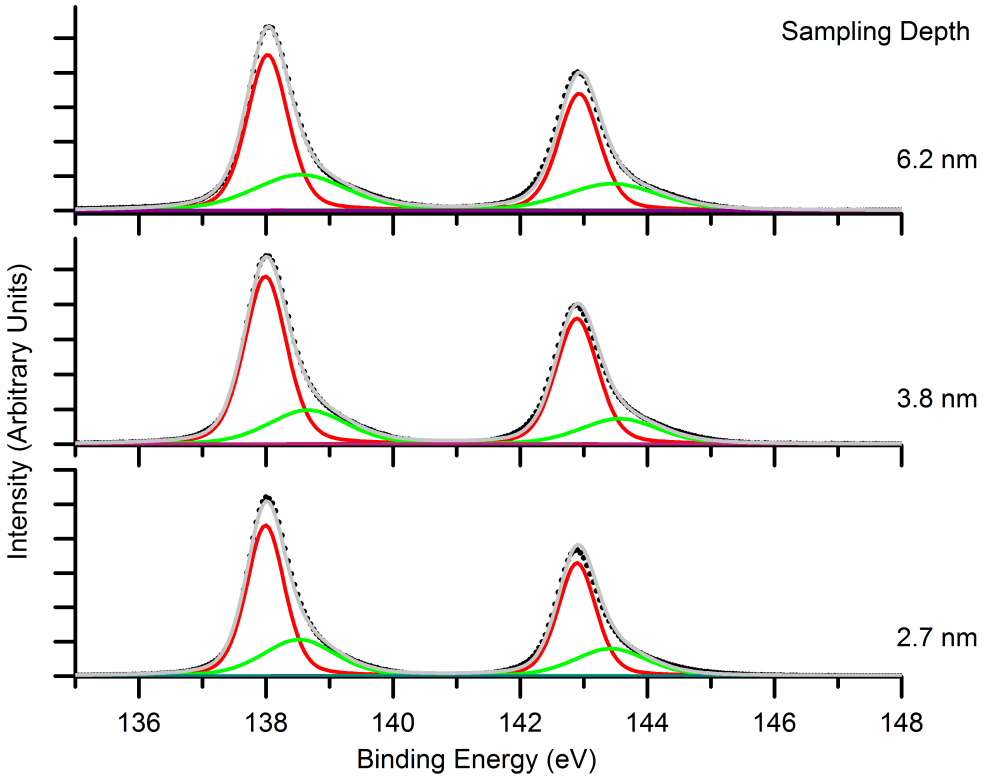

Figure 5.16: Depth profiling spectra for the lead peak of the sample synthesised at 16 mm solvent height. Sampling depths from top to bottom correspond to photon energies of 1000, 580 and 400 eV respectively.

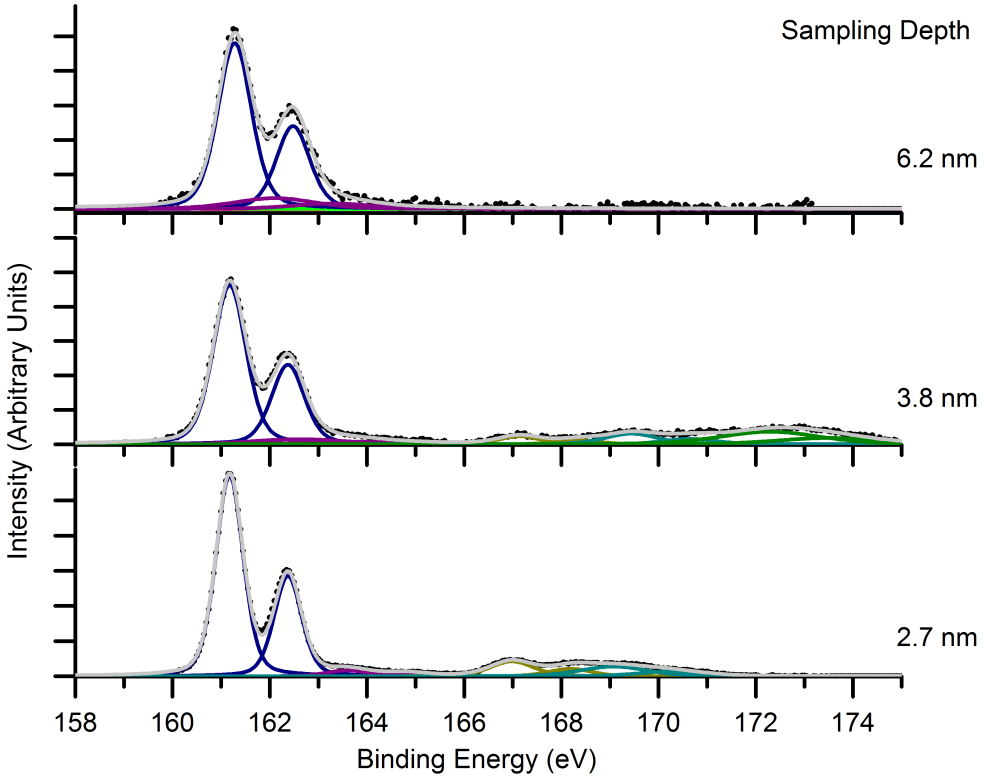

Figure 5.17: Depth profiling spectra for the sulfur 2p peak of the sample synthesised at 16 mm solvent height. Sampling depths from top to bottom correspond to photon energies of 1000, 580 and 400 eV respectively.

For all samples, a slight decrease in oxidised components is seen as the sampling depth increases, which suggests that the oxidation is a result of aging on exposure to air (as opposed to formation during synthesis, which would result in a uniform level of oxidation throughout).

The level of oxidation present in all samples is relatively low at all sampling depths, considering that samples were exposed to air for 19 days between synthesis and introduction to vacuum. This is notable in comparison with previous work on colloidal PbS nanoparticles[4] which exhibited a considerably larger proportion of oxidation after one week of exposure to air.

Tables 2, shows the calculated oxide thicknesses for all samples from sampling depths of 2.7 nm and 3.8 nm. Oxidised layer calculations show approximate oxide thicknesses of less than a tenth of a nanometer for all samples. Calculations were performed using the method outlined by Shard *et al.*[8].

Solvent height at synthesis	Oxidised layer thickness calculated at 2.7 nm sampling depth	Oxidised layer thickness calculated at 3.8 nm sampling depth
6±1 mm	0.107±0.011 nm	0.095±0.010 nm
8±1 mm	0.091±0.009 nm	0.057±0.006 nm
13±1 mm	0.066±0.007 nm	0.039±0.004 nm
14±1 mm	0.069±0.007 nm	0.026±0.003 nm
16±1 mm	0.089±0.009 nm	0.086±0.009 nm

Table 2: Table of calculated oxidised sulfur layer thicknesses from sampling depths of 2.7 nm and 3.8 nm for all solvent heights

The slight decrease in oxide thickness at greater sampling depths is likely due to the morphology or diameter of the particles differing to the morphology and diameter assumed in the calculation. Regardless of this effect, the calculated oxidised layer thicknesses are thin, representing less than a monolayer of $PbSO_n$ species present on the surface of the particles.

Figure 5.18 shows the ratios of total lead to total sulfur, lead in lead sulfide to lead in oxidised species and lead in lead sulfide to sulfur in lead sulfide for all samples as a

function of sampling depth.

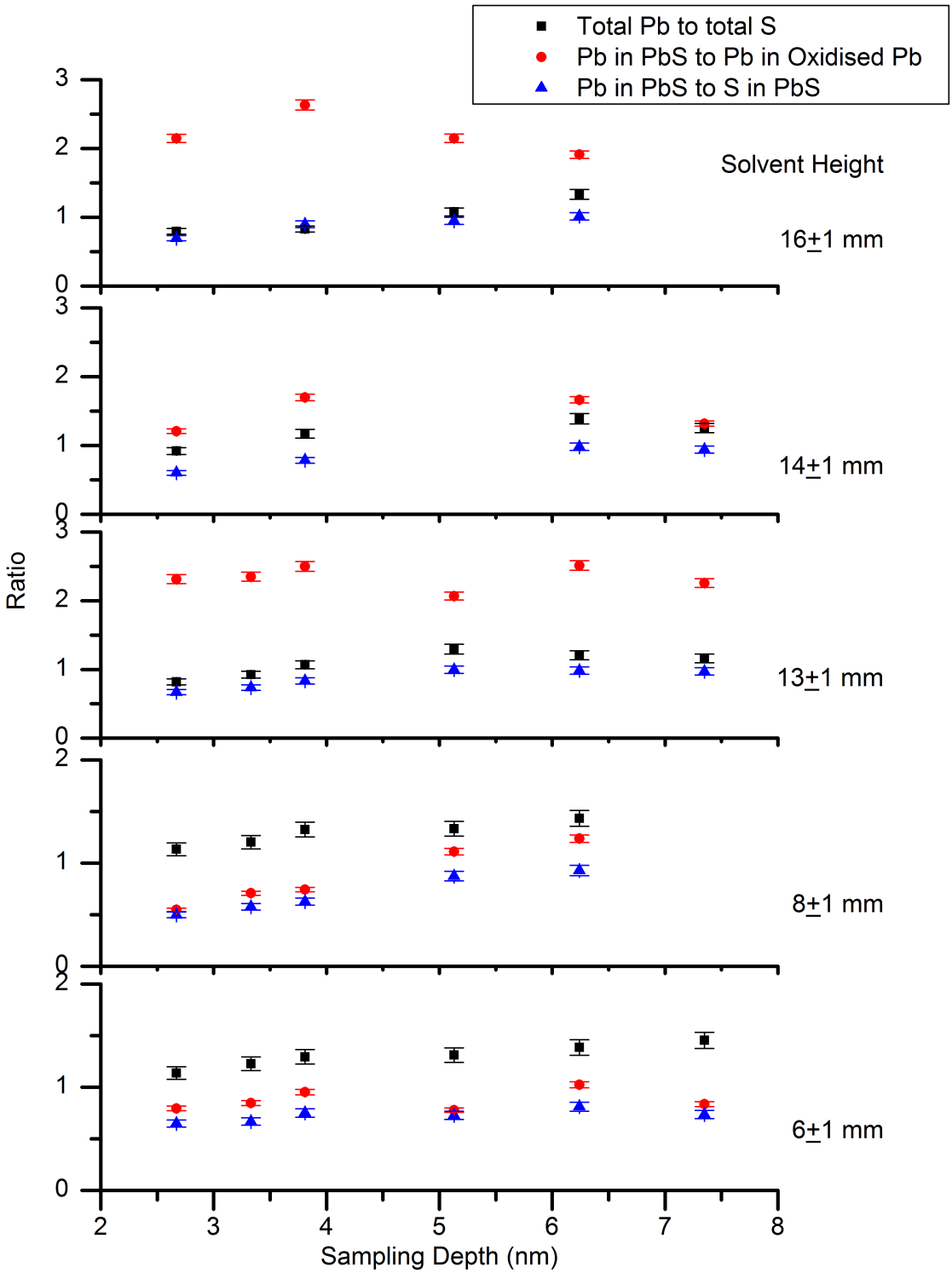

Figure 5.18: Ratios of total lead to total sulfur; sulfur in PbS to sulfur in oxidised species; lead in PbS to lead in oxidised species and lead in PbS to sulfur in PbS for all samples as a function of sampling depth.

A decrease in the PbS to PbSOx ratio (from sulfur 2p peaks) can be seen to occur at some

point between 3.8 and 6.2 nm sampling depths for all samples except the one synthesised at a solvent height of 8 mm. A potential explanation for this is that sampling ratio has begun to sample from the rear lower half of the particle, and thus is detecting an increase in oxide. However, this would not be expected to produce such a consistent feature throughout all samples, and so whether or not this explanation is accurate is unclear.

All samples display an increase of lead to sulfur with increasing sampling depth, and typically display a slight excess of lead, overall. The increase in lead at greater sampling depths is potentially due to the aging process, and will be discussed in detail in chapter 8.

Figure 5.19 shows the ratios of sulfur in PbS to sulfur in PbSOx for all samples as a function of sampling depth. As with the ratio of lead in lead sulfide to lead in oxidised lead species, there is a drop at approximately 5 nm sampling depth in every sample. Otherwise, the ratio of sulfur in lead sulfide to sulfur in sulfoxy species rises consistently throughout the sample, indicating concentration of oxidised species on the surface of the particles. The lowest average ratios of sulfur in lead sulfide to sulfur in sulfoxy species were seen in the samples synthesised at the highest and lowest solvent heights. This is expected considering that these samples had the smallest estimated particle sizes from XRD, and therefore the higher surface-area to volume ratios.

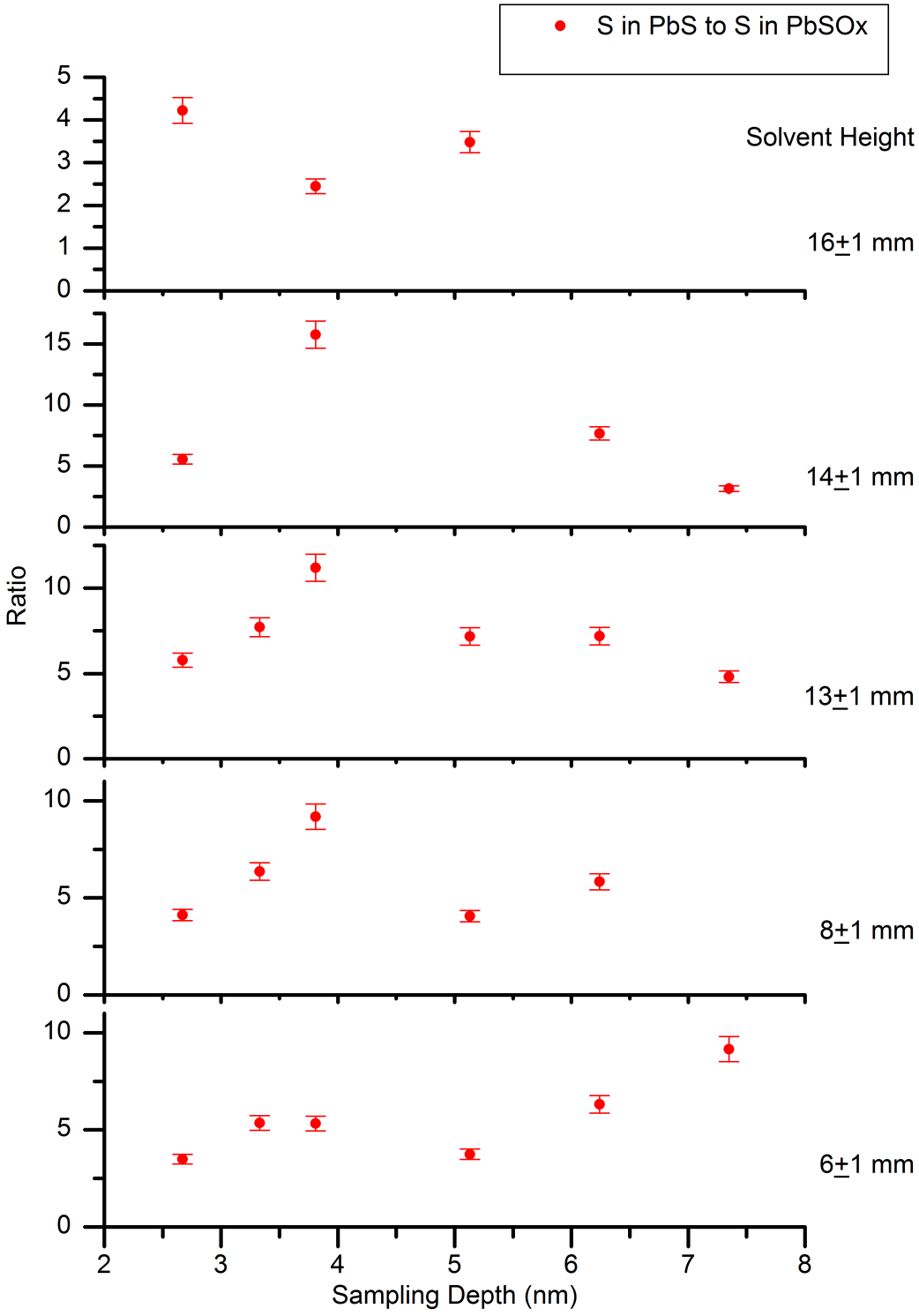

Figure 5.19: Ratio of sulfur in PbS to sulfur in PbSOx for all samples as a function of sampling depth.

5.3 Samples synthesised using purified lead thiobiuret precursor

After determination of the presence of impurities in the original precursor, efforts were made to obtain a purified version. The precursor synthesis was repeated carefully under nitrogen atmosphere, and the resulting product was recrystalised from tetrahydrofuran. Purified precursor synthesis was performed with assistance from Emmanuel Ezenwa of the School of Chemistry, University of Manchester, UK. Elemental analysis confirmed that this resulted in a much purer form of the precursor, which was then used to synthesise samples at solvent heights ranging from 16±1 to 8±1 mm.

5.3.1 X-ray diffraction

Figure 5.20 shows XRD of samples synthesised using the purified precursor. Peaks arising from the (111), (200), (220), (311) and (400) PbS reflections were readily identifiable, and are labelled accordingly. It is immediately apparent that the XRD patterns are substantially 'cleaner' than those from samples synthesised using the unpurified precursor, though there are still some small unidentified peaks at approximately 34^{o}, and in the sample synthesised at 13 mm, an additional unidentified peak at approximately 21^{o}.

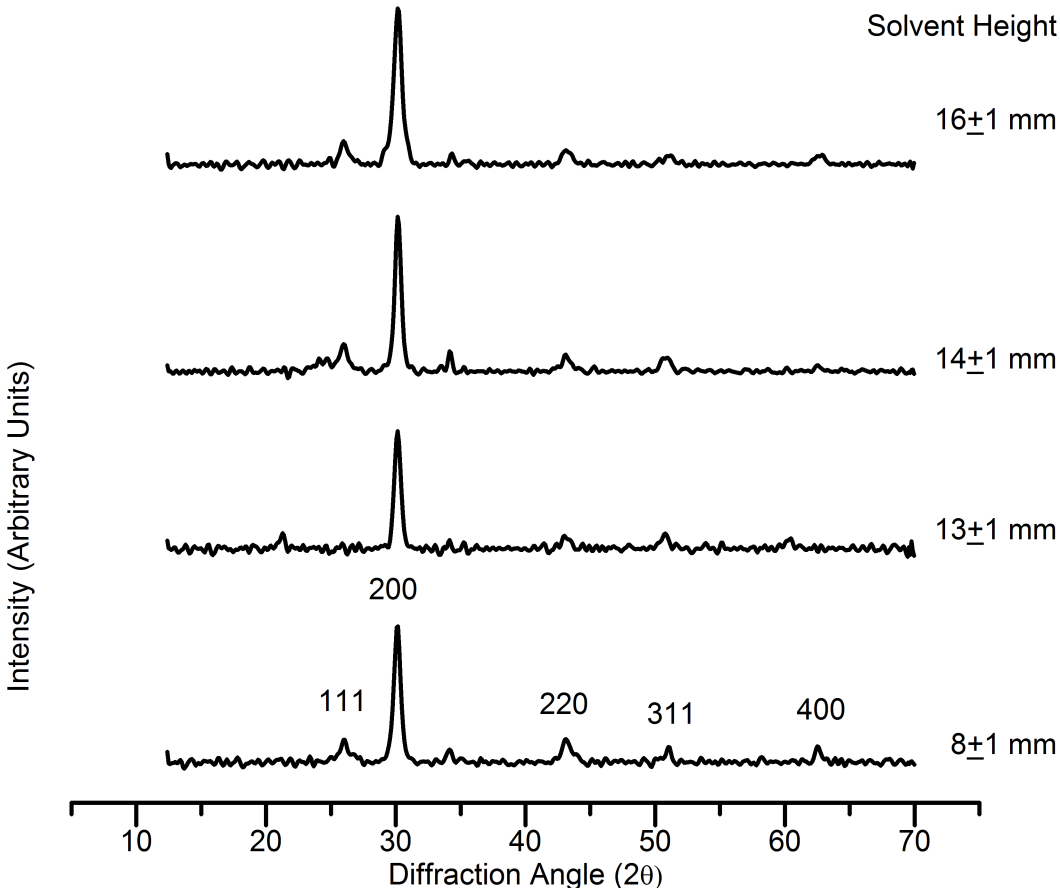

Figure 5.20: XRD of all samples synthesised using the purified lead thiobiuret precursor.

Table 3 shows the estimated crystallite diameters from the diffraction data shown in figure 5.20. As was seen with the samples synthesised using the unpurified precursor, the samples synthesised at the highest and lowest solvent heights exhibit the smallest average particle sizes, with the sample synthesised at the highest solvent height displaying the most uniform estimated crystallite sizes across all measured reflections.

	Miller Indices		
Solvent height	(111)	(200)	(220)
8±1 mm	8.3±0.8 nm	15.4±0.8 nm	10.3±1.0 nm
13±1 mm	-	16.0±0.8 nm	13.2±1.3 nm
14±1 mm	10.6±1.1 nm	16.3±0.8 nm	12.9±1.3 nm
16±1 mm	12.7±1.3 nm	12.4±0.6 nm	11.6±1.2 nm

Table 3: Table of minimum crystallite diameters calculated using the Scherrer equation[1].

5.3.2 X-ray photo-electron spectroscopy

XPS of the samples synthesised at 8 and 16 mm was carried out at beamline I311 at MAXLab synchrotron, Sweden. Samples were scanned within a week of synthesis at a similar range of photon energies to the samples synthesised using the unpurified precursor.

Figures 5.21 and 5.22 show depth profiling spectra for the lead 4f and sulfur 2p peaks of the samples synthesised at 16 mm and 8 mm solvent heights respectively. The differences between these samples are somewhat more pronounced than those synthesised using the unpurified precursor. In the sulfur 2p spectra of the sample synthesised at a solvent height of 8 mm there is a large proportion of neutral sulfur and a small amount of oxide; in contrast, the sample synthesised at a solvent height of 16 mm displays an almost pure sulfur 2p PbS doublet at all sampling depths. There is also a small amount of neutral lead present in the sample synthesised at a solvent height of 16 mm (indicated in figure 5.21) which was not previously seen in samples synthesised using the unpurified lead thiobiuret precursor. This was also present in the sample synthesised at 8 mm, but was too small to be fitted at the sampling depths shown. The presences of neutral lead can potentially be attributed to damage from the synchrotron beam. The reason for the presence of more oxidised sulfur in the sample synthesised at lower solvent height is unclear, as there is no indication of a large difference in particle size between these two samples from the XRD. The presence of large amounts of neutral sulfur, present only in the sample synthesised at lower solvent heights is potentially formed during aging, as this sample exhibits a greater degree of sulfur oxidation than that synthesised at the higher solvent height. The presence of neutral sulfur as an oxidation product has previously been reported in the literature occurring prior to formation of sulfoxy species[7,9].

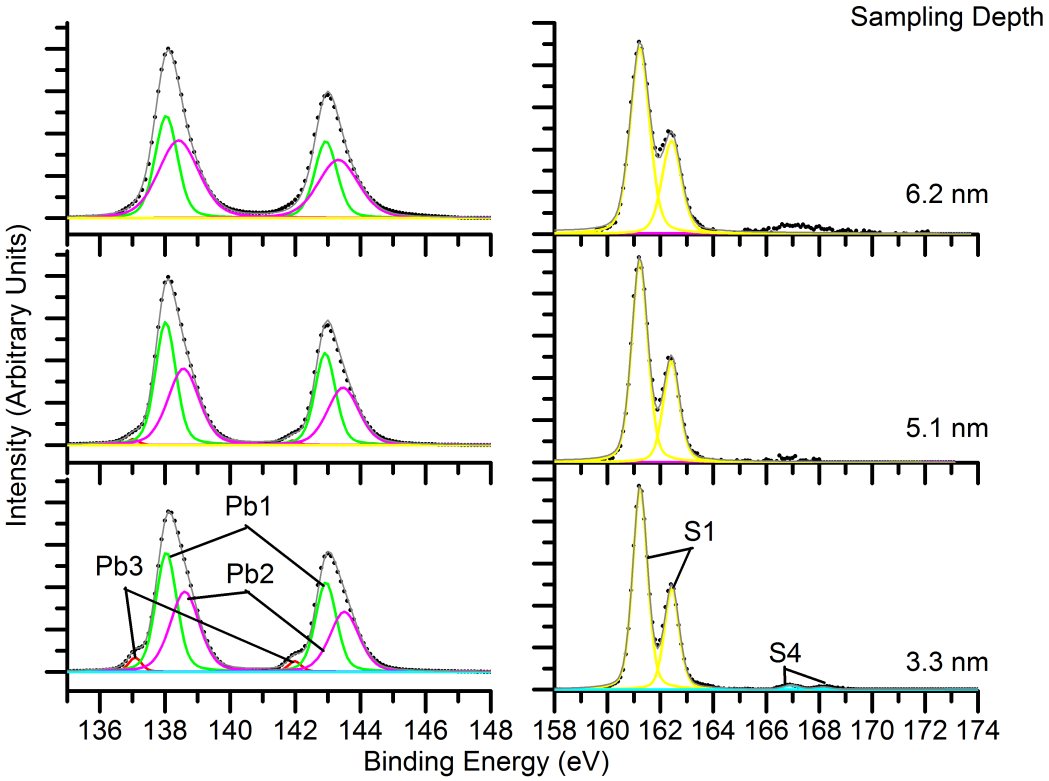

Figure 5.21: Depth profiling XPS spectra for the lead 4f and sulfur 2p peaks of the sample synthesised at 16 mm solvent height. Sampling depths from top to bottom correspond to photon energies of 1000, 800, and 500 eV respectively.

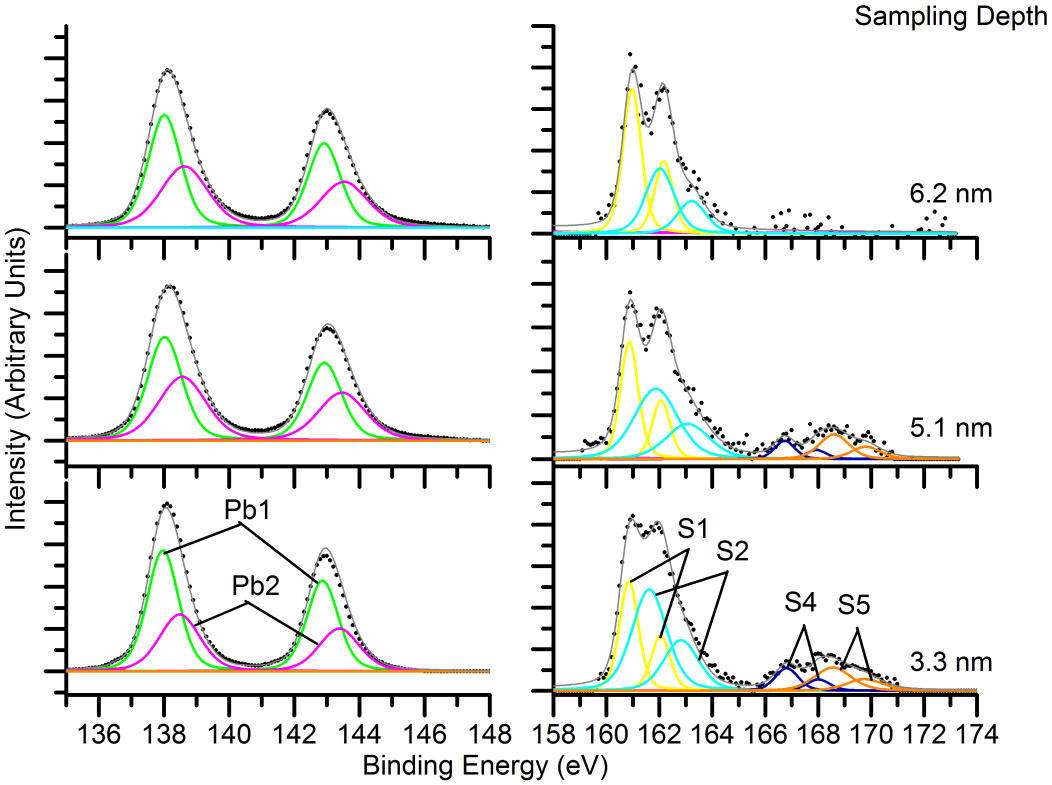

Figure 5.22: Depth profiling XPS spectra for the lead 4f and sulfur 2p peak of the sample synthesised at 8 mm solvent height. Sampling depths from top to bottom correspond to photon energies of 1000, 800, and 500 eV respectively.

Oxidised layer thickness calculations conducted for the sample synthesised at a solvent height of 8 mm (from the sulfur 2p PbS and $PbSO_n$ peaks) gave an estimated thickness of 0.49±0.10 nm at a sampling depth of 2.7 nm. This is significantly larger than the amount of oxide observed in samples synthesised using the unpurified precursor.

Table 4 shows the ratio of lead in lead sulfide to sulfur in lead sulfide in the samples as a function of sampling depth. As with the previous samples analysed, the lead to sulfur ratio increases with sampling depth. The average ratio of lead in lead sulfide to sulfur in lead sulfide however is much higher than in the samples synthesised using the unpurified precursor, particularly in the sample synthesised at 8 mm solvent height. This is due to the greater degree of lead oxidation observed in the samples synthesised with the unpurified precursor, along with the greater degress of sulfur oxidation seen in the sample synthesised using the purified precursor at a solvent height of 8 mm. The increased sulfur oxidation of this sample, relative to the sample synthesised at a solvent height of 16 mm which had a greater proportion of oxidised lead, potentially indicates the passivation of the surface by initial lead oxidation, delaying further oxidation. The reason for the difference in oxidation between the samples synthesised with the unpurified precursor compared to those synthesised with the purified precursor is unclear, and is complicated by the presence of the impurities in the samples synthesised with unpurified precursor, which may assist in passivation of the surface.

	Ratio of lead in PbS to sulfur in PbS at a sampling depth of:			
Solvent height	2.7 nm	3.3 nm	5.1 nm	6.2 nm
8±1 mm	2.3: 1	3.9 : 1	4.7 : 1	7.4
16±1 mm	-	1.5 : 1	2.6 : 1	2.8

Table 4: Table of the lead to sulfur ratios for both samples across multiple sampling depths.

5.4 Discussion and conclusions

Samples synthesised using the lead thiobiuret precursor typically displayed a minimum particle size on the order of ~10 nm, as shown by electron microscopy and x-ray diffraction. In both samples synthesised using unpurified and purified lead thiobiuret precursors, the minimum estimated particle sizes were observed for the samples synthesised at the highest and lowest solvent heights, with intermediate solvent heights producing particles with average estimated sizes of 15-20 nm.

Samples synthesised using an unpurified version of the precursor displayed a large amount of contamination in the x-ray diffraction patterns, and x-ray photoemission electron microscopy of these films showed localised areas of sodium present in the sample. It was inferred from this that the presence of sodium chloride in the precursor had no significant chemical effect on the formation of the films, but served to dilute the concentration of the precursor. There was little difference in oxidation observed across solvent heights of samples synthesised using the unpurified precursor, however samples synthesised using the purified precursor displayed a significant disparity, with far greater amounts of oxidation visible in the sample synthesised at a lower solvent height. This sample also exhibited a much lower degree of lead oxidation, indicating that the oxidised lead species may act to passivate the surface against further oxidation. Oxidised layer thickness calculations showed thicknesses of less than 0.1 nm on all samples synthesised using the unpurified precursor, and a thickness of 0.5 nm for the more oxidised of the samples synthesised using the purified precursor.

In all samples, an increase in lead to sulfur ratio was observed with increasing sampling depth within the XPS spectra. A higher lead to sulfur ratio in general was observed in samples synthesised using the purified precursor, indicating that the concentration of the lead precursor has an effect on the stoichiometry of the resulting film. Electron microscopy shows films of particles with a potentially fairly broad size dispersion and a strong tendency to form large agglomerates of particles.

References

(1) Patterson, A. *Physical Review* **1939**, *56*, 978-982.

(2) Delong Instruments Benchtop Low Voltage Electron Microscope http://www.lv-em.com/ (accessed Mar 28, 2012).

(3) Tanuma, S.; Powell, C. J.; Penn, D. R. *Surface and Interface Analysis* **1991**, *17*, 927-939.

(4) Hardman, S. J. O.; Graham, D. M.; Stubbs, S. K.; Spencer, B. F.; Seddon, E. A.; Fung, H.-T.; Gardonio, S.; Sirotti, F.; Silly, M. G.; Akhtar, J.; O'Brien, P.; Binks, D. J.; Flavell, W. R. *PCCP* **2011**, *13*, 20275-83.

(5) Yashina, L. V.; Zyubin, A. S.; Püttner, R.; Zyubina, T. S.; Neudachina, V. S.; Stojanov, P.; Riley, J.; Dedyulin, S. N.; Brzhezinskaya, M. M.; Shtanov, V. I. *Surface Science* **2011**, *605*, 473-482.

(6) Park, R. L. *Applications Of Surface Science* **1977**, *1*.

(7) Buckley, A. N.; Woods, R. *Applications of Surface Science* **1984**, *17*, 401-414.

(8) Shard, A. G. *The Journal of Physical Chemistry C* **2012**, *116*, 16806-16813.

(9) Nowak, P.; Socha, R. P. *Fizykochemiczne Problemy Mineralurgii* **2006**, *Vol. 40*, 134-148.

Chapter 6: Synthesis of PbS films using varied concentration ratios of lead diethyldithiocarbamate and sodium sulfide nonahydrate precursors

In order to explore the effect of changes in precursor concentration several samples were synthesised using 19±1 mm solvent heights using varying concentrations of lead DETC and sodium sulfide nonahydrate. Samples synthesised using concentrations of 2 mM lead precursor to 1 mM sulfide precursor; 1 mM lead precursor to 1 mM sulfide precursor; and 1mM lead precursor to 2mM sulfide precursor were characterised using X-ray diffraction, transmission electron microscopy, and x-ray photoelectron spectroscopy performed at the BACH beamline, Elettra synchrotron, Trieste, Italy.

6.1 XRD

XRD of samples synthesised at varying precursor concentrations are shown in figure 6.1.

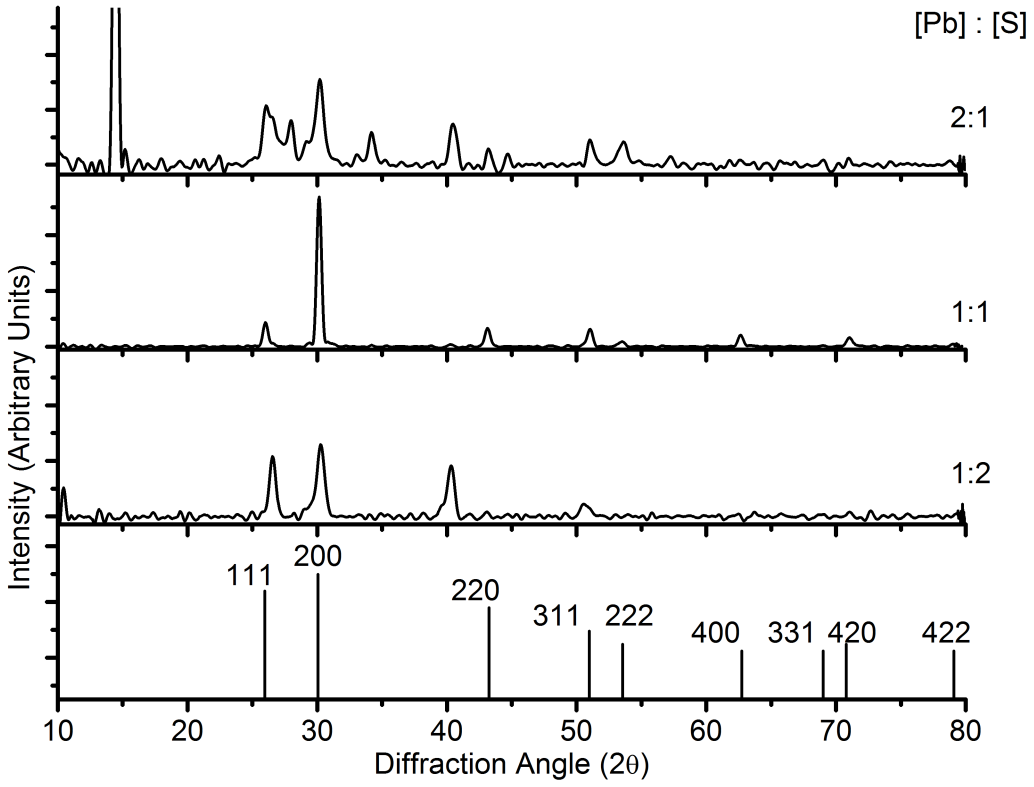

Figure 6.1: XRD of samples synthesised using lead diethyldithiocarbamate and sodium sulfide nonahydrate at varying concentrations. Concentrations are given on the right in mM. Standard lead sulfide XRD pattern is given as a reference.

Several additional peaks are present in the XRD of the sample synthesised using 2:1 concentrations of lead:sulfur precursors. The peak located at 15 degrees was determined to originate from the sample holder. However the peaks between 26-30° and at ~34° and ~40° originated from the sample itself. These peaks could not be attributed to any other expected product or contaminant, including lead sulfite, sulfate, or precursor. Due to the excess of lead precursor during synthesis of this sample, however, it seems likely that these peaks are due to fragments of the lead precursor being deposited with the film itself.

Estimates of minimum crystallite size were made using the Scherrer equation[1] for all quantifiable peaks. These estimates are shown in figure 6.2.

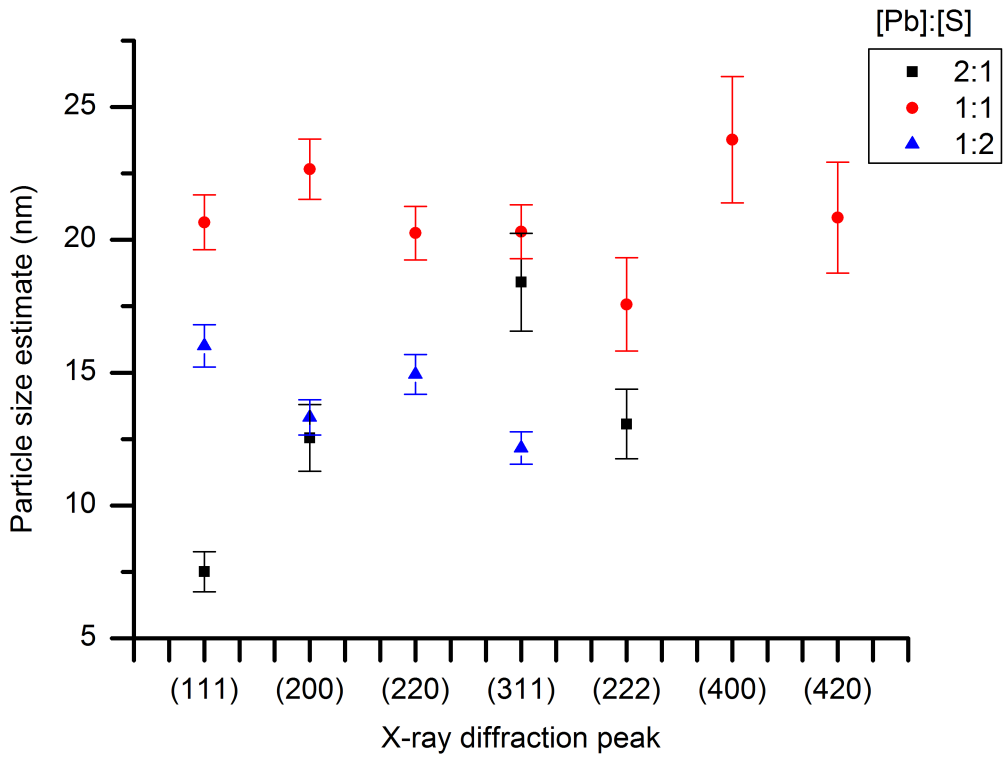

Figure 6.2: Graph of estimated minimum crystallite sizes calculated using the Scherrer equation[1] for each quantifiable diffraction peak in all samples.

The sample synthesised with stoichiometric precursor concentrations of 1 mM appears to exhibit the largest minimum crystallite size estimates of approximately 20 nm, with a relatively low variation between estimates calculated from different peaks. This sample also exhibits strong preferential orientation towards the (200) plane, which is not observed in either of the other two samples. The sample synthesised with a 1:2

lead:sulfur precursor ratio exhibited smaller size estimates of ~15 nm, again with only slight variation between different diffraction peaks. Estimates for the sample synthesised with a 2:1 lead:sulfur precursor ratio however exhibited a strong degree of variation, with estimates ranging from ~7.5 nm for the (111) peak to ~17.5 nm for the (311) peak. These results would indicate that a greater concentration of the lead precursor can lead to preferential growth along certain planes (resulting in particle size estimates that are larger for the corresponding diffraction peaks).

6.2 TEM

TEM of these films is shown in figures 6.3, 6.4, and 6.5, corresponding to the films synthesised with 2:1, 1:1, and 1:2 lead:sulfur precursor ratios respectively.

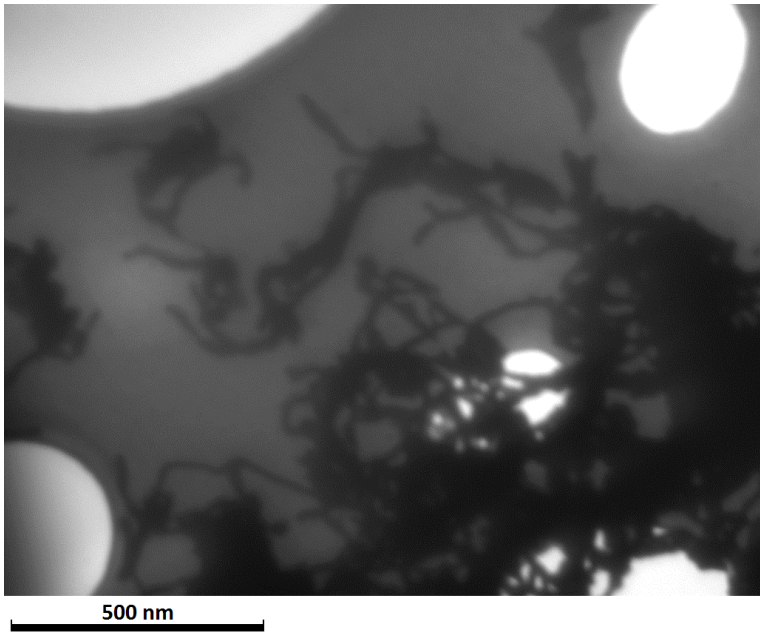

Figure 6.3: TEM image of the sample synthesised with a 2:1 lead:sulfur ratio.

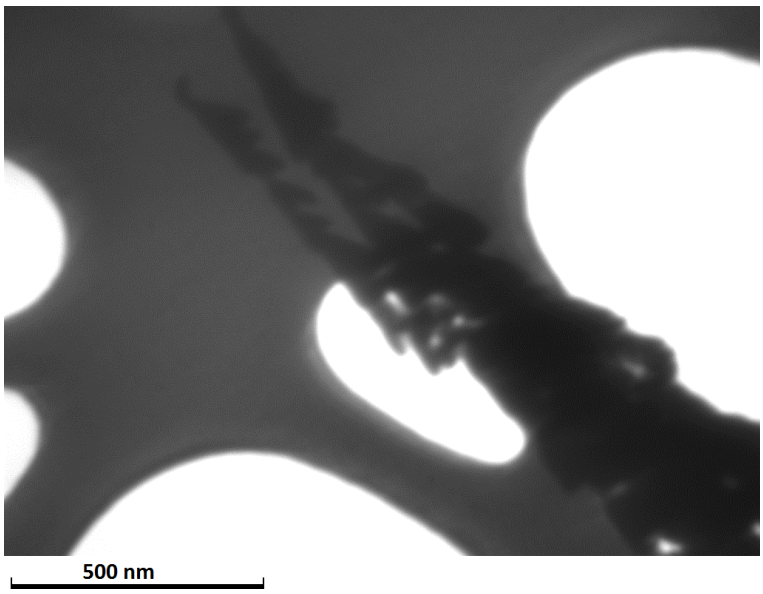

Figure 6.4: TEM image of the sample synthesised with a 1:1 lead:sulfur ratio.

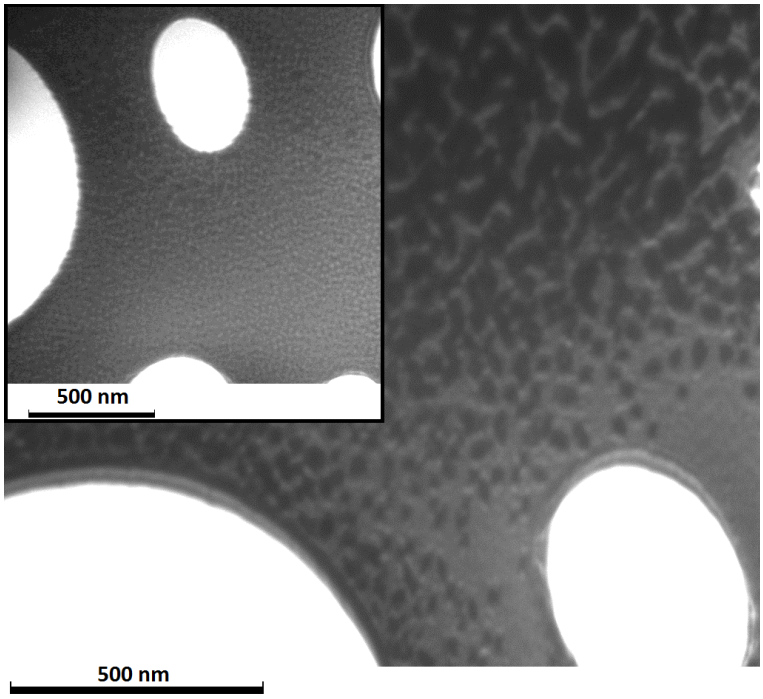

Figure 6.5: TEM image of the sample synthesised with a 1:2 lead:sulfur ratio. The inset displays a separate region of smaller particles.

There is a clear trend throughout the TEM of these samples. The sample synthesised with 2:1 lead:sulfur shows networks of long, thin 'stringlike' particles or particle agglomerates, forming large tangled masses; The sample synthesised with 1:1 lead:sulfur shows larger, more crystalline and angular particles but with a few longer particles and tree-like agglomerates visible in other areas within the sample. This is consistent with the narrow, intense XRD reflections seen for this sample. The sample synthesised with 1:2

lead:sulfur exhibits much more isotropic particles of varying size, from large agglomerates down to particles of 10 nm diameter and potentially less (albeit difficult to identify in the TEM images due to being too small). This indicates that the longer particles and agglomerates are preferentially formed in the presence of higher relative lead precursor concentrations. This implication is supported by the XRD results mentioned earlier which identified the greatest level of preferential growth in the particles synthesised with 2:1 lead:sulfur.

6.3 X-ray photo-electron spectroscopy

XPS of these samples was performed at beamline BACH, Elettra Synchrotron, Trieste, Italy. Samples were introduced in to vacuum within one week of synthesis. Figures 6.6, 6.7, and 6.8 show depth profiling spectra of the samples synthesised with 2:1, 1:1, and 1:2 lead:sulfur ratios respectively. Table 1 shows peak assignments with comparison to literature values. Figure 6.9 shows the ratios of lead to oxidised lead, sulfur to oxidised sulfur, lead in lead sulfide to sulfur in lead sulfide, and total lead to total sulfur for all three samples.

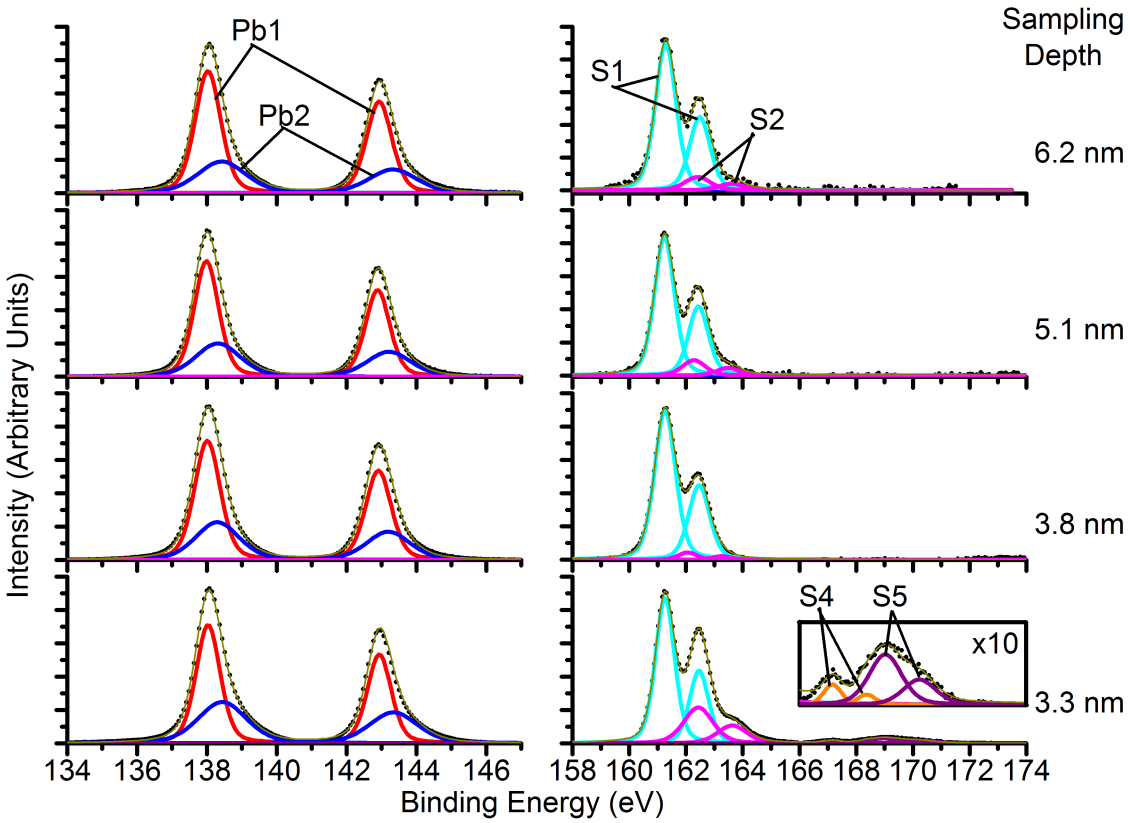

Figure 6.6: XPS spectra of the lead 4f and sulfur 2p regions as a function of sampling depth for the sample synthesised with a 2:1 lead:sulfur ratio. Sampling depths from top to bottom correspond to photon energies of 1000, 800, 580 and 500 eV respectively.

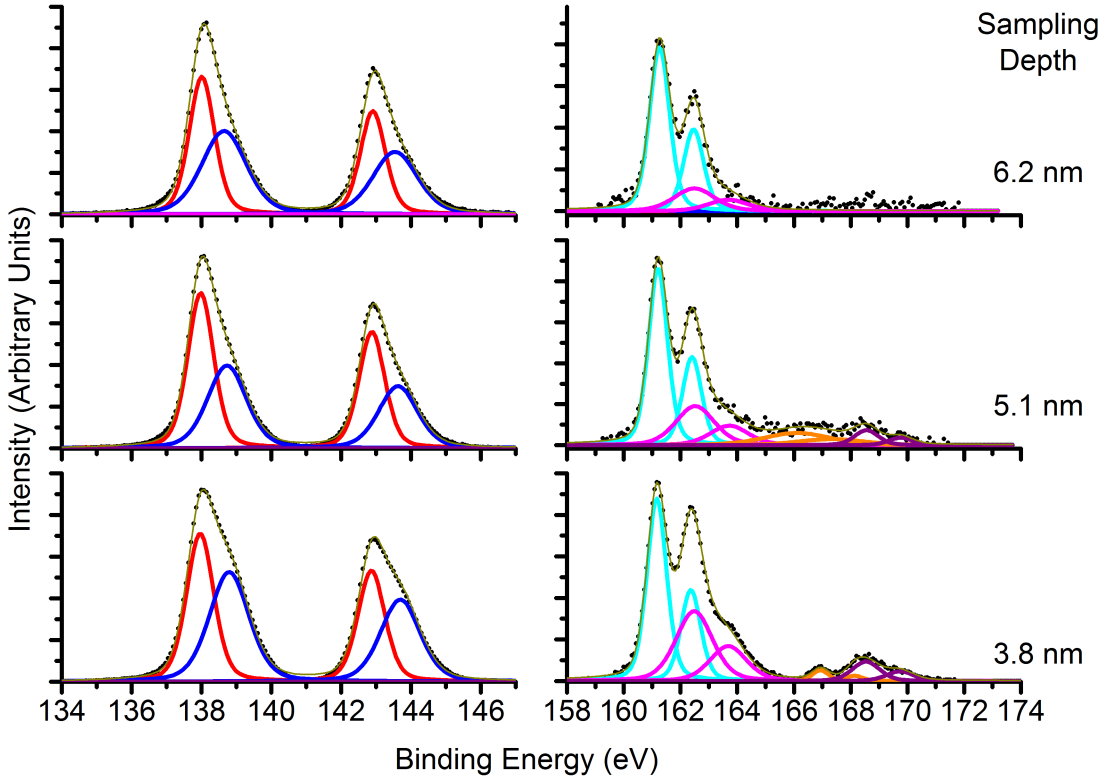

Figure 6.7: XPS spectra of the lead 4f and sulfur 2p regions as a function of sampling depth for the sample synthesised with a 1:1 lead:sulfur ratio. Sampling depths from top to bottom correspond to photon energies of 1000, 800, and 580 eV respectively.

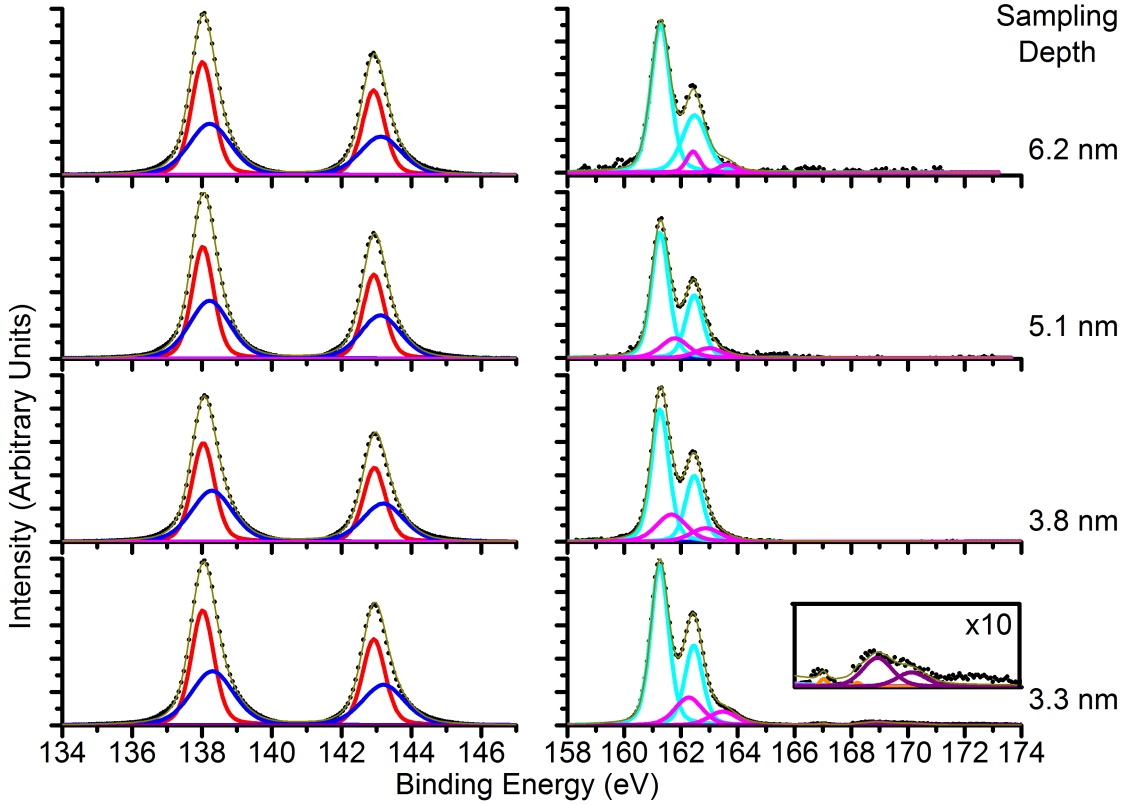

Figure 6.8: XPS spectra of the lead 4f and sulfur 2p regions as a function of sampling depth for the sample synthesised with a 1:2 lead:sulfur ratio. Sampling depths from top to bottom correspond to photon energies of 1000, 800, 580 and 500 eV respectively.

Peak label	Assignment	Literature Binding Energy (eV)	Observed Binding Energies (eV)	Observed FWHM (eV)
Pb1	Lead in PbS	138	138	~0.7-0.9
Pb2	Lead in PbSOx	139.1	~138.3-138.8	~1.3-1.7
S1	Sulfur in PbS	161.1	~161.2	~0.6-0.9
S2	Neutral sulfur	162	~162.2-162.5	~1.0-1.6
S3	Sulfur in $PbSO_n$	163-165	-	-
S4	Sulfur in $PbSO_3$	166.9	~166.9-167.1	~1.0-2.7
S5	Sulfur in $PbSO_4$	168.6	~168.5-169	~1.0-1.6

Table 1: Table of peak assignments. Spectra were aligned to the lead 4f PbS peak at 138 eV on the binding energy scale[2,3].

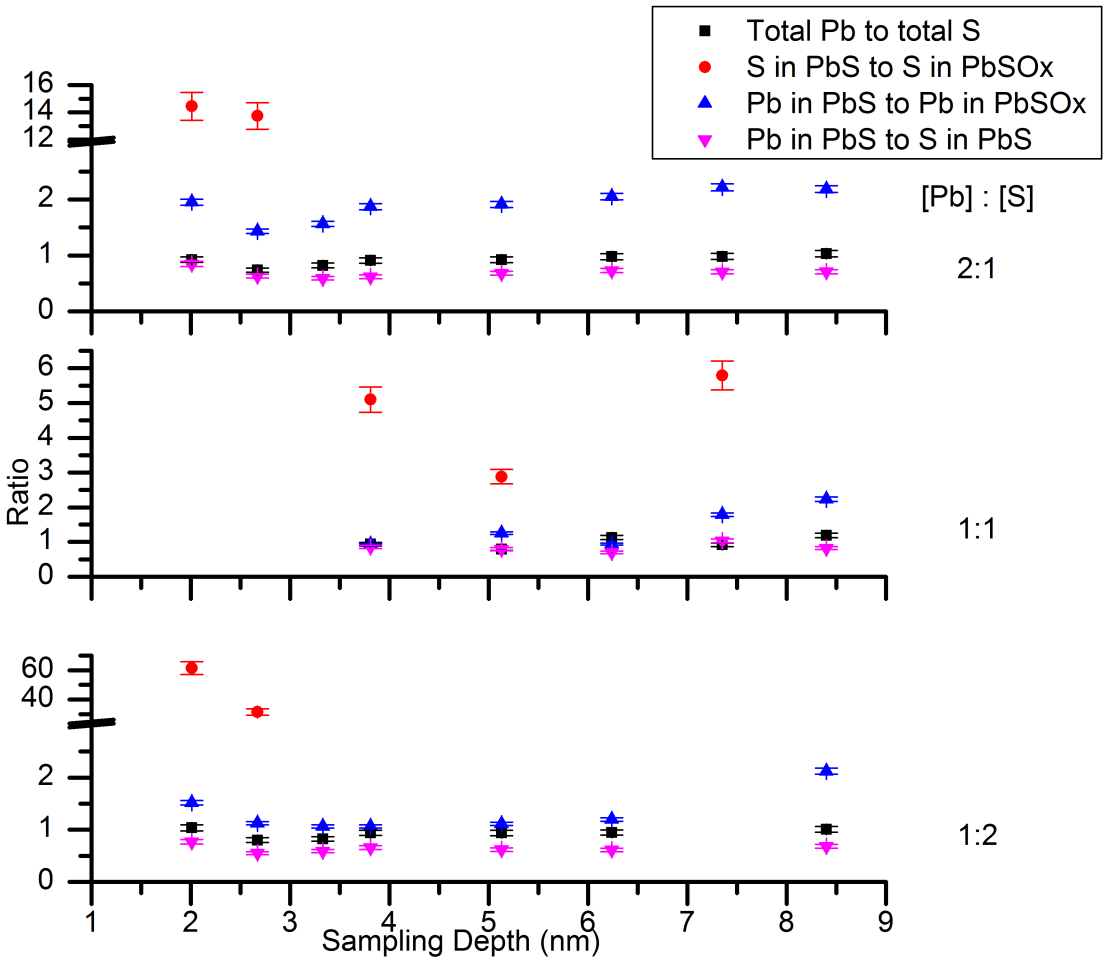

Figure 6.9: Ratios of lead in PbS to oxidised lead; sulfur in PbS to oxidised sulfur; lead in PbS to sulfur in PbS and total lead to total sulfur as a function of sampling depth for all three samples.

All samples display extremely low levels of sulfur oxidation which is localised to the surface of the sample. A larger amount of oxidised lead is seen throughout all sampling depths of all samples, with a slightly larger amount observed at the lowest sampling depths. This disparity indicates that lead is oxidised more rapidly than the sulfur during initial aging. A significant amount of neutral sulfur is also seen throughout all samples, with a slight increase towards the surface of the particle, potentially indicating decomposition on reaction with air of lead sulfide into oxidised lead and neutral sulfur. The largest relative amount of oxidised and neutral sulfur are observed in the sample synthesised with 1:1 lead:sulfur. This suggests that some characteristic of the film results in an increased propensity to sulfur oxidation; this is potentially related to the morphology, as this sample displayed a significantly different XRD pattern to the samples synthesised with non-stoichiometric precursor concentrations.

6.4 Absorption spectroscopy

The optical absorption of the films was measured using a Perkin-Elmer Lambda 1050 UV-Vis-NIR spectrometer. Figures 6.10, 6.11, and 6.12 show absorption spectra of the samples synthesised with 2:1, 1:1, and 1:2 lead:sulfur ratios respectively. Figure 6.13 shows absorption spectra of various lead sulfide thin films taken from the literature as a reference. Figure 6.14 shows a plot of particle size against the energy of the resulting absorption features, taken from Cademartiri *et al.* for purposes of estimating the required particle size to produce any features observed.

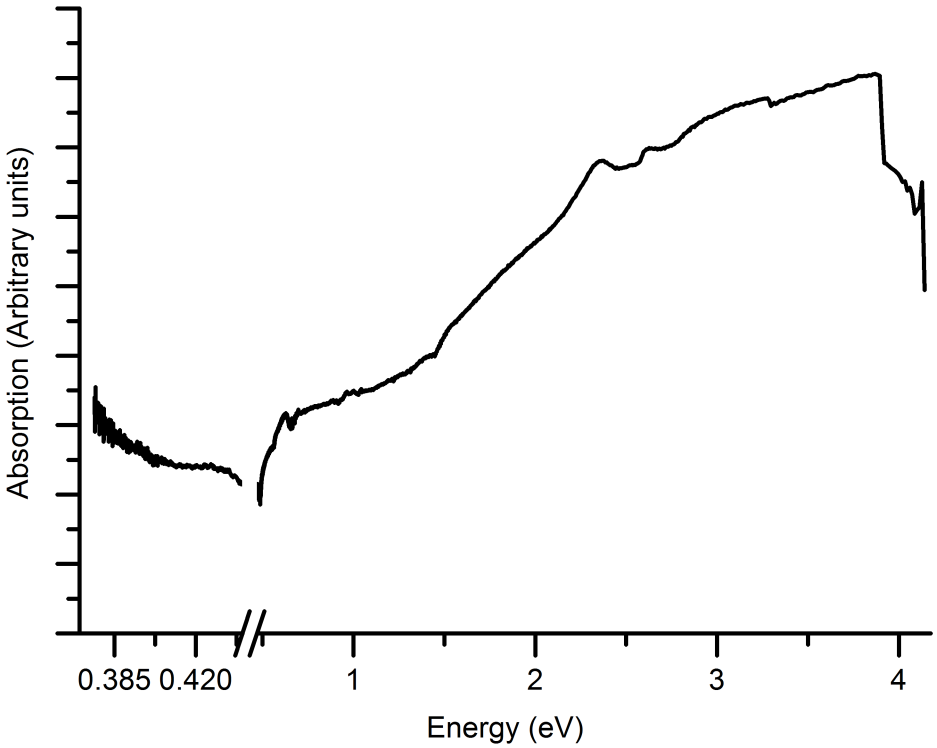

Figure 6.10: Absorption spectrum of the sample synthesised with 2:1 lead:sulfur.

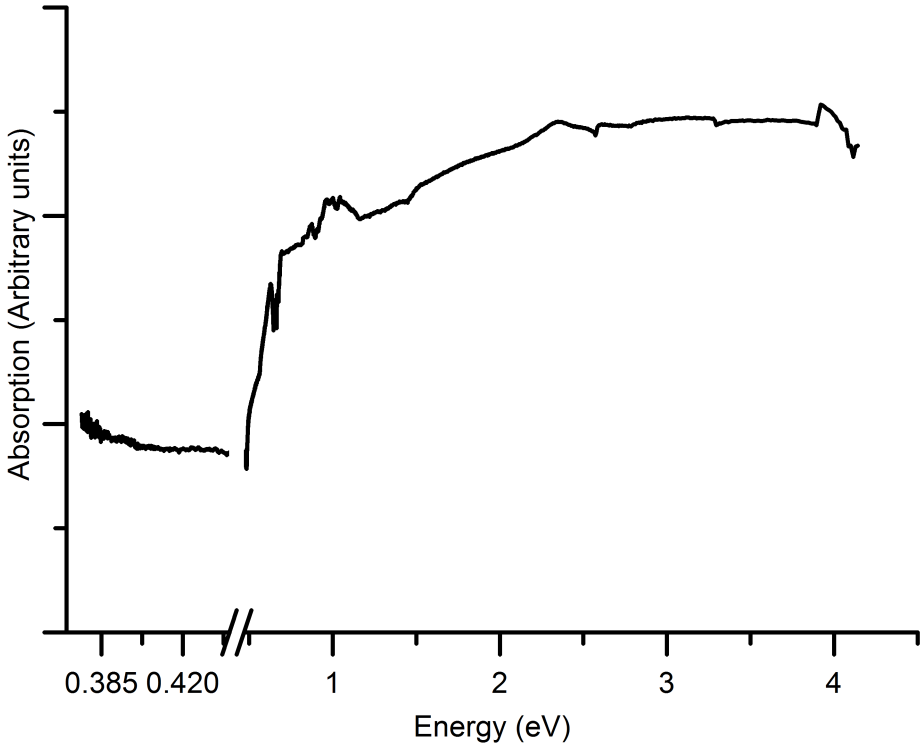

Figure 6.11: Absorption spectrum of the sample synthesised with 1:1 lead:sulfur.

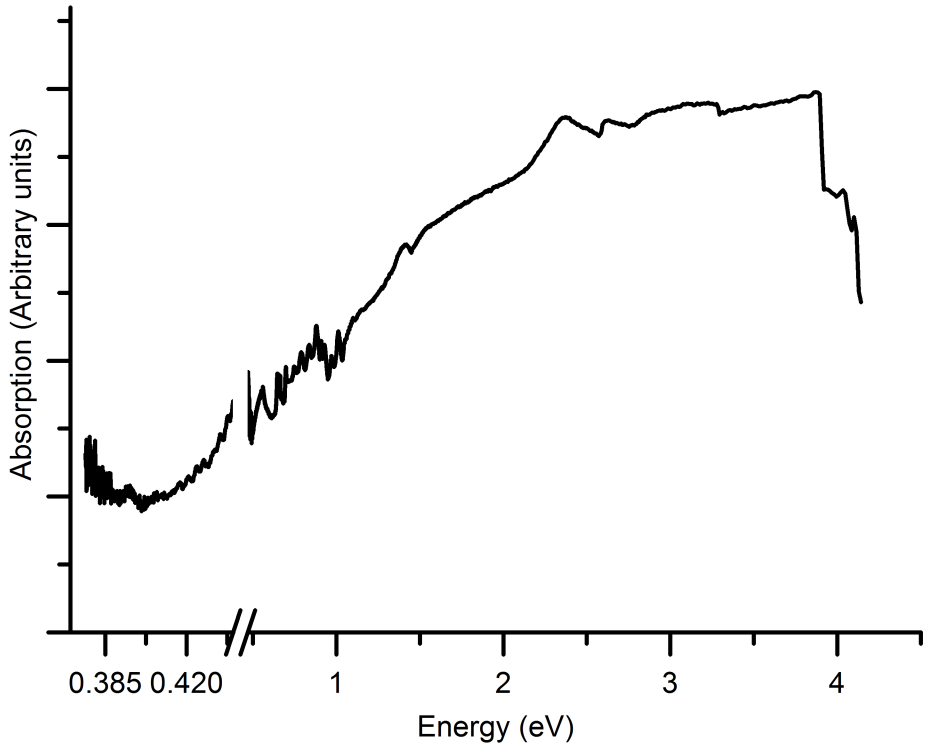

Figure 6.12: Absorption spectrum of the sample synthesised with 1:2 lead:sulfur.

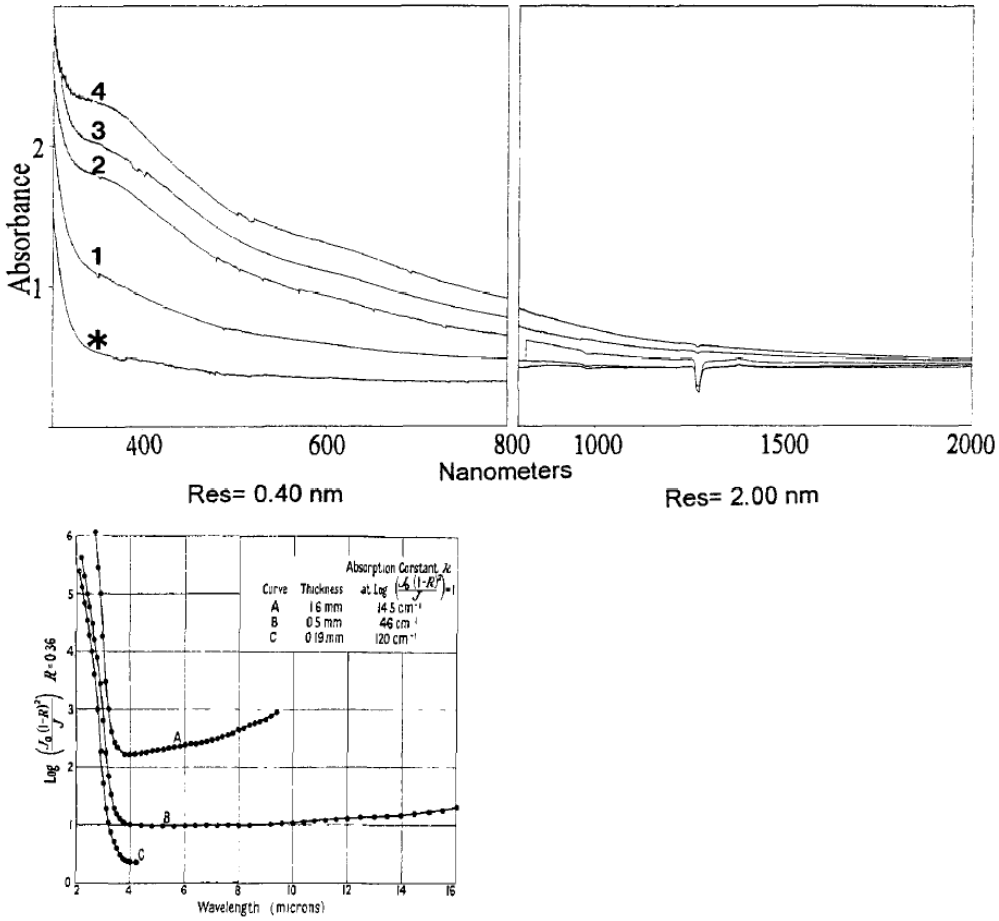

Figure 6.13: Absorption spectra of various thicknesses of lead sulfide film provided for reference, at photon wavelengths of 300 - 2000 nm[7] (top, corresponding to 4.13 - 0.62 eV) and 2000 - 16000 nm[8] (bottom, corresponding to 0.62 - 0.08 eV).

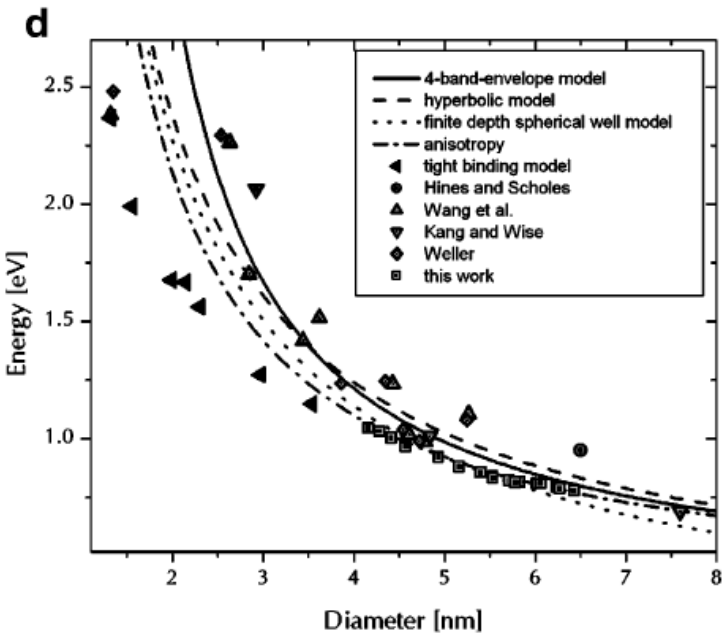

Figure 6.14: Plot of the the energy of absorption features as a function of particle diameter, taken from multiple sources[6].

Samples were deposited on glass slides, and then mounted upon a larger glass slide in order to take absorption spectra, and the absorption spectrum of the large glass slide was subtracted in order to obtain the spectra of the samples. As such, there are minor anomalies present in the spectra caused by the imperfect removal of the glass spectrum. Notably, the sharp drop off at high photon energies is a result of a the large increase in absorption of the glass at high energies (~4 eV). The break in the x-axis is to remove a small region between 0.44 and 0.47 eV in which the background absorption saturated the detector. A slightly wider scale is used below the break to provide greater detail in the area where the bulk band-gap of lead sulfide would be expected to produce a feature (~0.41 eV). No significant absorption feature is seen in this precise region, however all samples display an increase in absorption at slightly above this energy. This rise is gradual in the sample synthesised with a 1:2 lead:sulfur ratio, however in the samples synthesised with a 2:1 and 1:1 lead:sulfur ratio there is also a sharp rise at ~0.5 eV, which is sharpest in the sample synthesised with a 1:1 lead:sulfur ratio. This is consistent with the spectra shown in figure 6.13 for bulk lead sulfide thin films. The fact that this rise is greatest for the sample synthesised with a 1:1 lead:sulfur ratio is consistent with the particle size estimates for XRD which indicate that this sample exhibits the largest particles. In all samples there is a feature observed at a photon energy of approximately 2.35 eV that is not observed in the background spectrum originating from the glass.

Another local maximum in absorption occurs around 0.9-1 eV in all samples, although it is barely visible in the sample synthesised using 2:1 lead:sulfur, and most visible in the sample synthesised at 1:1 lead:sulfur. The cause of these features is unknown.

6.5 Summary and conclusions

All samples exhibited similar estimated minimum crystallite sizes from XRD, ranging from 10-20 nm. The sample synthesised with a 2:1 lead:sulfur ratio exhibited both the smallest estimated minimum crystallite size of ~7.5 nm from the (111) diffraction peak, and the largest variation in estimated minimum crystallite size across different diffraction peaks, indicating strong anisotropy in the the growth of crystallites. The sample synthesised with a 1:1 lead:sulfur ratio exhibited both the largest estimated minimum crystallite sizes, as well as the least variation across diffraction peaks. This was supported by TEM images of the samples, which showed long, string-like growths and agglomerations present in the 2:1 lead:sulfur ratio sample, and the most spherical, isotropic particles and agglomerates in the 1:2 sample.

XPS of these samples displayed a moderate level of lead oxidation throughout all samples, without a corresponding amount of oxidised sulfur. This indicates that oxidation of the samples is non-congruent; there is a process of degradation in which the lead is oxidised separately to the sulfur. The presence of small amounts of neutral sulfur throughout the sample, and in larger amounts closer to the surface, suggests that the degradation process begins with decomposition of lead sulfide into neutral sulfur and oxidised lead species, potentially in the form of lead hydroxide as has been reported in the literature[4,5]. This is supported by the fact that the 1:1 lead:sulfur sample has both the largest relative amount of oxidised lead and the largest relative amount of neutral sulfur, indicating that these two quantities are correlated. Small amounts of lead sulfate and sulfite were observed in all samples, however unlike the oxidised lead species observed, these were extremely localised to the surface.

References

(1) Patterson, A. *Physical Review* **1939**, *56*, 978-982.

(2) Park, R. L. *Applications Of Surface Science* **1977**, *1*.

(3) Hardman, S. J. O.; Graham, D. M.; Stubbs, S. K.; Spencer, B. F.; Seddon, E. A.; Fung, H.-T.; Gardonio, S.; Sirotti, F.; Silly, M. G.; Akhtar, J.; O'Brien, P.; Binks, D. J.; Flavell, W. R. *Physical chemistry chemical physics : PCCP* **2011**, *13*, 20275-83.

(4) Buckley, A. N.; Woods, R. *Applications of Surface Science* **1984**, *17*, 401-414.

(5) Nowak, P.; Socha, R. P. *Fizykochemiczne Problemy Mineralurgii* **2006**, *Vol. 40*, 134-148.

(6) Cademartiri, L.; Montanari, E.; Calestani, G.; Migliori, A.; Guagliardi, A.; Ozin, G. a. *Journal of the American Chemical Society* **2006**, *128*, 10337-10346.

(7) Najdoski, M.; Minceva-Sukarova, B.; Drake, A.; Grozdanov, I.; Chunnilall, C. J. *Journal of Molecular Structure* **1995**, *349*, 85-88.

(8) Gibson, A. F. *Proceedings of the Physical Society. Section B* **1952**, *65*, 378-388.

Chapter 7: Experiments with different thiocarbamate precursors

7.1 Introduction

Syntheses of lead sulfide nanoparticle films were carried out using lead thiocarbamate precursors with different sizes of organic complex in order to investigate the effect of precursor size on the synthesis product. As well as the syntheses described previously using lead diethyldithiocarbamate (DETC), films were synthesised using lead dibutyldithiocarbamate (DBTC) and lead dipentyldithiocarbamate (DPTC). The resultant films were characterised using XRD, TEM, and XPS. Initial samples synthesised using the lead DBTC precursor at solvent heights of 19±1 mm and 25±1 mm were also characterised using SEM.

DETC, DBTC and DPTC precursors used in the synthesis of samples for characterisation *via* XRD, TEM, and XPS were provided by Edward Lewis of the School of Chemistry, University of Manchester, UK. Unless otherwise noted, syntheses were carried out using 2 mM concentrations of both lead and sulfur precursors at a solvent height of 19±1 mm and a temperature of 50 °C for 2 hours.

7.2 X-ray Diffraction

XRD of samples synthesised with all three thiocarbamate precursors are presented in figure 7.1.

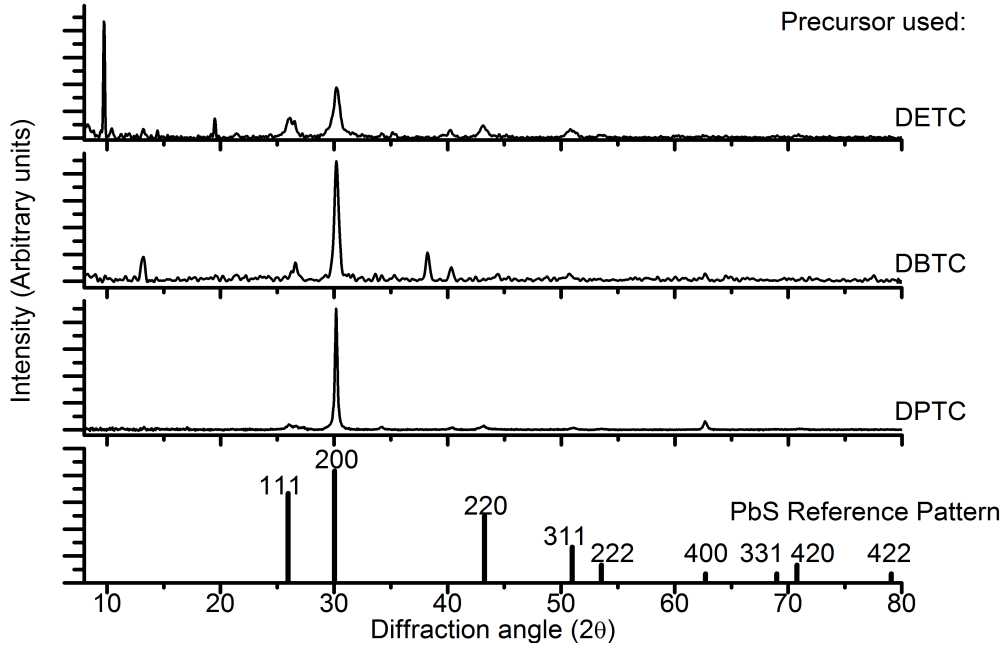

Figure 7.1: XRD of samples synthesised using three different forms of lead thiocarbamate precursor alongside a lead sulfide reference pattern[6].

The patterns observed show a clear trend with increasing precursor size of increasing crystallinity - the DPTC has the strongest lead sulfide peaks, indicating the greatest crystallinity, while the DETC has the weakest. A similar trend can be seen in the preferential orientation of the particles, as the relative size of the (200) reflection increases significantly with increasing precursor size. Several unidentified peaks occur in the diffraction patterns, at angles of ~13°, 15°, 38°, and 40° of which the only peak present in all of them is the one located at 40°. These peaks could not be assigned to any expected contaminant, including any possible oxidation products, sodium sulfide, or the precursors themselves. It is possible that these peaks arise from decomposition products of the thiocarbamate precursors, for which no XRD pattern is available for comparison.

Estimated particle sizes calculated using the Scherrer equation[1] from peak widths are shown in figure 7.2.

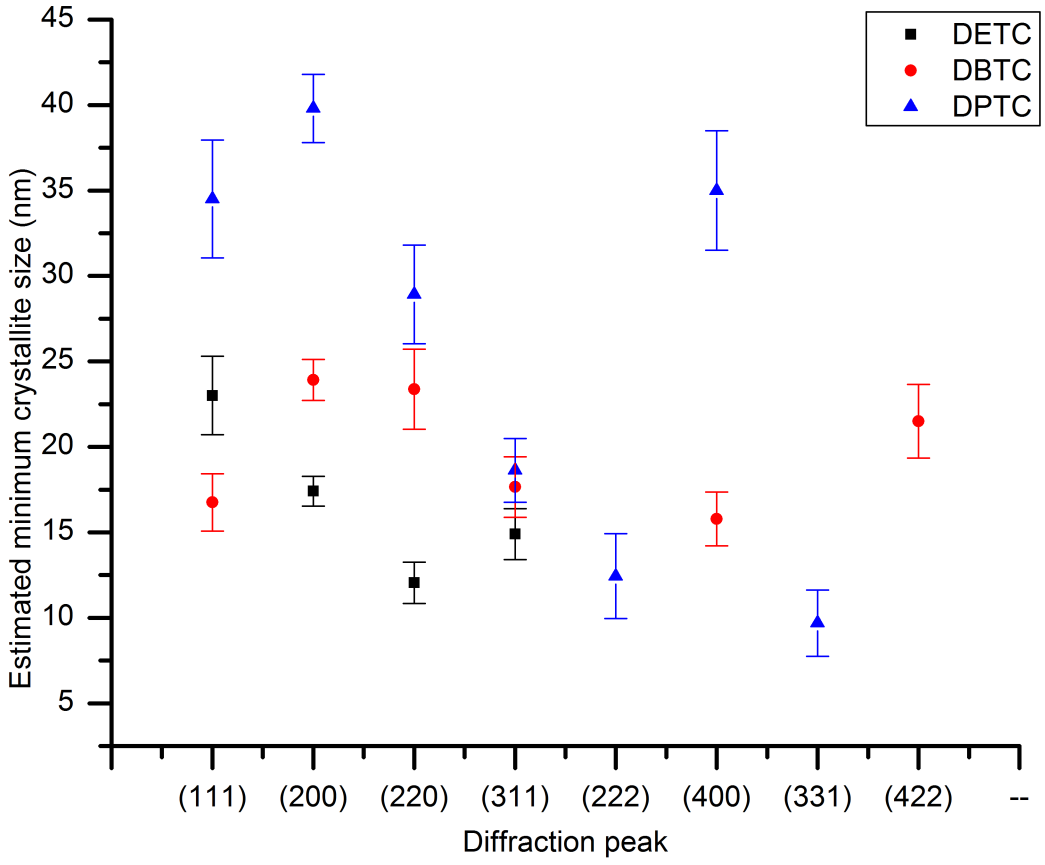

Figure 7.2: Estimates of minimum crystallite size from Scherrer calculations[1] for all samples.

The sample synthesised using the DPTC precursor shows the greatest level of preferential growth, with the largest variation of estimated particle size between different diffraction peaks. The (200) and (400) planes of this sample exhibit the highest estimated particle size of ≥35 nm. The other two samples diplay approximately similar estimated particle sizes of between 10-25 nm depending on diffraction peak, with the lower average size observed in the sample synthesised using DETC.

7.3 Electron Microscopy

Experiments with alternative thiocarbamate precursors began with synthesis of PbS films using lead DBTC precursor at solvent heights of 19±1 and 25±1 mm with a precursor concentration of 2 mM. SEM images of these films are shown in figures 7.3 and 7.4.

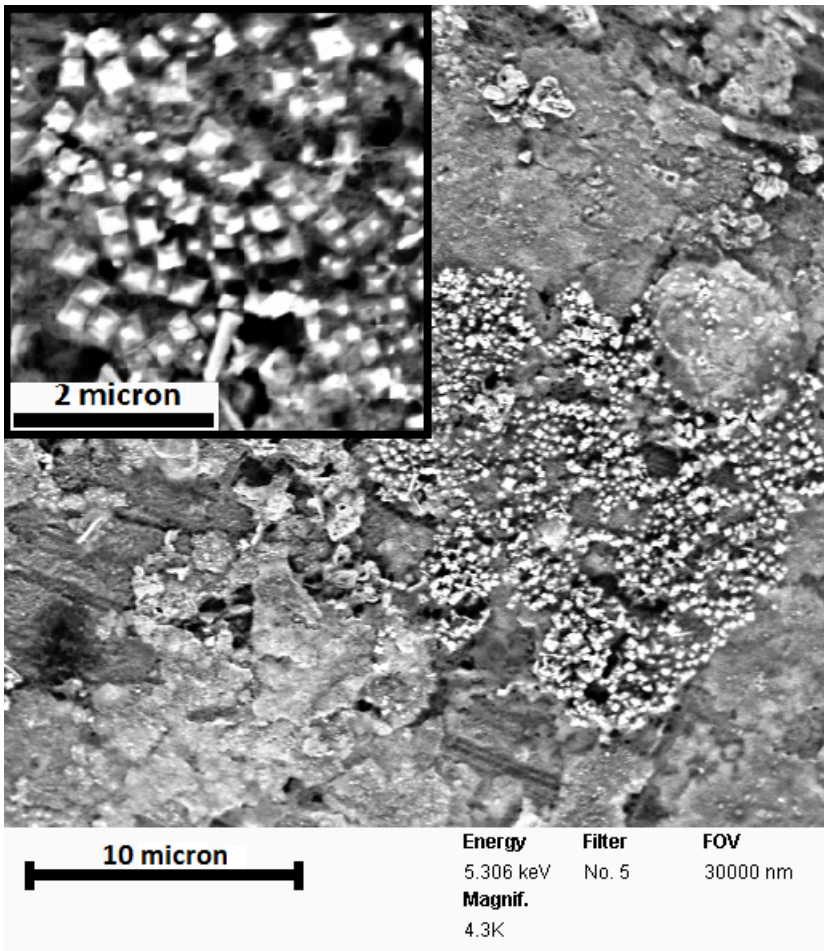

Figure 7.3: SEM image of a film synthesised using DBTC precursor at a solvent height of 19±1 mm. The inset shows a separate region at higher zoom.

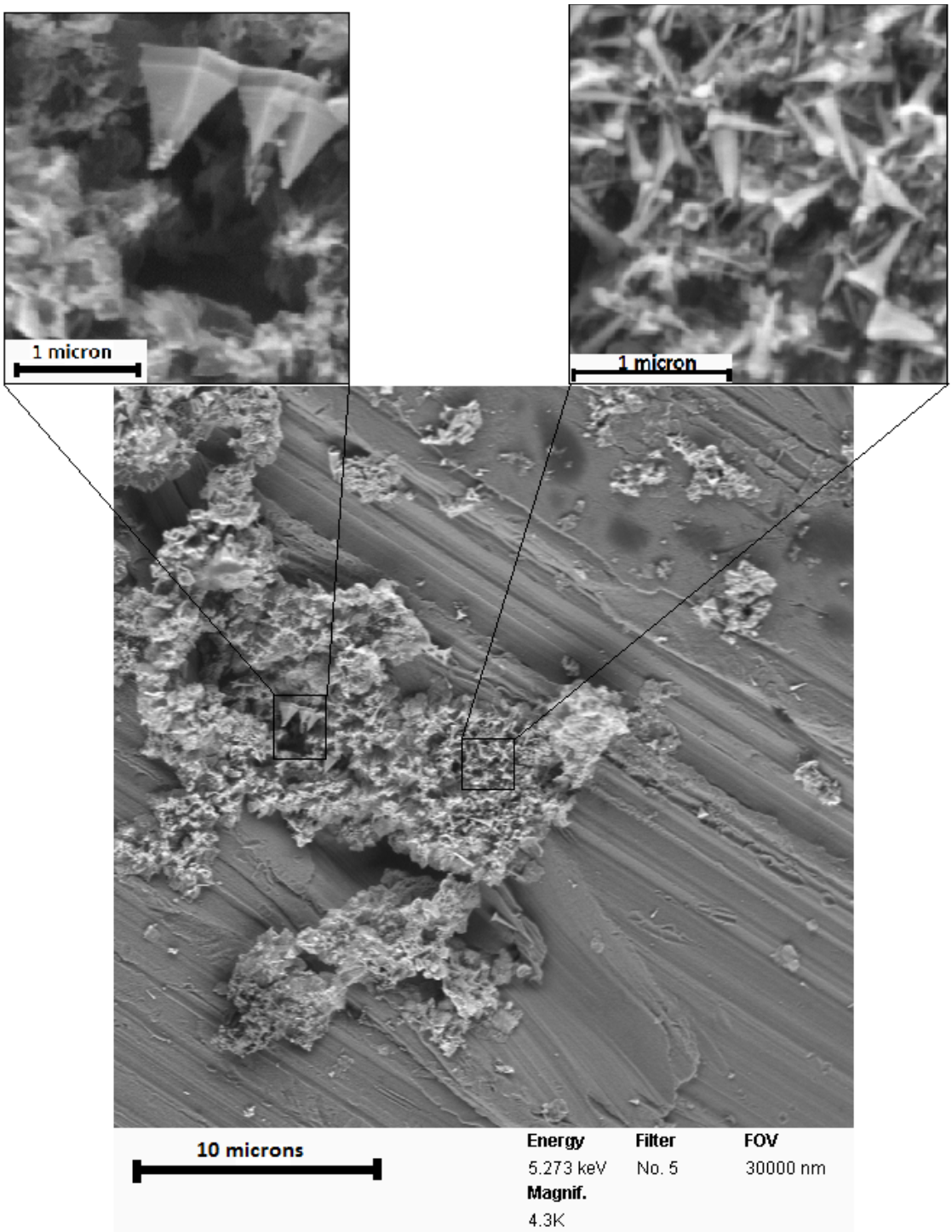

Figure 7.4: SEM image of a film synthesised using DBTC precursor at a solvent height of 25±1 mm. Images at the top show highlighted regions at greater zoom.

Both of the samples contained a background film of particles which appeared to be smaller than the SEM could resolve, as well of several patches of large structures. In the film synthesised at 19 mm solvent height (figure 7.3) the majority of these large particles are pyramids on the order of ~0.5 micron in size, adopting similar orientations. The film

synthesised at a solvent height of 25 mm (figure 7.4) also contains a small number of similar pyramidal crystals, however the majority of this film consists of higher-aspect ratio particles, including rods and conical particles. These appear to form the 'seeds' from which the pyramids form, with several of them appearing to have the beginnings of a pyramid-like structure forming at one end. This is very similar to previous work reported using this synthesis method by D. Fan *et al.*[2] in which small string-like particles were observed on the caps of pyramidal structures.

Figures 7.5, 7.6, and 7.7 show TEM of samples synthesised using DETC, DBTC, and DPTC precursors respectively.

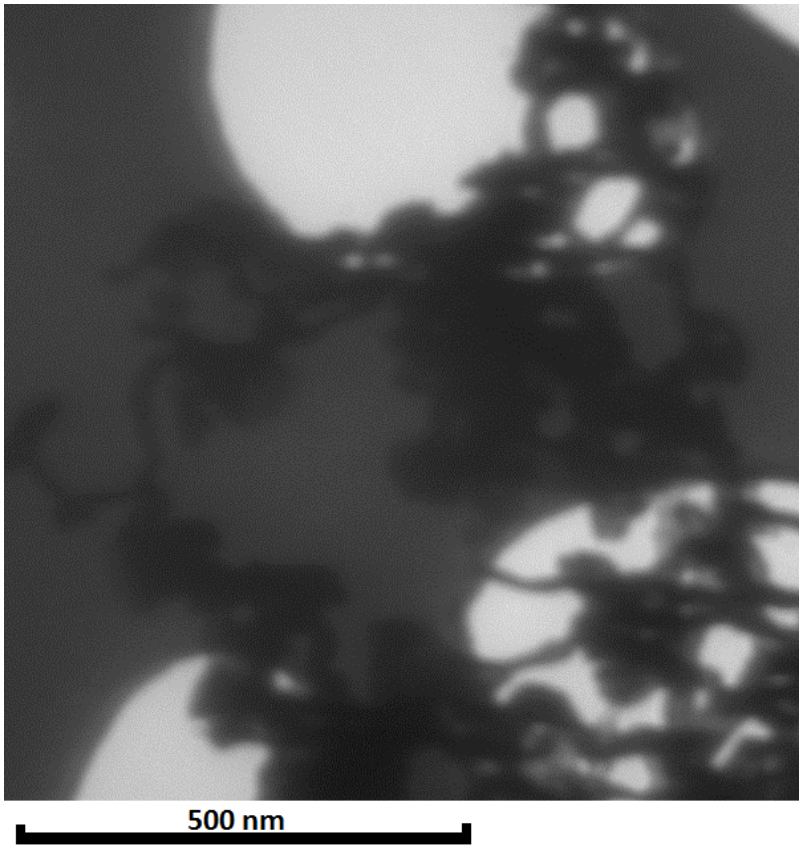

Figure 7.5: TEM image of a sample synthesised using lead DETC precursor.

TEM of the sample synthesised using the lead DETC precursor showed agglomerates of string-like particles, similar to those seen in previous samples synthesised using high concentrations of this precursor. The sample synthesised using lead DBTC precursor showed similar agglomerates, but with a larger proportion being transparent to the TEM

beam, indicating a much thinner film had been formed. There was also a greater proportion of individual visible particles throughout the sample.

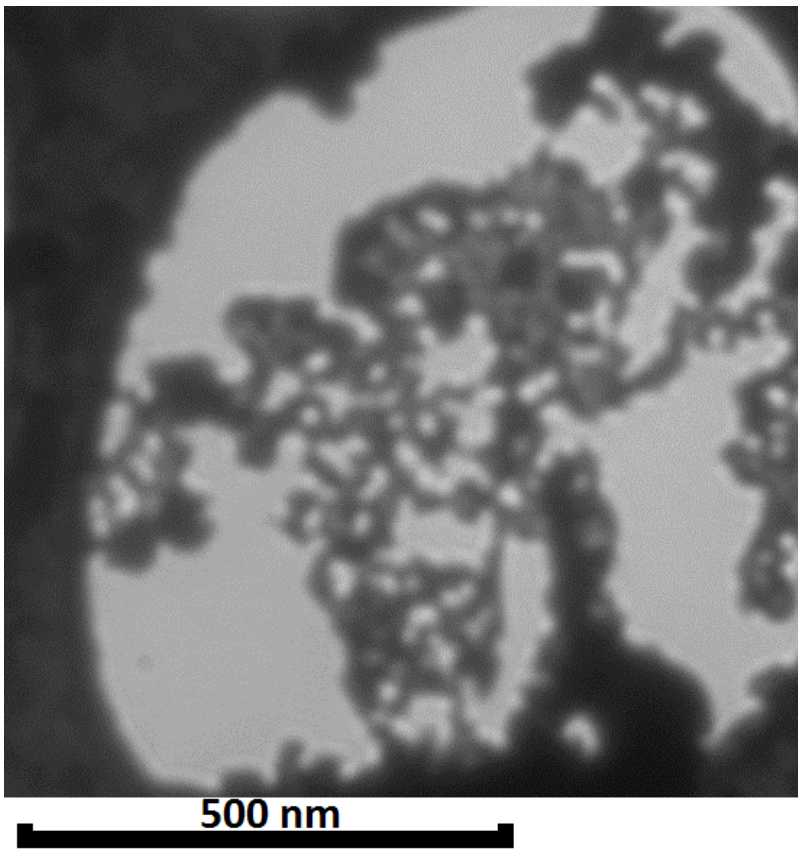

Figure 7.6: TEM image of a sample synthesised using lead DBTC

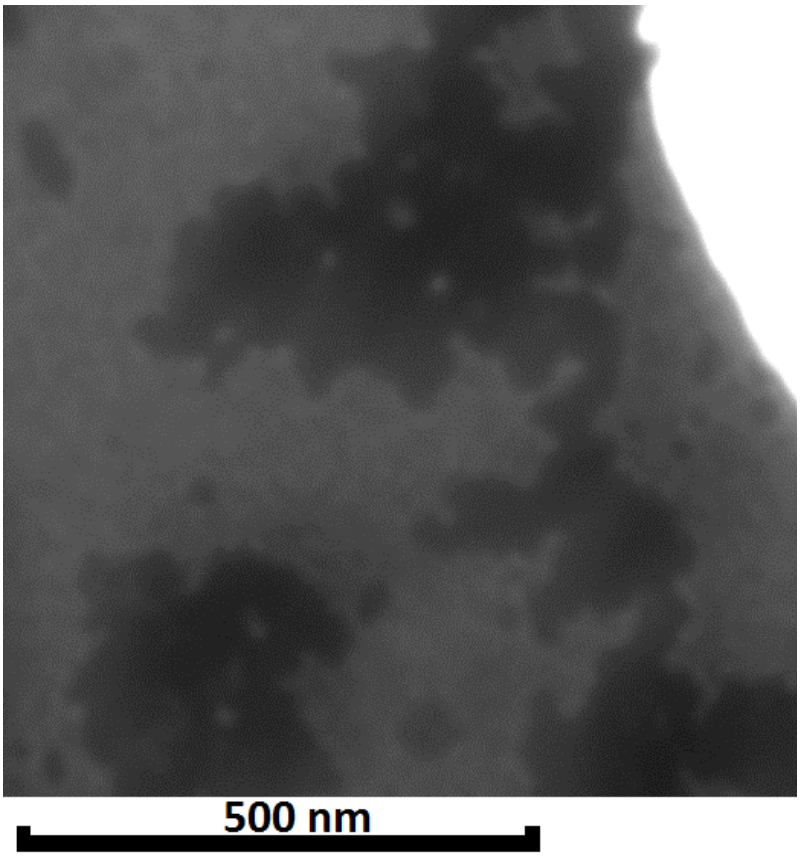

Figure 7.7: TEM image of a sample synthesised using lead DPTC precursor.

The sample synthesised using lead DPTC precusor showed agglomerates of particles of a more rounded nature than those seen in the two other precursors, with fewer individual particles than seen in the sample synthesised using the lead DBTC precursor.

7.4 X-ray photo-electron spectroscopy

XPS was performed on a lab-based XPS kit in the Photon Science Institute at the University of Manchester, UK. Figure 7.8 shows XPS spectra of the samples taken at a photon energy of 1486 eV, corresponding to a sampling depth of 8.8 nm. All samples were exposed to air for ~ 3 weeks and introduced to vacuum simultaneously.

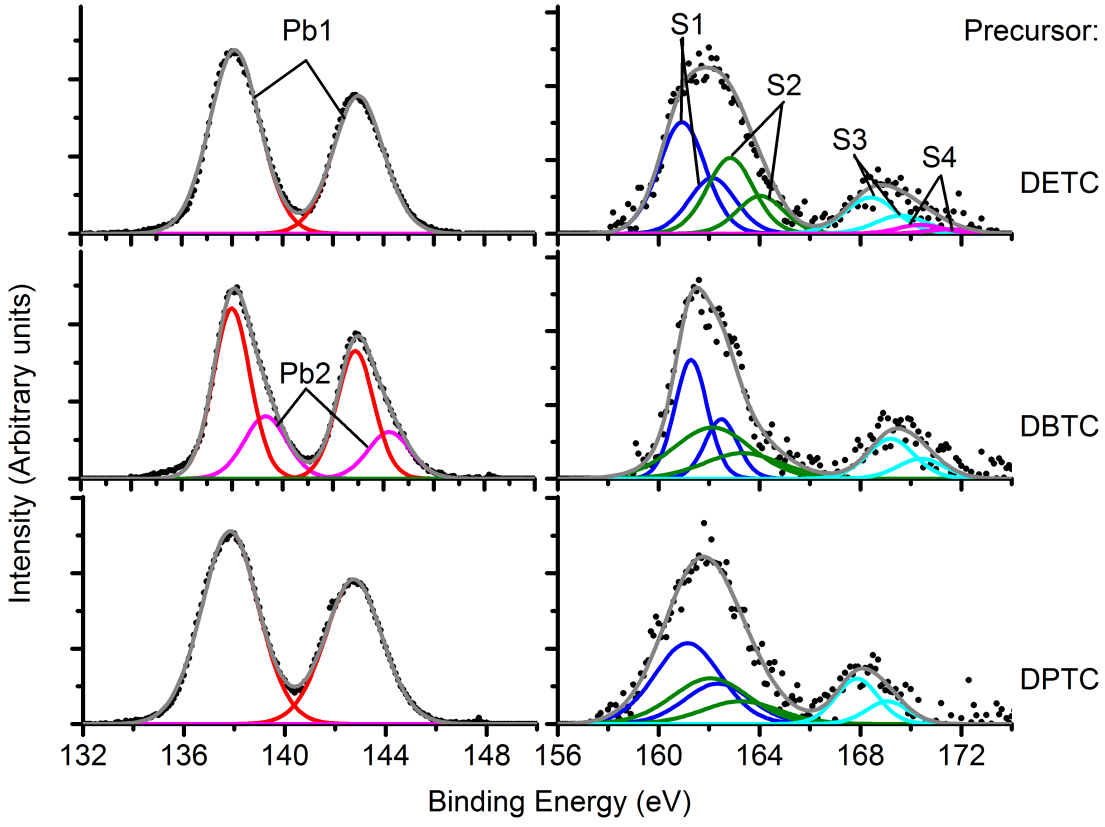

Figure 7.8: XPS of lead 4f and sulfur 2p regions for samples synthesised using all three precursors. Energies were normalised to the PbS lead 4f peak at 138.0 eV[3].

Peak label	Assignment	Literature Binding Energy (eV)	Observed Binding Energies (eV)	Observed FWHM (eV)
Pb1	Lead in PbS	138	Assigned as 138	~1.7-2.4
Pb2	Oxidised lead	138.4-138.9	139.3	~2.0
S1	Sulfur in PbS	161.1	161.0 - 161.3	~1.5-2.2
S2	Neutral sulfur	162	162.0 - 162.8	~2.2-3.6
S3	Oxidised sulfur	166.9	~ 167.7-169.2	~2.0-2.4
S4	Oxidised sulfur	168.6	~ 170.4	~2.1

Table 1:Table of peak assignments[3,4].

Table 1 shows peak assignments for the XPS spectra. Peaks assigned to 'Oxidised sulfur' potentially consist of a mixture of $PbSO_3$ and $PbSO_4$. Due to the low signal to noise ratio and relatively large width of peaks due to the use of a lab-based x-ray source, however, it was difficult to separate these species. The same issue applies to the presence of oxidised lead, which was only successfully fitted in the sample synthesised using lead DBTC precursor – in the other samples, the peak width was too great to successfully fit more than a single doublet with any degree of precision, however it seems likely based on syntheses discussed in previous chapters that a significant amount may be present.

All three samples exhibit similar XPS spectra – a notable of oxidised sulfur is seen, along with a moderate amount of neutral sulfur. Ratios of species present are given in table 2. The errors in these ratios are typically two to three times larger than those seen for synchrotron data, due to the significant difference in signal-to-noise ratio between the two sources.

Ratio of	DETC sample	DBTC sample	DPTC sample
Total lead to total sulfur	0.8±0.1	0.9±0.1	0.9±0.1
Sulfur in PbS to oxidised sulfur	2.4±0.3	2.1±0.3	2.8±0.4
Lead in PbS to oxidised lead	-	2.4±0.2	-

Table 2: Table of species ratios.

The ratio of lead to sulfur in all three samples is fairly similar, with a slight excess of sulfur present. The amount of oxidised sulfur compared to sulfur in lead sulfide is also fairly similar for all three samples, with all having 2-3 times more sulfur in lead sulfide than oxidised sulfur. The DBTC sample exhibits the largest relative amount of oxidised sulfur, and the DPTC sample exhibits the least. This corresponds well to conclusions drawn from the XRD and electron microscopy, which indicated the DPTC having the largest particles (which would be likely to have the lowest proportion of oxide) . It is unclear whether the neutral sulfur present originates from decomposition products of the lead precursor, or whether it is a product of aging as indicated in previous chapters, or a combination of both of these factors. Higher resolution analysis of the lead and sulfur peaks, over a variety of ages would assist in determining this, the presence of neutral sulfur as an oxidation product has been proposed for an oxidation mechanism wherein the initial step is decomposition of the lead sulfide into oxidised lead and neutral sulfur.

7.5 Absorption spectroscopy

The absorption of the films was tested using a Perkin-Elmer Lambda 1050 UV-Vis-NIR spectrometer. Samples were deposited on glass slides, which themselves were mounted on glass in order to be introduced to the spectrometer. Any small, sharp peaks and troughs present within the spectra are likely to be due to a combination of scattering and/or imperfect removal of the background absorption produced by the sample mount

and substrate. As a directly equivalent background measurement could not be made, the background was removed by finding the minima of the sample spectrum, and applying a factor to the background spectrum such that the absorption at this minima was identical in both spectra. This adjusted background spectrum was then subtracted to provide a realistic estimate of the samples true absorption profile. Figures 7.9, 7.10, and 7.11 show absorption spectra of the samples synthesised using lead DETC, DBTC, and DPTC precursors respectively. Literature spectra for the absorption spectrum of bulk lead sulfide thin films can be found in chapter 6, and will be referred to for comparison.

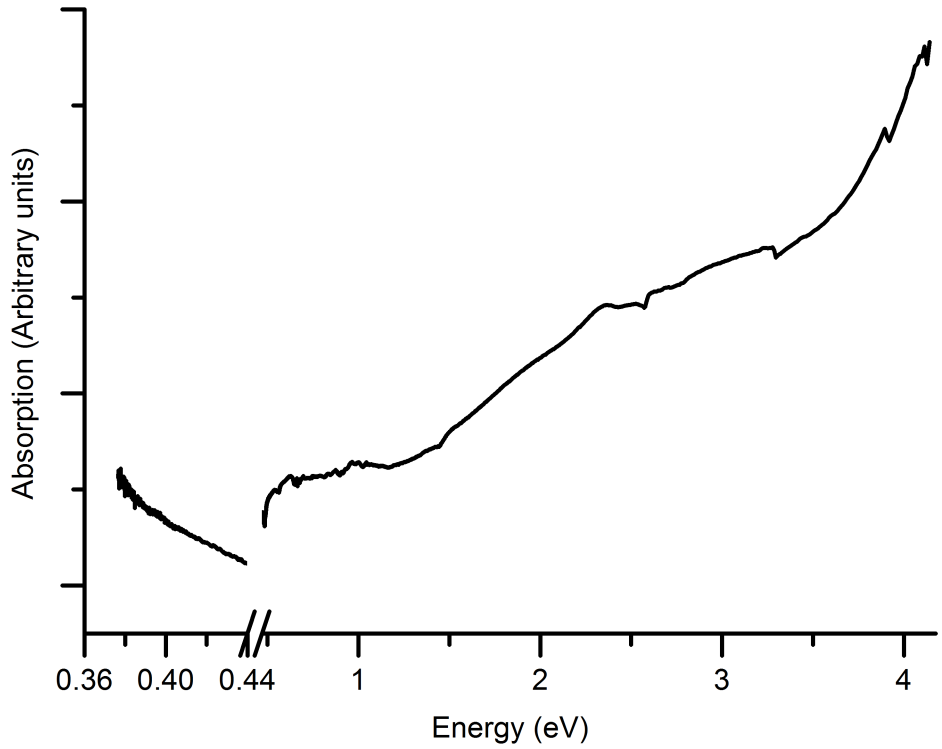

Figure 7.9: Absorption spectrum of PbS synthesised using lead DETC precursor.

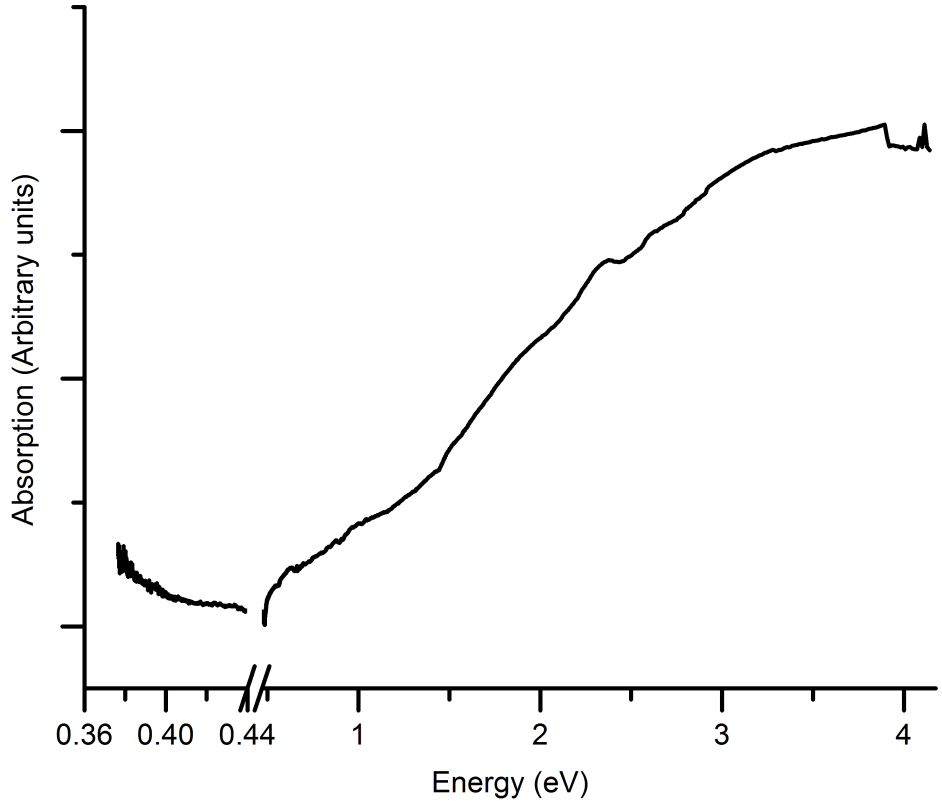

Figure 7.10: Absorption spectrum of PbS synthesised using lead DBTC precursor.

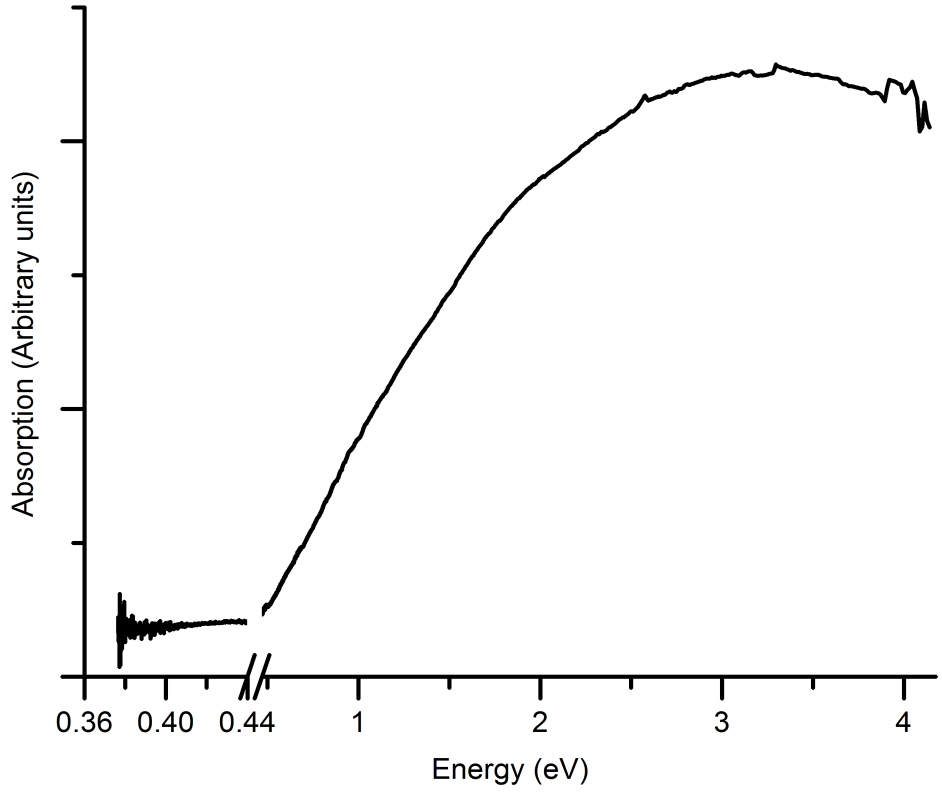

Figure 7.11: Absorption spectrum of PbS synthesised using lead DPTC precursor.

As with absorption spectra for samples synthesised using lead DETC precursor in varying concentrations discussed in chapter 6, the sample synthesised here using 2 mM of both lead DETC and sodium sulfide nonahydrate exhibits a sharp rise shortly after the bulk bandgap, as well as some small local maxima of absorption at just above 1 eV and just below 2.5 eV photon energy which are not present in the absorption spectrum of bulk lead sulfide. Similar features are visible in the sample synthesised using lead DBTC, although the maxima at around 1 eV is barely present, and a more even, gradual increase in absorption is seen. The sample synthesised using lead DPTC however, exhibits no identifiable absorption features within its spectrum. The reasons for the presence, or lack, of these features are unclear.

7.6 Summary and conclusions

A notable trend in particle size was observed from the XRD, with the average estimated particle size increasing with increasing precursor size. This is supported to an extent by the TEM images of the samples, in which the DPTC sample appeared to contain a greater proportion of larger particles and agglomerates. XPS of these samples is generally relatively uniform, with all samples showing small amounts of neutral and oxidised sulfur. The DPTC sample exhibits the least relative sulfur oxidation, which is what would be expected from the largest synthesised particles, due to surface-area to volume ratios resulting in a lower rate of oxidation the larger the particle. Oxidised lead species were only identified in the DBTC sample, however it is likely that oxidised lead is present in all samples, but simply could not be fit due to the peak width and low signal provided by the lab-based x-ray source.

References

(1) Patterson, A. *Physical Review* **1939**, *56*, 978-982.

(2) Fan, D.; Thomas, P. J.; O'Brien, P. *Journal of the American Chemical Society* **2008**, *130*, 10892-4.

(3) Hardman, S. J. O.; Graham, D. M.; Stubbs, S. K.; Spencer, B. F.; Seddon, E. A.; Fung, H.-T.; Gardonio, S.; Sirotti, F.; Silly, M. G.; Akhtar, J.; O'Brien, P.; Binks, D. J.; Flavell, W. R. *PCCP* **2011**, *13*, 20275-83.

(4) Park, R. L. *Applications Of Surface Science* **1977**, *1*.

(5) Cademartiri, L.; Montanari, E.; Calestani, G.; Migliori, A.; Guagliardi, A.; Ozin, G. a. *Journal of the American Chemical Society* **2006**, *128*, 10337-10346.

(6) *Lead Sulphide Powder Diffraction File - PDF#00-003-0665 (accessed 21/03/12)*.

Chapter 8: Aging of lead sulfide nanoparticle thin films

Due to the surface oxidation observed in previous results, investigation of the aging of the synthesised films as a function of time was necessary. Syntheses of lead sulfide films using lead DETC at a solvent height of 19±1 mm and at a range of precursor concentrations (2 mM lead precursor to 1 mM sulfide precursor; 1 mM lead precursor to 1 mM sulfide precursor; and 1mM lead precursor to 2mM sulfide precursor) were carried out, and the initial characterisation of these films can be found in chapter 6 of this thesis. Initial XPS was carried out at beamline Bach, Elettra synchrotron, Italy. The same films were later investigated with XPS after approximately 9 months of ageing in air at beamline I311 at MAXLab synchrotron, Sweden. A second set of samples, synthesised under identical conditions and allowed to age for 3 weeks, were also investigated. The ageing of a sample synthesised using the unpurified lead dithiobiuret precursor (discussed in chapter 5 of this thesis) at a solvent height of 19±1 mm and precursor concentrations of 1 mM lead dithiobiuret to 1 mM sodium sulfide was also investigated using XPS which was performed 1 week after synthesis and again at 9 months after synthesis.

8.1 Ageing of samples synthesised using lead DETC

8.1.1 XPS spectra

Figures 8.1, 8.2, and 8.3 show XPS spectra of samples synthesised using lead diethyldithiocarbamate at varying precursor concentrations, taken approximately 1 week, 3 weeks, and 9 months after synthesis respectively.

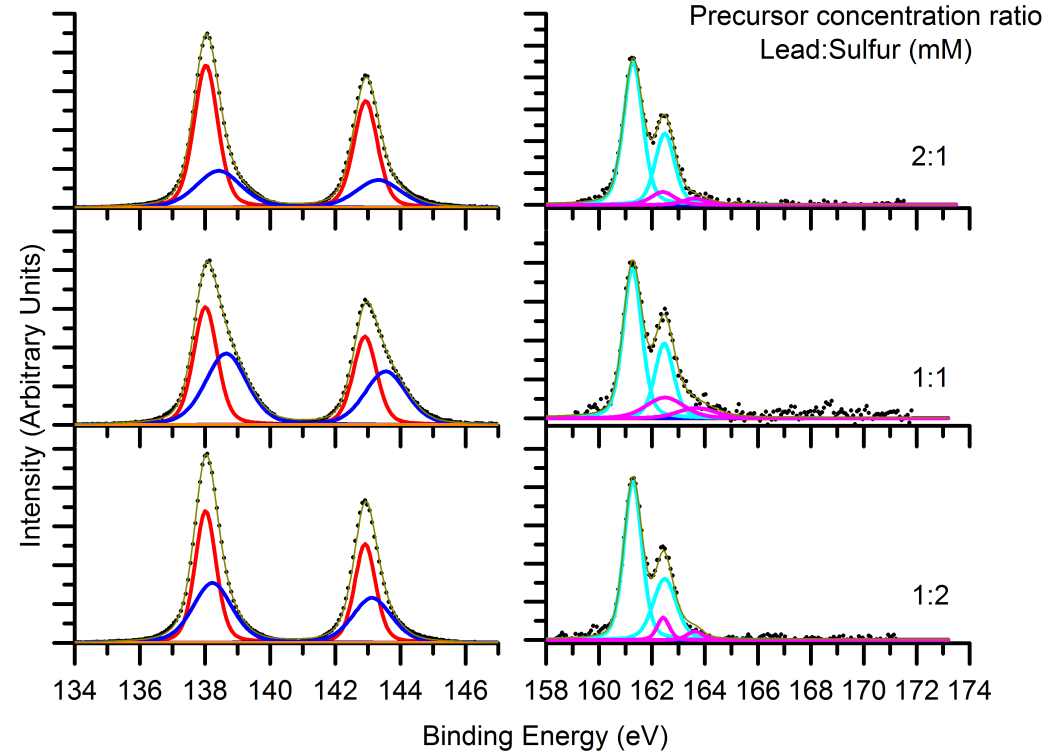

Figure 8.1: XPS spectra taken at a photon energy of 1000 eV (corresponding to a sampling depth of 6.2 nm) of PbS films synthesised using varying precursor concentrations of lead DETC and sulfur precursor, approximately one week after synthesis.

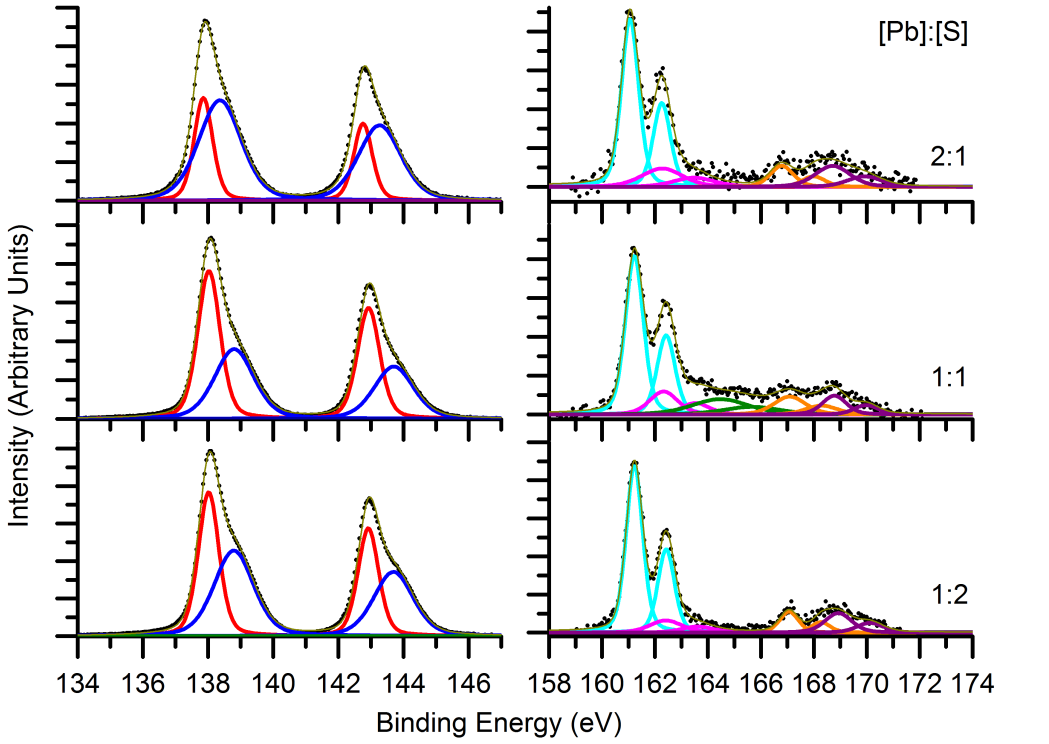

Figure 8.2: XPS spectra taken at a photon energy of 1000 eV (corresponding to a sampling depth of 6.2 nm) of PbS films synthesised using varying precursor concentrations of lead DETC and sulfur precursor, approximately three weeks after synthesis.

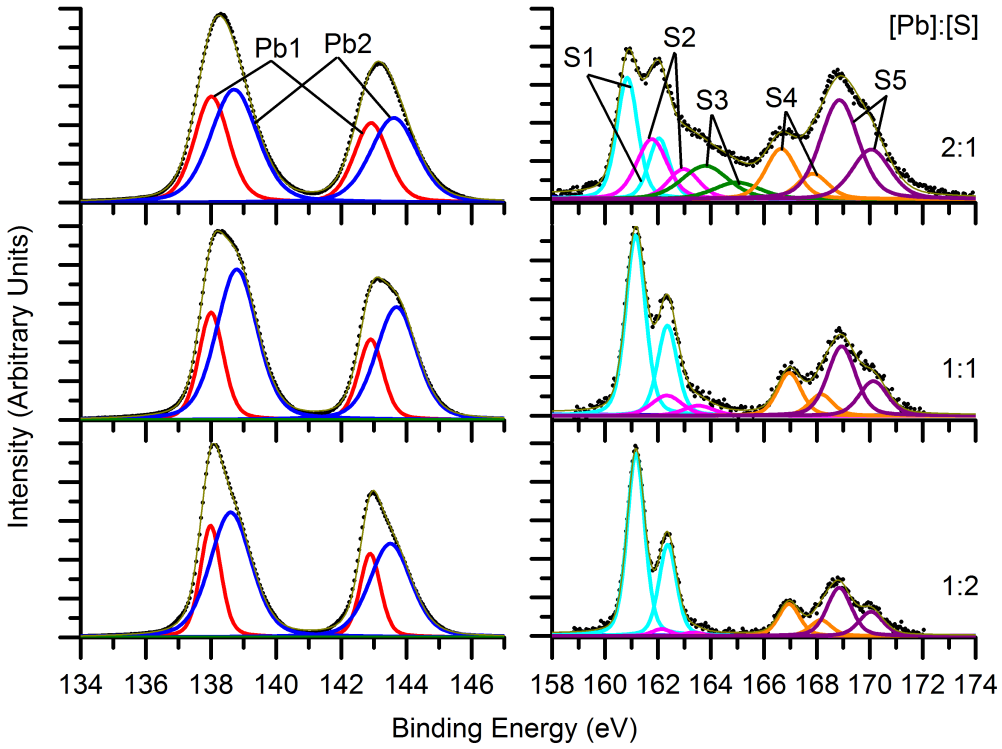

Figure 8.3: XPS spectra taken at a photon energy of 1000 eV (corresponding to a sampling depth of 6.2 nm) of PbS films synthesised using varying precursor concentrations of lead DETC and sulfur precursor, approximately nine months after synthesis.

Peaks were assigned as shown in table 1, corresponding to the labels in figure 8.3 (in which all identified species are present).

Peak label	**Assignment**	**Literature Binding Energy (eV)**	**Observed Binding Energies (eV)**	**Observed FWHM (eV)**
Pb1	Lead in PbS	138	Assigned to 138	~0.8-1.2
Pb2	Oxidised lead	138.4-138.9	138.2-138.8	~1.3-1.7
S1	Sulfur in PbS	161.1	160.8-161.25	~0.8-1.0
S2	Neutral sulfur	162	161.75-162.4	~0.8-1.4
S3	$PbSO_n$	~163-165	163.7-164.4	~2.0
S4	Sulfur in $PbSO_3$	166.9	166.7-167.0	~0.9-1.4
S5	Sulfur in $PbSO_4$	168.6	168.7-168.9	~1.1-1.7

Table 1: Table of peak assignments[1–4].

All samples show relatively low oxidation visible in the sulfur 2p peak at one week after

synthesis. The samples exposed to air for three weeks display notably more oxidation, in the form of lead sulfite and sulfate (S4 and S5), with no significant difference between the samples synthesised at different precursor concentrations. After nine months a notable difference appears between the samples synthesised at different concentrations. The sample synthesised with 2:1 mM concentrations of the lead to sulfur precursors respectively shows the highest proportion of oxidised sulfur species, while the sample synthesised with 1:2 mM concentrations of the lead to sulfur precursors shows the lowest proportion of oxidised sulfur species. This is likely due to the difference in particle size noted in chapter 6 – the sample synthesised using a 2:1 lead:sulfur ratio exhibited the smallest estimated particle sizes, while the sample synthesised using a 1:2 lead:sulfur ratio exhibited the largest. The difference in the amounts of sulfoxy species seen in the samples after 9 months of exposure to air can therefore be attributed to the difference in surface-area to volume ratio of particles within the sample. A similar trend can be seen in the presence of neutral sulfur (S2). This is potentially due to neutral sulfur being generated as a by-product of the oxidation process. The sample synthesised with a 2:1 mM lead to sulfur precursor concentration is also the only sample in which the species labelled 'S3', assigned to sulfur in partially oxidised lead sulfide as reported by Yashina *et al.*[4], can be seen.

Oxidation of the lead occurred far more rapidly than observed in the sulfur, with all samples exhibiting a significant proportion of oxidised lead after only one week's exposure to air. This indicates that oxidation of lead seperately to the sulfur occurs as the initial step in the oxidation mechanism of the lead sulfide particles, resulting in an oxidised species such as lead hydroxide, carbonate, hydrated oxide, or a combination thereof. The neutral sulfur observed would thus be the byproduct of this process. After one weeks oxidation, the proportions of neutral sulfur and oxidised lead seem to approximately correspond – the sample with the highest proportion of oxidised lead also contains the highest proportion of neutral sulfur, and the reverse is also true. While the relative proportions of lead in PbS to oxidised lead and sulfur in PbS to neutral sulfur are not identical, this is likely due to the propensity of neutral sulfur to be removed in vacuum at ambient temperatures[3,5].

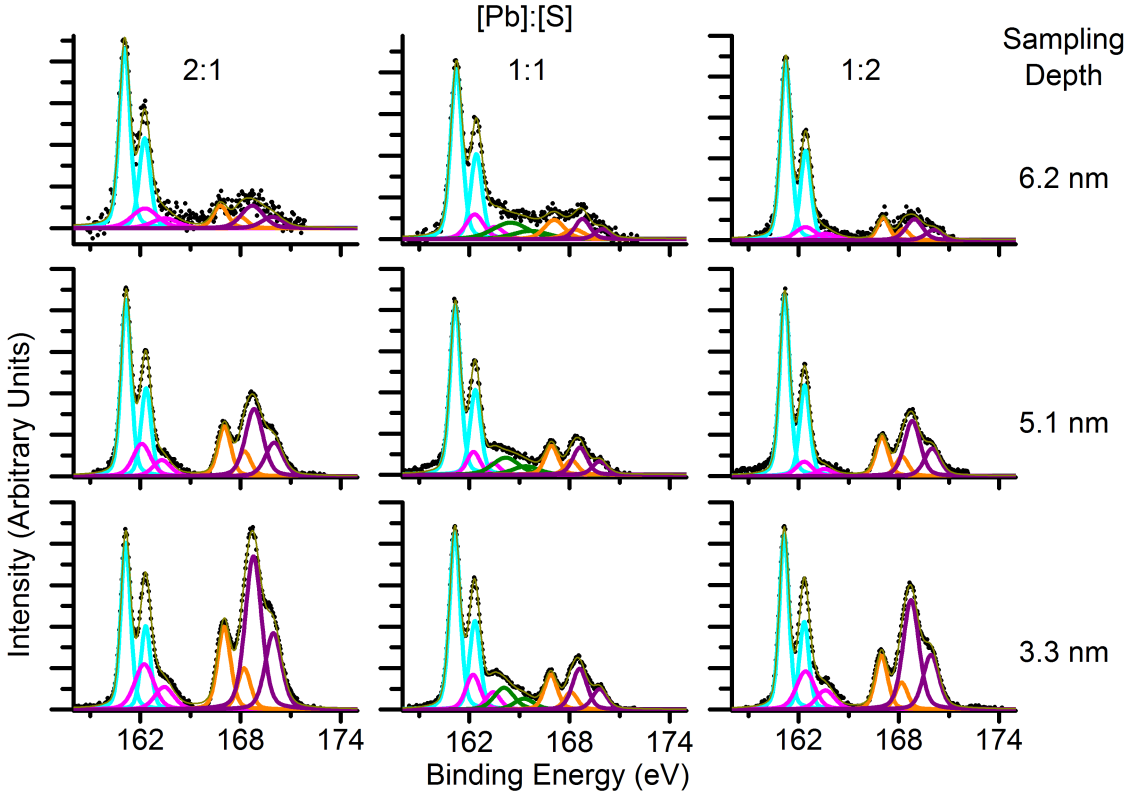

Figure 8.4: XPS spectra of the sulfur 2p peak at varying sampling depths for PbS films exposed to air for three weeks. Sampling depths from top to bottom correspond to photon energies of 1000, 800, and 500 eV respectively.

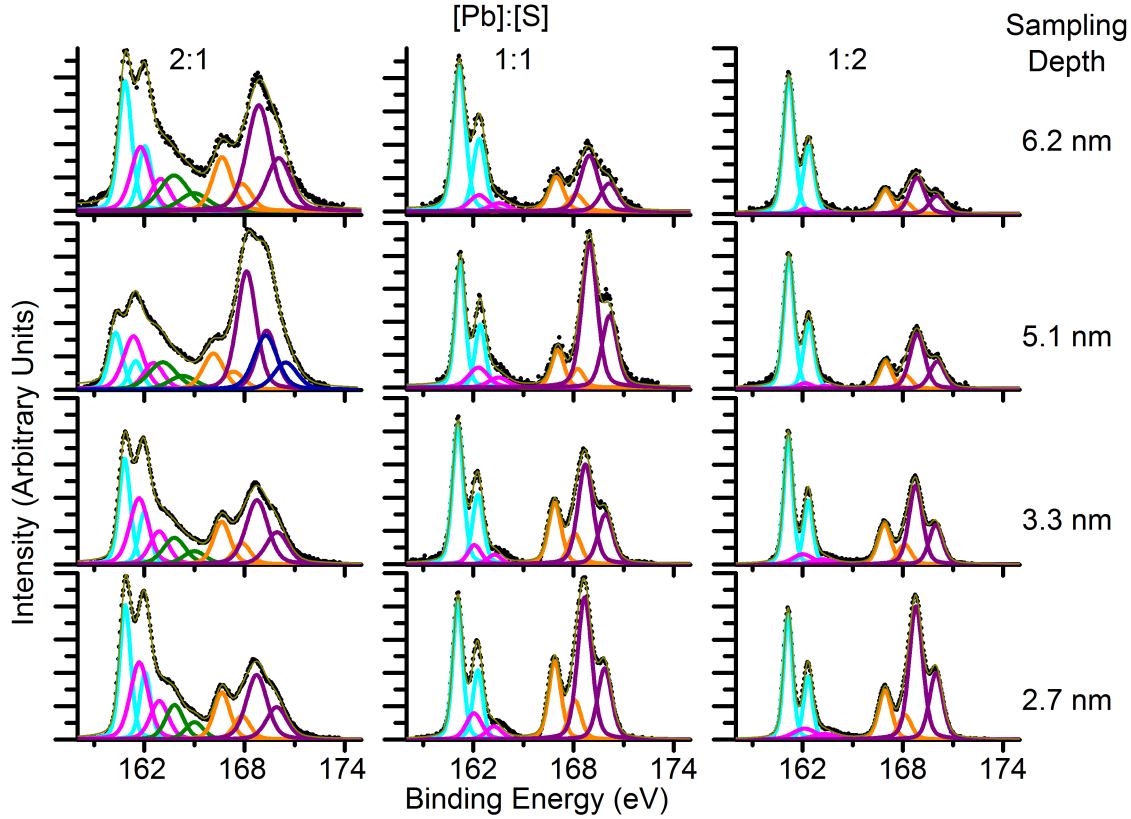

Figure 8.5: XPS spectra of the sulfur 2p peak at varying sampling depths for PbS films exposed to air for nine months. Sampling depths from top to bottom correspond to photon energies of 1000, 800, 500 and 400 eV respectively.

Figures 8.4 and 8.5 show the sulfur 2p XPS spectra for the lead DETC PbS samples at varying sampling depths for the samples exposed to air for three weeks and nine months respectively.

In all samples, at three weeks exposure to air there is a noticeable increase in oxidation of the sulfur in comparison to after one week, in the form of lead sulfite and lead sulfate, concentrated towards the surface of the particle. This increase is most pronounced in the samples synthesised with asymmetric precursor stoichiometry, while the sample synthesised with a 1:1 lead:sulfur precursor ratio displays more uniform oxidation. The samples exposed to air for nine months are noticeably more oxidised than those exposed for three weeks, as would be expected. However the difference is not as significant as the difference in oxidation between samples exposed to air for one week and those exposed to air for three weeks (as seen in comparison between figures 8.1 and 8.2). This indicates that oxidation happens more rapidly immediately after synthesis and progresses more slowly over time. For the samples exposed to air for nine months, only the sample synthesised with a 1:2 ratio of lead to sulfur precursors shows a significant increase in oxide at lower sampling depths. The samples synthesised with 2:1 and 1:1 ratios of lead to sulfur precursors show fairly uniform oxidation across the range of sampling depths examined, with both showing a maximum in intensity of oxidised species at a sampling depth of 5.1 nm. While the oxidised sulfur is generally localised to the surface, this is especially true of the sulfate, which exhibits a far sharper drop in intensity with increasing sampling depth than is seen for the sulfite. This is particularly notable in the 2:1 and 1:2 samples in figure 8.4 after three weeks' aging.

The increase in oxide observed at a 5.1 nm sampling depth is unusual, and could not be explained by the presence of overlapping auger peaks or by any known instrumental factors. A potential explanation would be that the sampling depth is exceeding the radius of the particle, and thus the proportion of particle surface being sampled is increasing due to the particles sides curving back inwards. This explanation seems unlikely, however, as the minimum estimated particle size from XRD for these particles was approximately 10 nm, and therefore the sampling depth of 5.1 nm indicates that a very small proportion of the signal (<5%) is originating from the bottom 'half' of the particles. The increase in oxidised sulfur is also much sharper than would be expected if this were the case – this would instead produce a gradual increase with increased sampling depth. Another

potential explanation is that this effect is due to some unusual morphology, for example if the base of the particles came to a point (or similarly narrow structure) which was thus more vulnerable to forming oxidised sulfur species, this could conceivably create a sharp increase in the proportion of oxide observed with increasing sample depth. However, this would require the stated morphology to occur in a large proportion of the particles, and occur uniformly at a specific depth within the film. As such, the exact reason for this phenomenon remains unclear.

Unlike with the less aged samples, there is a clear trend in oxidation with precursor concentration in the samples exposed to air for nine months; as the relative concentration of the lead precursor increases, so does the relative intensity of oxidised sulfur species. The sample synthesised with a 2:1 lead to sulfur ratio has the highest level of oxidation, while the sample synthesised with 1:2 lead to sulfur precursor concentrations has the lowest. This is likely due to the difference in particle sizes as shown in the XRD of these samples in chapter 6; the sample synthesised with a 2:1 lead to sulfur ratio exhibited the smallest particles, and thus had the highest surface-area to volume ratio, leading to a greater proportion of oxidised sulfur.

Neutral sulfur appears present throughout the samples at all ages, with a greater proportion present closer to the surface, and a clear increase with increasing sample age. This further supports the proposition that the neutral sulfur is formed as a product of the oxidation.

8.1.2 Chemical species ratios

Figure 8.6 shows how the ratios of lead and sulfur species vary across sampling depth and sample age for all precursor concentration ratios. The ratios of all lead species to all sulfur species shows similar behaviour across all samples. In the samples exposed to air for one week, the ratio of lead to sulfur remains around 1:1 throughout all sampling depths. As the sample age increases, a gradient of increasing lead to sulfur ratio towards greater sampling depths begins to emerge. The ratio of lead to sulfur remains most consistent at the lowest sampling depths for all samples, with the gradient being the result of increasing lead to sulfur ratio deeper within the sample (as opposed to being caused by decreasing lead to sulfur ratio at the surface). This is potentially explained by migration of sulfur from within the particle to the surface, where some is removed due to volatility in vacuum. Elemental sulfur as an oxidation product has previously been proposed to form an amorphous layer at the surface[5] and has been reported to be volatile and removed

from samples in vacuum conditions at ambient temperature[3,5].

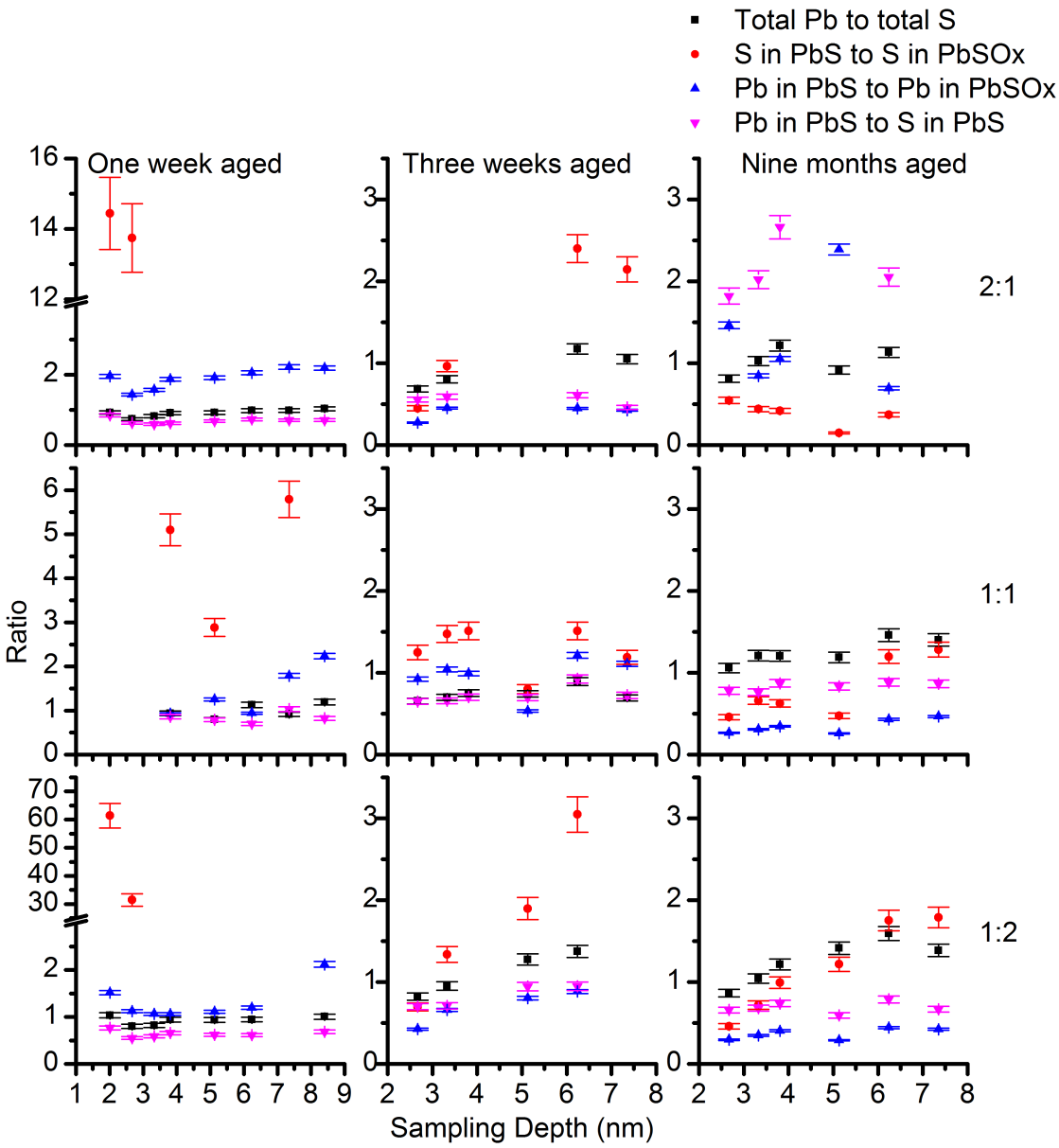

Figure 8.6: Graph showing various ratios of species present in DETC PbS samples, as a function of sampling depth. Ratios shown are: lead in lead sulfide to lead in oxidised species; sulfur in lead sulfide to sulfur in oxidised species; and total lead present to total sulfur present. The ratio of lead to sulfur precursor concentrations is given on the right.

The ratio of lead in lead sulfide to lead in oxidised species displays a slight increase towards greater sampling depths in several of the samples at multiple ages (clearest in the '1:2' precursor ratio sample at three weeks aged, and in the '1:1' precursor ratio sample at one week aged). This indicates that as lead is removed from the crystal via oxidation to non-sulfur containing products (such as the previously proposed hydroxide, carbonate, or oxide/hydrated oxide) it may become volatile and liable to be lost from the surface of the

particles. As the age of samples increases, there is a slight decrease in the ratio of lead in lead sulfide to lead in oxidised species in all samples.

The ratio of sulfur in lead sulfide to sulfur in oxidised species varies between the samples. In all three sets of synthesis conditions very little sulfite/sulfate formation is observed after one week of aging, with high ratios of sulfur in lead sulfide to sulfur in oxidised species, and with oxidised species not intense enough to be quantifiable at greater than 3 nm sampling depth for both samples synthesised with non-stoichiometric precursor concentrations. The sample synthesised with a 1:1 ratio of precursor concentrations displays a higher level of oxidation at one week of aging, with oxidised species identifiable at all sampling depths.

The samples exposed to air for three weeks display a much greater level of oxidised sulfur species. Both samples synthesised with non-stoichiometric precursor concentrations display a strong increase in the ratio of sulfur in lead sulfide to sulfur in oxidised species as sampling depth increases, indicating that the sulfite/sulfate species are concentrated at the surfaces of the particles. The sample synthesised with 1:1 precursor concentration ratios however differs again, exhibiting a relatively uniform level of sulfoxy species across all sampling depths, albeit with a peak sulfite/sulfate concentration at a sampling depth of approximately 5 nm.

In all of the samples exposed to air for nine months, an even greater level of sulfite/sulfate formation is observed. In the sample synthesised with 1:2 lead to sulfur precursor concentrations, the ratio of sulfur in lead sulfide to sulfur in oxidised species is relatively similar near the surface in the sample aged for nine months and the sample aged for three weeks. The increase in sulfite/sulfate formation is instead manifested in a greater concentration of sulfoxy species at larger sampling depths, although the greatest amount of oxide is still present at the surface.

The highest amount of oxidised sulfur after nine months of aging was observed in the sample synthesised with a 2:1 ratio of lead to sulfur precursors. At this age, the sample also exhibits an increase in the concentration of oxidised sulfur species towards greater sampling depths, a phenomenon which has not been observed in any other sample. As seen in figure 8.5, this sample also exhibits a much greater concentration of neutral sulfur

than any other sample at this age. It is expected that this sample would display the largest proportion of oxidation, as it has the smallest average estimated particle size from the XRD shown in chapter 6. The reason for the observed increase in oxidation with increasing sampling depth is unclear, but could be explained by an unusual particle morphology, as discussed earlier with regards to the anomalous peak in oxidised sulfur at a sampling depth of 5.1 nm.

8.1.3 Oxidised sulfur layer thickness

Oxidised layer thickness from ratios of sulfur to oxidised sulfur species were calculated for the particles using the method for calculation of shell thicknesses of spherical particles described in Shard *et. al.*[6]. For simplification purposes, the inelastic mean free path of electrons in lead sulfide and lead sulfate/sulfite were assumed to be the same. The particle size used for these calculations was 10 nm, an approximate estimate of the size of the smallest particles present in these samples based on estimated particle sizes given in chapter 6. Oxidised sulfur thickness estimates across a range of sampling depths, for all ages of the sample synthesised using 1:1 lead:sulfur precursor concentrations are given in figure 8.7.

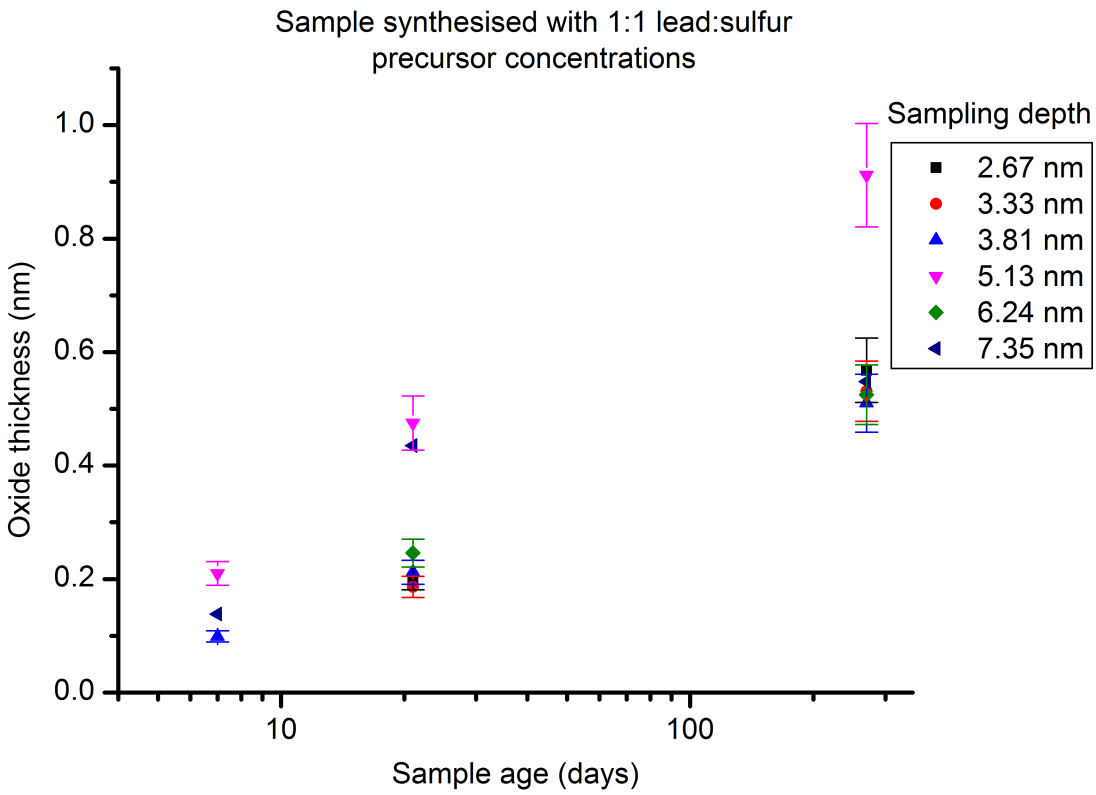

Figure 8.7: Calculated oxide layer thicknesses assuming a spherical particle of 10 nm diameter, for the sample synthesised using 1:1 mM lead:sulfur precursor concentrations. Sample age is presented on a log10 scale.

All samples displayed a similar behaviour with age, exhibiting a rapid initial increase in oxidised sulfur thickness which slows with time, indicating an eventual saturation of oxidation in the samples. Thickness of the oxidised sulfur layer was found to follow a logarithmic relationship with time, as shown in figure 8.7. Maximum calculated oxide thicknesses at an age of ~270 days were 1.38 nm for the sample synthesised with 2:1 lead:sulfur precursor concentrations, 0.91 nm for the sample synthesised with 1:1 (above) and 0.57 for the sample synthesised with 1:2 lead:sulfur precursor concentrations.

Excluding the anomalous behaviour exhibited at a sampling depth of ~5 nm, the calculated thicknesses are extremely consistent across sampling depths, indicating that sulfoxy species form a well-defined layer on the surface of the particles. Figure 8.8 shows a schematic cross-section of a nanoparticle of 10 nm diameter with layers of 0.2 nm and 1 nm thickness overlaid. These correspond to the approximate oxidised layer thicknesses shown in figure 8.7 after 1 weeks exposure to air and 9 months exposure to air respectively. The intensity of the XPS signal as a function of depth is shown for three

sampling depths as a reference.

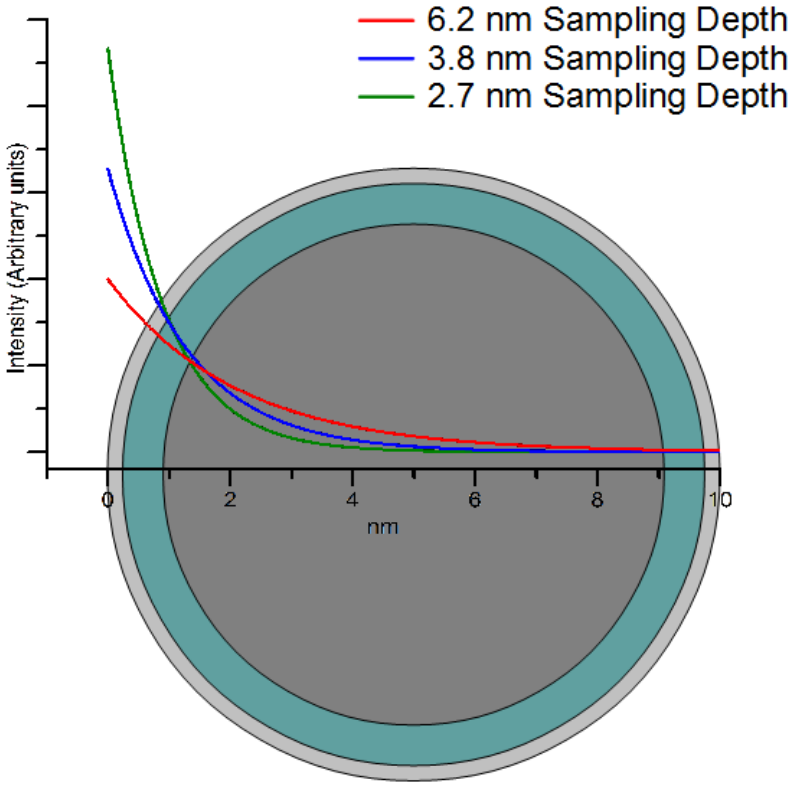

Figure 8.8: Schematic diagram of example oxidised sulfur layer thicknesses on a particle with a diameter of 10 nm. Curves illustrating the relative intensity of signal as a function of XPS sampling depth are overlaid for reference. The outer 'shell' represents a layer of thickness ~0.2 nm; the inner shell represents a layer of thickness ~1 nm.

8.2 Ageing of PbS synthesised using the lead thiobiuret precursor

Figures 8.9 and 8.10 show depth-profiling XPS of one-week-aged and nine-month-aged (respectively) samples synthesised using the unpurified lead thiobiuret precursor discussed previously in chapter 5.

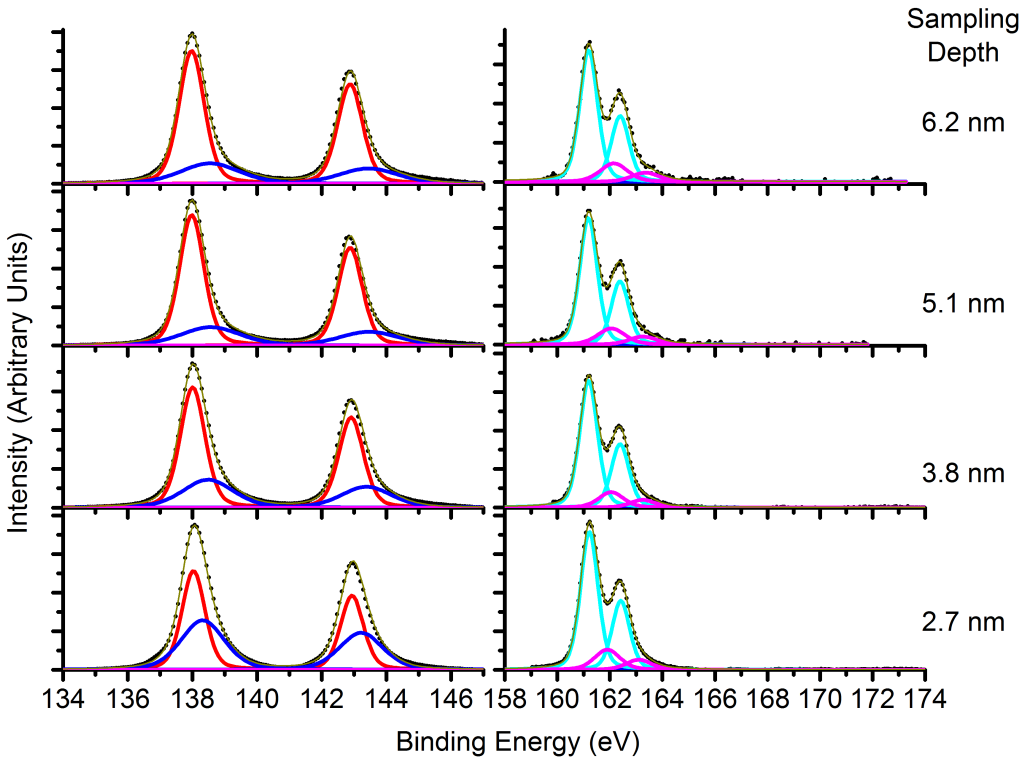

Figure 8.9: Depth profiling XPS spectra of the lead 4f and sulfur 2p peaks of the PbS film synthesised using the lead thiobiuret precursor, after one week of exposure to air. Sampling depths from top to bottom correspond to photon energies of 1000, 800, 500 and 400 eV respectively.

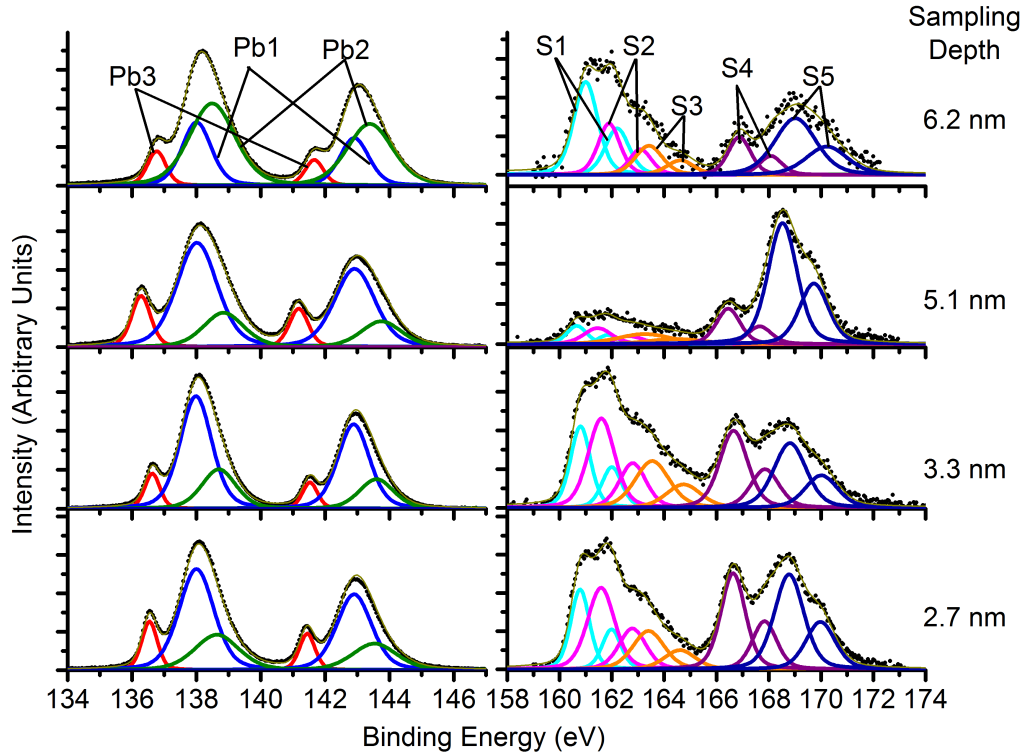

Figure 8.10: Depth profiling XPS of the lead 4f and sulfur 2p peaks of the PbS film synthesised using the lead thiobiuret precursor, after nine months of exposure to air. Sampling depths from top to bottom correspond to photon energies of 1000, 800, 500 and 400 eV respectively.

Peak assignments for the spectra shown in figures 8.9 and 8.10 are as described in table 1, with the addition of the Pb3 doublet, which is assigned to neutral lead, and located at a binding energy of 136.3-136.75 eV (expected at ~136.8 eV^2) As with the samples synthesised using lead diethyldithiocarbamate, after one week of aging the sulfur 2p peak shows little to no evidence of oxidised species, while the lead 4f peak shows the presence of a small amount of oxidised lead throughout the sample, which increases towards the surface. After nine months of aging, the sample exhibits an increase in oxidation similar to that seen in previous samples, and also displays the peak in oxidation around 5nm sampling depth which has been seen in several of the previous samples. A notable difference to the samples synthesised using lead DETC is the presence of significant amounts of neutral lead, along with larger amounts of neutral sulfur than was seen in the previous samples. This indicates a greater proclivity for decomposition of the lead sulfide than was seen in the samples synthesised with lead DETC, either through oxidation or synchrotron radiation damage.

Figure 8.11 shows the ratios of both sulfur and lead in lead sulfide to their oxidised species, as well as the ratio of total lead to total sulfur as a function of sampling depth for both one week and nine months aged samples.

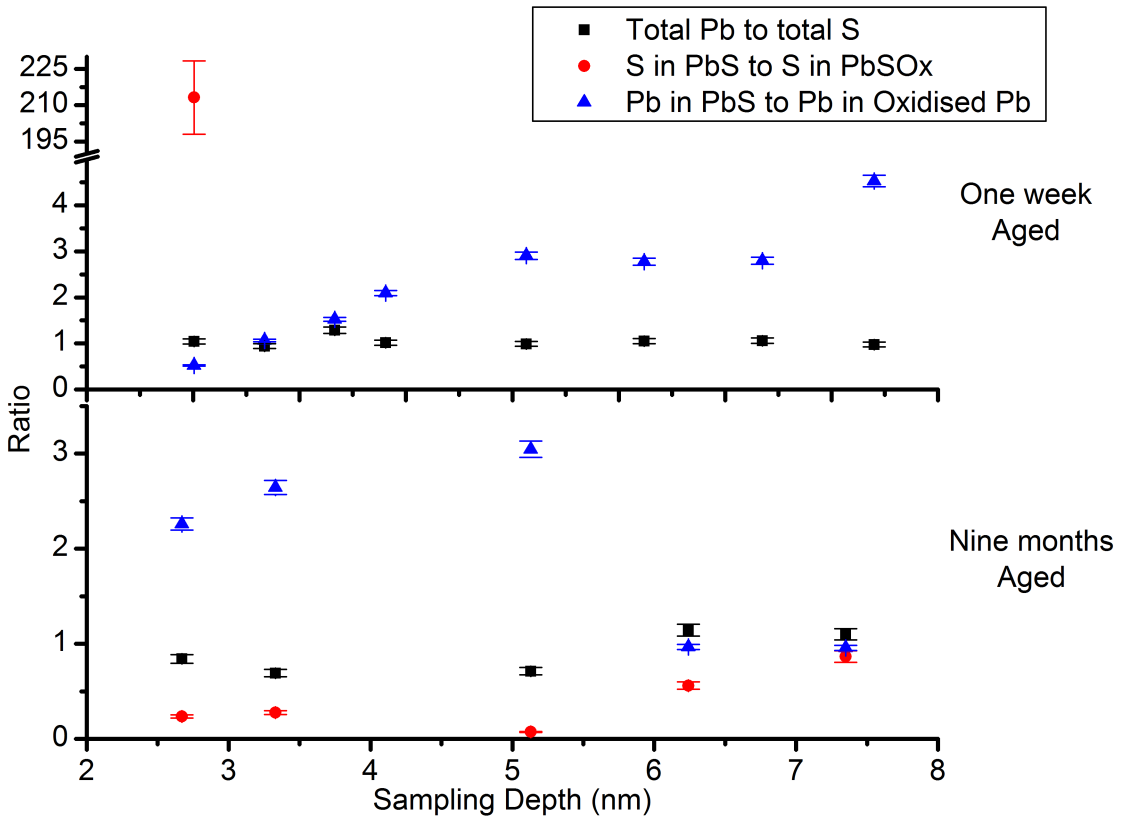

Figure 8.11: Ratios of chemical species present across all sampling depths for both one week old and nine months old PbS films.

The ratio of lead in lead sulfide to oxidised lead in the samples synthesised using the lead thiobiuret precursor after one week of aging shows a considerable increase with sampling depth, in contrast to the samples synthesised with the lead diethyldithiocarbamate precursor, which showed a much lower gradient. A plateau in the lead in lead sulfide to oxidised lead ratio is visible between approximately 5-7 nm. This is potentially for the same reason as the sharp increase in oxide seen in previous samples at approximately 5 nm sampling depth, and seems likely to be related to particle morphology as discussed previously.

At both ages, the total lead to total sulfur ratio is fairly uniform throughout the sample, with only a slight increase with sampling depth being visible in the nine months aged sample. This suggests that unlike the samples synthesised using the lead DETC precursor, there is little migration or loss of either element, or the loss is congruent in nature.

The ratio of sulfur in lead sulfide to sulfur in lead oxide is extremely high after one weeks aging, and relatively uniform after nine months, although it does exhibit the sharp decrease in ratio at approximately 5 nm sampling depth, followed by a slight increase at

higher sampling depth.

8.3 Summary and conclusions

All samples examined exhibited a similar rate of oxidation over time; barely any oxidised sulfur species were seen after one weeks' exposure to air. After three weeks' exposure to air, significant amounts of sulfoxy species were observed, however oxidation rate appeared to decrease with time, with a proportionally smaller increase in sulfite/sulfate after nine months of aging. After nine months of aging, sulfide in lead sulfide to oxidised sulfide ratios that reached, at minimum, around 0.5:1 were observed. Oxidised sulfur species were concentrated on the surface of samples in most cases, with many displaying a high gradient in the ratio of sulfur in lead sulfide to oxidised sulfur with increasing sampling depth. Sulfate appeared to be especially concentrated on the surface of many samples relative to sulfite. This concentration of sulfate at the surface is most obvious after three weeks aging; after nine months, the decrease in sulfate with increasing sampling depth was less sharp, and absent completely in the sample synthesised with a 2:1 lead to sulfur ratio. This indicates that the sulfate is likely formed as the terminal product of oxidation. A sharp increase in oxidised species, particularly sulfur in lead sulfate, was also observed in several samples at a sampling depth of just over 5 nm. The reason for this was not clear, but may be due to unusual particle morphology resulting in an abnormal depth profile. After nine months, the most oxidised samples exhibited a relatively uniform sulfur to oxidised sulfur ratio throughout, indicating uniform oxidation of the particles to a depth of several nanometers.

The relative amounts of lead to sulfur in all samples increased slightly with age and depth sampled, indicating a potential migration of neutral sulfur, formed as an initial oxidation product, to the surface of the particles, where some is lost in vacuum due to volatility[5]. This effect was notably not present in the sample synthesised with lead thiobiuret, which did however display a much larger proportion of neutral lead and sulfur throughout the sample after nine months of aging. The ratio of lead in lead sulfide to lead in lead oxide was relatively uniform throughout all samples, with a very slight increase with sampling depth seen in some samples.

In general, the thickness of oxide in all samples seems to follow a logarithmic relationship with time, oxidising relatively rapidly at first, but quickly reaching a plateau

at a certain proportion of oxide to lead sulfide throughout.

The oxidation mechanism of the nanoparticles appears to begin within an initial step resulting in the formation of oxidised lead species. Based upon the binding energies observed for this oxidised species, it is believed to be a form of lead hydroxide or hydrated oxide; lead hydroxide has been previously proposed as an initial product[3] in the oxidation of lead sulfide. Lead hydroxide is not stable in solid phase however, and as such a more likely source of the oxidised lead species seen is lead in hydrated lead oxide, $Pb_6O_4(OH)_4$ formed after the initial oxidation of lead to lead hydroxide . Neutral sulfur is also observed as a product of this initial oxidation step, albeit in lower proportion than the oxidised lead species. This is likely due to the volatility of neutral sulfur in vacuum resulting in the removal of sulfur from the sample. Following this step, it appears oxidation proceeds much slower, and sulfoxy species such as sulfite and sulfate are formed, with formation of sulfate being the terminating step. A possible reaction route is proposed in equations 1 – 5, where SO_2 is proposed as the intermediate reaction product in the formation of lead sulfite.

$$PbS + 2H_2O \Rightarrow Pb(OH)_2 + 2H + S \quad (1)$$

$$6Pb(OH)_2 + 2H_2O \Rightarrow Pb_6O_4(OH)_4 + 6H_2 \quad (2)$$

$$S + O_2 \Rightarrow SO_2 \quad (3)$$

$$Pb_6O_4(OH)_4 + 6SO_2 \Rightarrow 6PbSO_3 + 2H_2O \quad (4)$$

$$PbSO_3 + \frac{1}{2}O_2 \Rightarrow PbSO_4 \quad (5)$$

References

(1) Park, R. L. *Applications Of Surface Science* **1977**, *1*.

(2) Hardman, S. J. O.; Graham, D. M.; Stubbs, S. K.; Spencer, B. F.; Seddon, E. A.; Fung, H.-T.; Gardonio, S.; Sirotti, F.; Silly, M. G.; Akhtar, J.; O'Brien, P.; Binks, D. J.; Flavell, W. R. *: PCCP* **2011**, *13*, 20275-83.

(3) Buckley, A. N.; Woods, R. *Applications of Surface Science* **1984**, *17*, 401-414.

(4) Yashina, L. V.; Zyubin, A. S.; Püttner, R.; Zyubina, T. S.; Neudachina, V. S.; Stojanov, P.; Riley, J.; Dedyulin, S. N.; Brzhezinskaya, M. M.; Shtanov, V. I. *Surface Science* **2011**, *605*, 473-482.

(5) Hampton, M. A.; Plackowski, C.; Nguyen, A. V. *Langmuir : the ACS journal of surfaces and colloids* **2011**, *27*, 4190-201.

(6) Shard, A. G. *The Journal of Physical Chemistry C* **2012**, *116*, 16806-16813.

Chapter 9: Summary and conclusions

Films of lead sulfide nanoparticles were synthesised *via* the liquid-liquid interface method using a variety of precursors and synthesis conditions. Films were synthesised using lead diethyldithiocarbamate, lead dibutyldithiocarbamate, lead dipentyldithiocarbamate and lead dithiobiuret precursors. Films synthesised using lead DETC were investigated at a range of solvent heights and precursor concentrations. The aging of films synthesised using lead DETC was also investigated. Films synthesised using lead dithiobiuret were also investigated at a range of solvent heights and ages. Films synthesised using lead DETC, DBTC and DPTC were synthesised under identical conditions for comparison.

9.1 Variation in solvent height

XRD of films synthesised using lead DETC at varying solvent heights showed a decrease in particle size with increased solvent height, as well as a decrease in the variation in particle size calculated from different reflections, indicating a decrease in particle aspect ratio. Preferential orientation resulting in higher intensity (200) reflections than those observed in bulk PbS was observed in all samples. XPS of these samples after one week of exposure to air displayed an increase in the proportion of surface oxidised species in the samples synthesised using larger solvent heights. This is likely to be due to the smaller particle size, as estimated from the XRD, resulting in a greater rate of oxidation due to the increased surface-area to volume ratio. Oxidised species were primarily seen in the lead 4f peak, with little or no visible sulfite/sulfate. A moderate amount of neutral sulfur was observed in all samples, with the highest proportion of neutral sulfur also being observed in the sample synthesised using the largest solvent height. The formation of oxidised lead species, such as hydroxides and carbonates, prior to the formation of sulfoxy species has been reported previously[1]. The formation of neutral sulfur due to decomposition of the initial lead sulfide has been observed previously[1,2] however neutral sulfur is typically expected to be volatile and removed from the surface in vacuum at ambient temperatures[1]. As such, the neutral sulfur visible in XPS may be attributable to a lead-deficient sulfide formed on oxidation of lead[2].

XRD of films synthesised using purified lead dithiobiuret precursor at varying solvent heights exhibited the same decrease in particle aspect ratio with increasing solvent height as seen in those synthesised with lead DETC. The particle size itself however displayed no clear trend, with the broadest (111) and (220) reflections occurring in the sample synthesised with the lowest solvent height, while the broadest (200) reflection occurred in the sample synthesised with the highest solvent height. This indicates a more complex relationship between particle size and solvent height than a simple linear trend. As with the samples synthesised using lead DETC, there appeared to be strong preferential orientation of the particles resulting in an increased relative intensity of the (200) reflection. XPS of these sample exhibited a significantly larger proportion of oxidised species present in the sample synthesised at the lowest solvent height compared to that synthesised at the highest solvent height. Significant amounts of neutral sulfur were also observed in the sample synthesised at the lowest solvent height, with none visible at all in the sample synthesised at the largest solvent height.

9.2 Variation in precursor concentration

Samples were synthesised using 2:1, 1:1, and 1:2 ratios of lead DETC to sodium sulfide. XRD of these samples showed no clear trend in particle size with precursor concentration, however the lowest variation in particle size between different reflections was seen in the sample synthesised with a 1:1 precursor ratio. TEM of these samples showed string-like particles and agglomerates in the sample synthesised with a 2:1 ratio of precursors, angular, crystalline particles in the 1:1 sample, and more rounded particles across a broad size distribution in the 1:2 sample. This indicates that the morphology of the resultant particles is strongly affected by the concentrations of the precursors. XPS of these samples showed the highest level of both sulfur and lead oxidation in the sample synthesised with a 1:1 precursor ratio. All three samples exhibited at least a moderate amount of oxidised lead species, with relatively low amounts of sulfoxy species, further supporting the conclusion that oxidation proceeds via formation of oxidised lead species as the initial step[1].

9.3 Synthesis using longer-chain thiocarbamates

XRD of the films synthesised using lead DETC, DBTC and DPTC exhibited a slight increase in particle sizes with increasing length of the organic chain of the precursor, with lead DPTC samples exhibiting the largest average particle size estimates. This distinction is not especially clear, however, due to the broad range of calculated particle sizes from differing reflections. The greatest variation in particle size across the different reflections was also observed in lead DPTC, ranging from ~10 nm calculated from the (331) reflection, to ~40 nm calculated from the (200) reflection. The DPTC sample also exhibited the greatest degree of preferred orientation, with a much greater intensity of (200) and (400) reflections compared to other reflections than is seen in a typical lead sulfide powder diffractogram. SEM of samples synthesised using the lead DBTC precursor showed a variety of unusual morphologies, including thin, rod like structures, narrow cones, and several pyramid-like structures similar to that seen by D. Fan *et al.*[3], with small string or rod-like structures located at the tips. All of these structures appear to have grown from a similar small rod-like structure, which supports the observations made by D. Fan *et al.*. XPS of all these samples after ~3 weeks' exposure to air only exhibited oxidised lead species in the sample synthesised with lead DBTC (although this is potentially due to the breadth of peaks due to the lab-based x-ray source used making it difficult to resolve lead species at similar binding energies in the samples synthesised with lead DETC and lead DPTC). A moderate amount of neutral sulfur and a small proportion of sulfoxy species were seen in all three samples, similar to that observed previously in ~3 week aged samples. An increase in the width of the neutral sulfur doublet was seen with increasing precursor chain length, potentially indicating some interaction between the neutral sulfur and some remaining precursor deposited on the surface resulting in a decrease in conductivity, leading to charging-based peak broadening. Such an interaction could also explain how neutral sulfur is retained on the surface of the particles under exposure to vacuum, in contrast with what has been reported in the literature[1]. Absorption spectra of these samples exhibited a few small absorption features in both the samples synthesised using lead DETC and lead DBTC. The samples synthesised using lead DPTC however exhibited a broad, smooth rise in absorption with increasing photon energy, closer to that of bulk lead sulfide. All three samples exhibited a rise in absorption above approximately 0.5 eV, indicating that the predominant band gap is that of bulk lead sulfide.

9.4 Ageing of nanoparticle films

The aging of the films synthesised using varying precursor concentrations was also investigated. The original samples were examined using XPS after one week's exposure to air, as discussed previously, and after 9 months exposure to air. A set of samples synthesised under identical conditions were investigated after 3 weeks exposure to air. One of the most immediately apparent trends observed with increasing age is an increase in lead to sulfur ratio at greater sampling depths. This may the migration of sulfur from the core of the particle, and its loss at the surface. This can be explained by the presence of neutral sulfur as an apparent oxidation product, which is known from the literature to be volatile and easily removed in a vacuum[2,4] with the remaining neutral sulfur observed in the XPS being attributable to a lead-deficient sulfide[2]. While both neutral sulfur and oxidised lead species were seen in significant amounts after one week of exposure to air, sulfoxy species such as sulfite and sulfate were seen in significant amounts only after 3 weeks of exposure to air, and even after 9 months were not significantly increased. While all oxidised species of both lead and sulfur appeared in greater proportions at the surface of the particles, sulfate in particular was found to be extremely concentrated at the lower sampling depths. The oxidised sulfur thickness of the samples was calculated using the method given by Shard *et al.*[5] and was found to typically reach a maximum of around 1 nm, assuming a spherical particle of 10 nm diameter. The rate of increase of oxidised sulfur thickness was found to decelerate with time, following an approximately logarithmic relationship with time. It is likely that this is due to the passivation of the surface by the oxidation products themselves, as described in the literature previously[1]. A proposed oxidation mechanism involves the formation of lead hydroxide and hydrated oxide as the initial oxidation products, leaving neutral sulfur or sulfur in lead-deficient sulfide behind. This is followed by formation of lead sulfite and sulfate *via* sulfur dioxide as an intermediate reaction product. The proposed mechanism is detailed in equations 1-5

$$PbS + 2H_2O \Rightarrow Pb(OH)_2 + 2H + S \quad (1)$$

$$6Pb(OH)_2 + 2H_2O \Rightarrow Pb_6O_4(OH)_4 + 6H_2 \quad (2)$$

$$S + O_2 \Rightarrow SO_2 \quad (3)$$

$$Pb_6O_4(OH)_4 + 6SO_2 \Rightarrow 6PbSO_3 + 2H_2O \quad (4)$$

$$PbSO_3 + \frac{1}{2}O_2 \Rightarrow PbSO_4 \quad (5)$$

9.5 Overview

There is a strong indication from much of the XPS performed that the oxidation process occurring is incongruent, with initial oxidation forming oxidised lead species (probably hydroxides and hydrated oxides, as suggested in some of the literature[1]) and neutral sulfur, with sulfoxy species such as sulfites and sulfates forming later, sulfate being the final oxidation product. This is in agreement with some of the previous work done on lead sulfide oxidation[1,6,7]. The particle size appeared to decrease with increased solvent height for samples synthesised using lead DETC, however this dependence was not replicated in samples synthesised using lead dithiobiuret, indicating that a more complex relationship is likely present. The relative concentration of the lead and sulfur precursors appears to have a strong effect on particle morphology, but no strong effect on particle size was observed with the concentrations used. A increase in size of the organic portion of the lead precursor increased the size of the resultant particles on average, and a larger variation in estimated particle size across different diffraction peaks indicates a greater degree of preferential growth is also present with increased precursor ligand size. The smallest particles observed were on the order of 10 nm in diameter, and particles of this size were synthesised using both lead DETC precursor with the larger solvent heights, and at both low and high solvent heights with the lead dithiobiuret precursor.

9.6 Future work

While some of the smallest particles were synthesised using lead DETC, both lead DBTC and lead DPTC exhibited interesting results (unusual morphologies, and significant preferential growth, respectively) which are potentially worthy of further investigation. In particular, variation of solvent height of these precursors would also be useful in further investigating the precise relationship solvent height has to particle size, which is currently unclear due to the differing behaviours observed with lead DETC and lead dithiobiuret precursors. Variation of concentration for precursors other than the lead DETC may prove valuable in identifying whether the changes in morphology observed are dependent on precursor. Finally, construction of a research cell in order to determine potential efficiencies achievable with films of particles as have been synthesised thus far would be useful in investigating the practicality of further research into using this synthesis method for the aim of producing photovoltaic devices.

References

(1) Buckley, A. N.; Woods, R. *Applications of Surface Science* **1984**, *17*, 401-414.

(2) Hampton, M. A.; Plackowski, C.; Nguyen, A. V. *Langmuir : the ACS journal of surfaces and colloids* **2011**, *27*, 4190-201.

(3) Fan, D.; Thomas, P. J.; O'Brien, P. *Journal of the American Chemical Society* **2008**, *130*, 10892-4.

(4) Nowak, P.; Laajalehto, K. *Applied Surface Science* **2000**, *157*, 101-111.

(5) Shard, A. G. *The Journal of Physical Chemistry C* **2012**, *116*, 16806-16813.

(6) Nowak, P.; Laajalehto, K. *Fizykochemiczne Problemy Mineralurgii* **2007**, *Vol. 41*, 107-116.

(7) Yashina, L. V.; Zyubin, A. S.; Püttner, R.; Zyubina, T. S.; Neudachina, V. S.; Stojanov, P.; Riley, J.; Dedyulin, S. N.; Brzhezinskaya, M. M.; Shtanov, V. I. *Surface Science* **2011**, *605*, 473-482.